

Department of Precision and Microsystems Engineering

Estimation of the lateral force acting at the tire contact patch of a vehicle wheel using a hub bearing unit instrumented with strain gauges and Eddy-current sensors

J.A. den Engelse

Report no : AUT 2013.016
Coach : Dr. Ir. E.J.H. de Vries
Professor : Prof. Dr. Ir. E.G.M. Holweg
Specialisation : Automotive
Type of report : MSc thesis
Date : 5 June 2013

Estimation of the lateral force acting at the tire contact patch of a vehicle wheel using a hub bearing unit instrumented with strain gauges and Eddy-current sensors.

Master Thesis

J.A. den Engelse
Wb 1280384
PME-AUT

SKF

Engineering & Research Centre B.V.

Delft University of Technology

Faculty of Mechanical, Maritime and Materials Engineering

Department Precision and Microsystems Engineering

June 2013

Author:

John A. den Engelse

MSc student

Delft University of Technology

Faculty of Mechanical, Maritime and Materials Engineering (3mE)

Department Precision and Microsystems Engineering (PME)

Mekelweg 2

2628 CD Delft

The Netherlands

Phone: +031 (0)6 18817141

Email: johndenengele@gmail.com

Persons involved:

Daily supervisors

Dr. Ir. Edwin J.H. de Vries

Assistant professor vehicle dynamics

Delft University of Technology

Faculty of Mechanical, Maritime and Materials Engineering (3mE)

Department Precision and Microsystems Engineering (PME)

Mekelweg 2

2628 CD Delft

The Netherlands

Phone: +31 (0)15 27 86980

Email: E.J.H.deVries@tudelft.nl

Ir. Henk A. Mol

Scientist

SKF Engineering & Research Centre

Mechatronics

Kelvinbaan 16

3430 DT Nieuwegein

The Netherlands

Phone: +31 (0)30 6075684

Email: Henk.Mol@skf.com

Dr. Ir. Matthijs Langelaar

Assistant professor, structural optimization & computational mechanics group

Delft University of Technology

Faculty of Mechanical, Maritime and Materials Engineering (3mE)

Department Precision and Microsystems Engineering (PME)

Mekelweg 2

2628 CD Delft

The Netherlands

Phone: +31 (0)15 27 86506

Email: M.Langelaar@tudelft.nl

Ir. Simon.van.Ballegooij

SKF Engineering & Research Centre

Mechatronics

Kelvinbaan 16

3430 DT Nieuwegein

The Netherlands

Email: Simon.van.Ballegooij@skf.com

MSc thesis advisor:

Prof. Dr. Ir. Edward Holweg

Delft University of Technology

Faculty of Mechanical, Maritime and Materials Engineering (3mE)

Delft Centre for Systems and Control (DCSC)

Mekelweg 2

2628 CD Delft

The Netherlands

Phone: +31 (0)15 27 89007

Email: edward.holweg@skf.com

Abstract

Load Sensing Bearing (LSB) units are based on the measurement of the elastic deformation of the outer ring of the bearing unit usually using strain gauges which are placed along the circumference of the bearing.

The master thesis is aimed at estimating the lateral tire force of a vehicle wheel using the vehicle wheel bearing hub unit which is instrumented to become a LSB and is placed in a BMW E60 lab vehicle.

Calibration of the LSB is needed to obtain a strain-force model. In situ calibration is expensive, time consuming and not always possible. Therefore a calibration system, the Bearing Test System (BETSY) has been used. Sensor responses of the LSB are greatly influenced by differences in bearing housing compliance where on one hand the LSB is mounted on the machine and on the other hand in the vehicle. It will be shown how it is possible to use BETSY as calibration system when the LSB is mounted to machine via the actual knuckle and ball joints found in the vehicle.

Next, a Multivariate Linear Regression Analysis (MLRA) is used to obtain a strain-force model to estimate the lateral force. However, the strain gauges are subjected to thermal influences of a low frequent nature and can therefore only be used to estimate the 'high'-frequent lateral force. Besides that, it is not possible with the specific compact wheel hub unit of the BMW E60 lab vehicle to determine, with the strain gauges, whether the vehicle is turning left or right. To overcome these two issues, two Eddy-current sensors measuring the tilting movement of the ABS-ring, which is integrated in the seal of the bearing, are used to determine the direction and to estimate the low frequent content of the lateral force.

Calibration and validation experiments are performed to show the accuracy and precision of the lateral force estimation.

Acknowledgement

I would like to thank my daily supervisors Henk Mol and Edwin de Vries for all their assistance, help, advice, eye-openers and their precious time they gave me during my master thesis project. I would also like to thank Henk Mol for giving me the opportunity to work on my master thesis project within SKF. I had a great and interesting time and I gained a lot of experience and knowledge during my stay at SKF. Furthermore I would like to thank all other people working at the mechatronics and automotive departments at SKF with a special thanks to Simon van Ballegooij with whom I spent a lot of time in the Carlab while working on the installation of the LSB in the BMW. Also thanks to Gilbert Peters who helped me in the Carlab with the process of bleeding the brakes of the BMW after the replacement of the brake calipers and –discs.

I would also like to thank Matthijs Langelaar, Daniel Rixen, Poalo Tiso, Arend Schwab and all the students who attended the monthly student progress meetings for their useful discussions and feedback during these meetings.

Another thanks to Tjalling Veldhuizen, Peter van Amelsfoort, Henk Lupker and the rest of the people at Fontys for their time and interesting discussions.

I would also like to thank the staff and students of the PME department at the 3mE faculty of the TU Delft who advised and motivated me in any way possible.

Table of contents

Abstract	vii
Acknowledgement	ix
Table of contents	xi
List of figures	xv
List of tables	xviii
Acronyms	xix
1 Introduction	1
2 Calibration method	5
2.1 Introduction	5
2.2 Bearing calibration system: Bearing test system (BETSY)	6
2.3 Field measurements: Papenburg (Zaaijer, 2005)	9
2.4 Applied loads to the LSB mounted on BETSY	10
2.5 Sign convention	13
2.6 Signal conditioning	14
2.6.1 BETSY	14
2.6.2 Field measurements	16
2.6.3 Low- and high pass filtering	20
2.7 Analysis of the forces	21
2.7.1 Global behaviour	21
2.8 Analysis of the strains	22
2.8.1 Global behaviour	22
2.9 Relation between the lateral force F_y and strain ϵ	23
2.10 Conclusions	31
3 Lateral force estimation by the deformation of the bearing outer ring using a Multivariate Linear Regression Analysis	33
3.1 Multivariate Linear Regression Analysis	33
3.1.1 Result	37
3.2 Separate estimation for positive- and negative lateral force	39
3.2.1 Result: Left, right and total	40
3.3 Separation into two frequency bands	42
3.3.1 Theory MLRA	43
3.3.2 Result	45
3.4 Changing the order of the MLRA	46
3.5 Reduction of the used strain gauges. Removal of poorly correlated strain gauges	47

3.5.1	Result	47
3.6	Conclusion	47
4	Sensor fusion; addition of Eddy-current sensors	49
4.1	Eddy-current sensors	50
4.2	Eddy-current sensor conditioning	51
4.2.1	BETSY	51
4.3	Lateral force estimation using the Eddy-current sensors.	55
4.3.1	Influence of the lateral force on the tilt	55
4.3.2	Reproducibility	58
4.4	Force estimation using the Eddy-current sensor signals	59
4.4.1	Force estimation using the tilt	60
4.4.2	Lateral force estimation using the tilting movement of the ABS-ring and the deformation of the LSB outer ring	64
5	Field / validation measurements	67
5.1	Field measurements set-up	67
5.2	Strain measurements: BETSY	73
5.3	Strain measurements: Field	74
5.3.1	Correlation	76
5.4	Comparison strain measurements: BETSY and field	76
5.5	Eddy-current sensor measurements: BETSY	78
5.6	Eddy-current sensor measurements: Field	80
5.6.1	Eddy-current sensor signals	80
5.6.2	Sampling rate	82
5.6.3	F_y - tilt curves field SKF	83
5.7	Comparison Eddy-current sensor measurements: BETSY and field	84
5.8	Reproducibility	86
5.8.1	BETSY measurements: Strain	87
5.8.2	BETSY measurements: tilt	88
5.8.3	Field measurements: strain	89
5.9	Algorithm force estimation	91
5.9.1	In situ calibration	94
5.9.2	BETSY calibration	96
6	Conclusions	101
7	Recommendations	105
8	Appendices	107
8.1	Appendix A	107
8.1.1	Overview measured variables Papenburg	107
8.2	Appendix B	108
8.2.1	Papenburg vehicle specifications	108

8.3	Appendix C	109
8.3.1	Frequency analysis: Papenburg	109
8.3.2	Comparison	111
8.3.3	Frequency analysis BETSY	114
8.4	Appendix D	118
8.4.1	Overview of the performed field tests at SKF, Nieuwegein	118
8.5	Appendix E	119
8.5.1	F_y vs. bottom- and top deflection	119
8.6	Appendix F	122
8.6.1	F_y estimations using Eddy-current sensor	122
8.7	Appendix G	125
8.7.1	Cabling of the sensor signals	125
9	Bibliography	129

List of figures

Figure 1 A load sensing bearing	1
Figure 2 Bearing unit instrumented with six sensors	2
Figure 3 Performed experiments	3
Figure 4 Placement of the strain gauges along the circumference of the LSB placed in the left front wheel	5
Figure 5 The bearing test system	6
Figure 8 The load cycle consisting of 24 load steps with superimposed noise	7
Figure 6 BETSY load and moment convention	7
Figure 7 The load cycle consisting of 24 load steps without superimposed noise	7
Figure 9 LSB mounted on BETSY with a knuckle with ball joints	8
Figure 10 MTS wheel force transducer assembly (Swift version)	9
Figure 11 MTS wheel force transducer assembly (Swift version)	9
Figure 12 The lateral force F_y versus the vertical force F_z measured during all different tests performed in Papenburg	10
Figure 13 The lateral force F_y versus the vertical force F_z measured during a test run performed on BETSY.	12
Figure 14 The lateral force F_y versus the vertical force F_z measured during tests performed in Papenburg and a test run performed on BETSY	12
Figure 15 Coordinate systems. Left: Papenburg. Right: BETSY	13
Figure 16 Unconditioned strain signals for BETSY +0005	14
Figure 18 Conditioned strain signals for BETSY +0005	15
Figure 17 Conditioned strain signals for BETSY +0005	15
Figure 19 Unconditioned raw strain gauge signals. Field measurement: Papenburg - slalom008	16
Figure 20 Filtered strain gauge signals $\omega_c = 10$ Hz. Field measurement: Papenburg - slalom008	16
Figure 21 Conditioned strain gauge signals. Field measurement: Papenburg - slalom008	17
Figure 22 VELOS measuring wheel	17
Figure 23 Measured VELOS signals. Upper plot: The six signals from the six full Wheatstone bridges. Lower plot: The signals of the angle resolver	19
Figure 24 Processed VELOS signals. Forces and moments in the vehicle coordinate system.	19
Figure 25 Block diagram of the filter process	20
Figure 26 Bode diagram on a logarithmic scale of the two filters. Blue: Low pass filter. Green: Bandpass filter	20
Figure 27 Bode diagram on an absolute scale of the two filters. Blue: Low pass filter. Green: Bandpass filter	20
Figure 28 Block diagram of the improved separation process of the two frequency ranges	21
Figure 29 Bode diagram of the improved separation process of the two frequency ranges	21
Figure 30 Measured forces, moments and strains. Above: Papenburg 'slalom008', Below: Betsy 'BWM+0005'	22
Figure 31 Placement of the strain gauges along the circumference of the load sensing bearing	22
Figure 32 Load lines of the two ball rows	23
Figure 33 Lateral force vs. strain for tests performed at Papenburg	24
Figure 34 Lateral force vs. strain for tests performed at BETSY	25
Figure 35 Lateral force vs. strain for tests performed at BETSY and in Papenburg	26
Figure 36 Lateral force vs. strain for tests performed at BETSY including linear fit lines	28
Figure 37 Lateral force vs. strain for tests performed at Papenburg including linear fit lines	28
Figure 38 Left: LSB in vehicle. Right: LSB on BETSY	31
Figure 40 Applied force plotted versus the estimated force	38
Figure 41 Error distribution	38
Figure 39 Applied and estimated lateral force	38
Figure 42 F_y estimation where two calibration matrices are used. One for left- and one for right cornering data. Upper plot: . Middle plot: Estimation using calibration matrix calculated by right cornering data. Lower plot: Combined estimation	40
Figure 43 applied force versus the estimated force where a calibration is performed on left- and right cornering data separately	41

Figure 44 F_y estimation using a global and separate calibration matrices.	41
Figure 45 Lateral force vs strain with linear fit lines through the content per load step	42
Figure 46 Block diagram	45
Figure 47 Integrated steel ABS-disc in the rubber bearing sealing	49
Figure 49 Eddy-current sensor	50
Figure 48 Eddy-current sensors installed in the knuckle	50
Figure 50	51
Figure 51 Eddy-current signal conditioning electronics	51
Figure 52 Eddy-current sensor signals. Test BMW+0005.	52
Figure 53 Flow chart low of the value algorithm	53
Figure 54 Upper figures: The low values of Eddy-current sensor signal before the low pass filter. Lower figures: The low values of Eddy-current sensor signal after the low pass filter	54
Figure 55 Filtering of the wobble on BETSY	54
Figure 56 Lateral force versus the measured deflection. Left plot: top sensor. Right plot: bottom sensor	55
Figure 57 Tilt vs. the lateral force F_y	56
Figure 58 Tilt versus lateral force approximated by n-th order polynomials	57
Figure 59 Reproducibility of the tilt measurement	58
Figure 60 Frequency separation of the BETSY signals	59
Figure 61 Low frequent force estimation using the tilt	60
Figure 62 Low frequent force estimation using the top sensor	61
Figure 63 Low frequent force estimation using the bottom sensor	62
Figure 64 Block diagram of the full algorithm	64
Figure 65 Applied and estimated lateral force versus time	65
Figure 66 Applied force versus the estimated force	65
Figure 67 Error distribution	66
Figure 68 Load sensing bearing. Left: Single LSB. Right: Mounted in the vehicle.	67
Figure 69 Conditioner box of the strain gauges	68
Figure 70 Conditioner box of the strain gauges installed in the vehicle	68
Figure 71 Eddy-current sensors and knuckle	69
Figure 72 Conditioner box Eddy-current sensor	69
Figure 73 DC/DC-converter for the Eddy-current conditioner boxes	70
Figure 74 Left: VELOS wheel. Middle: Conditioning and power electronics. Right: VELOS mounted to the vehicle.	70
Figure 75 New brake disc and - calliper	71
Figure 76 Data acquisition system: dSpace Autobox	72
Figure 77 BETSY test run	73
Figure 78 Measured signals: left bearing/knuckle	75
Figure 79 VELOS measured forces and moments	75
Figure 80 Lateral force vs. strain for tests performed at BETSY and at SKF	77
Figure 81 BETSY measurements: lateral force versus the measured deflection. Left plot: top sensor. Right plot: bottom sensor	78
Figure 82 BETSY measurements: tilt vs. the lateral force F_y	79
Figure 83 BETSY measurements: tilt versus lateral force approximated by n-th order polynomials	79
Figure 84 Measured Eddy-current signals during the field measurements.	80
Figure 85 Eddy-current sensor signal measured during the field measurements at the SKF test-track including the moving average filtered signals	81
Figure 86 Lateral force versus the measured deflection. Left plot: top sensor. Right plot: bottom sensor	83
Figure 87 Field measurements: tilt vs. the lateral force F_y	83
Figure 88 Field measurements: tilt versus lateral force approximated by n-th order polynomials	84
Figure 89 Tilt vs F_y measured on BETSY and during the field measurements. Left: 2nd order. Right: 6th order	85
Figure 90 F_y - strain curves for three BETSY test runs	87
Figure 91 Second order polynomial relation of the lateral force vs the tilt for the old and new BETSY data	89

Figure 92 Sixth order polynomial relation of the lateral force vs. the tilt for the 2011 and 2012 BETSY data	89
Figure 93 Lateral force vs. strain for the field measurements performed in Papenburg and at SKF	90
Figure 94 Block diagram method 1	92
Figure 95 Block diagram method 2	93
Figure 96 Frequency separation. Upper plot: Total signal. Middle plot: Signal content in the range from 0 Hz to 1 Hz. Lower plot: Signal content in the range from 1 Hz to 10 Hz.	93
Figure 97 Measured and estimated lateral force	94
Figure 98 Measured force versus the estimated force	95
Figure 99 Probability density distribution of the estimation error. Left: estimation by 2 MLRAs and the tilt. Right: estimation by 4 MLRAs.	96
Figure 100 Transformation of the strain measured in the vehicle	97
Figure 101 Lateral force estimation using BETSY calibration	97
Figure 102 Measured force versus the estimated force	98
Figure 103 Probability density distribution of the estimation error. Left: estimation by 2 MLRAs and the tilt. Right: estimation by 4 MLRAs.	98
Figure 104 Frequency spectrum of the strain signals	109
Figure 105 Frequency spectrum of the output signals	110
Figure 106 Ball pass frequency as a function of the wheel speed / vehicle speed	113
Figure 107 Frequency spectra of the strain gauges	114
Figure 108 Frequency spectra of the applied loads	115
Figure 109 Frequency spectra of the Eddy-current sensors	115
Figure 110 Overview of the performed field tests at the test track of SKF Nieuwegein	118
Figure 111 Deflection bottom sensor versus lateral force F_y including polynomial fits for BETSY BMW+0005 – BMW+0008	119
Figure 112 Deflection top sensor versus lateral force F_y including polynomial fits for BETSY BMW+0005 – BMW+0008	119
Figure 113 BETSY measurements: deflection bottom sensor versus lateral force approximated by n-th order polynomials for the BETSY test performed on the bearing which is mounted in the BMW E60	120
Figure 114 BETSY measurements: deflection top sensor versus lateral force approximated by n-th order polynomials for the BETSY test performed on the bearing which is mounted in the BMW E60	120
Figure 115 Field measurements: deflection bottom sensor versus lateral force approximated by n-th order polynomials	121
Figure 116 Field measurements: deflection top sensor versus lateral force approximated by n-th order polynomials	121
Figure 117 High frequent force estimation using the tilt	122
Figure 118 Full frequency range force estimation using the tilt	122
Figure 119 High frequent force estimation using the top sensor	123
Figure 120 Full frequency range force estimation using the top sensor	123
Figure 121 High frequent force estimation using the bottom sensor	124
Figure 122 Full frequency range force estimation using the bottom sensor	124
Figure 123 25 D-Sub plug	125

List of tables

Table 1 Measured signals during the BETSY tests with the	7
Table 2 BETSY test procedure	8
Table 3 The 24 load cases on BETSY	11
Table 4 Measured signals by the VELOS measuring wheel	17
Table 5 Linear calibration factors	18
Table 6 F_y - strain linear fit coefficients	29
Table 7 Transformation coefficients	30
Table 8 Estimation error	38
Table 9 Correlation between force and strain	39
Table 10 Accuracy improvement of the left/right separation	41
Table 11 Error quantification using separate calibration matrices for positive and negative F_y	42
Table 12 Correlation coefficients between applied F_y and measured strain for positive lateral force	43
Table 13 Correlation coefficients between applied F_y and measured strain for negative lateral force	43
Table 14 Result lateral force estimation using four different section	46
Table 15 Correlation between F_y and strain/higher order of the strain	46
Table 16 Results of the lateral force estimation using first to fourth order estimations	46
Table 17 Polynomial fit errors	57
Table 18 Fit coefficients for the top- and bottom sensor and the tilt	58
Table 19 RMS, mean and variance of the estimation error using the tilt	61
Table 20 RMS, mean and variance of the estimation error using the top sensor	61
Table 21 RMS, mean and variance of the estimation error using the bottom sensor	62
Table 22 Low frequent estimation errors	62
Table 23 High frequent estimation errors	63
Table 24 Full frequency range estimation errors	63
Table 25 Correlation coefficients R_{xy} for the low frequent content	63
Table 26 Correlation coefficients R_{xy} for the high frequent content	63
Table 27 Correlation coefficients R_{xy} for the full frequency content	63
Table 28 Estimation errors	66
Table 29 Power supply cabling	71
Table 30 Correlation coefficients between F_y and strain for the field measurements	74
Table 31 Correlation coefficients between F_y and strain for the field measurements	76
Table 32 F_y - strain linear fit coefficients	77
Table 33 Transformation coefficients	78
Table 34 BETSY measurements polynomial fit errors	80
Table 35 BETSY measurements polynomial fit errors	84
Table 36 Slopes and offsets of the linear fits of the three BETSY test runs	88
Table 37 Reproducibility errors of the strain gauge response	88
Table 38 Numbering LSB	90
Table 39 Reproducibility errors of the strain gauge response	91
Table 40 RMS, mean and standard deviation of the estimation errors using an in-situ calibration	96
Table 41 RMS, mean and standard deviation of the estimation errors using a BETSY calibration	99
Table 42 Frequency content per load	110
Table 43 Frequency content of the strain and measuring wheel signals	111
Table 44 Frequency spectra overview	116
Table 45 Strain gauge conditioner box left- and right side	125
Table 46 25 D-Sub connector at the trunk side	125
Table 47 25 D-Sub connector VELOS	126
Table 48 D-Sub 50 connector at the data acquisition unit	127
Table 49 Measured signals during the field tests at the test track of SKF Nieuwegein	128

Acronyms

ABS	Anti-lock Braking System
BETSY	BEaring Test SYstem
DoF	Degree of Freedom
F_x	Longitudinal force
F_y	Lateral force
F_z	Vertical force
MLRA	Multivariate Linear Regression Analysis
LSB	Load Sensing Bearing
M_x	Moment around the x-axis
M_y	Moment around the y-axis
M_z	Moment around the z-axis

1 Introduction

Nowadays, vehicles are becoming a more and more mechatronic system with increasing safety demands. Several systems in the vehicle, like the Antilock Braking System (ABS) and the Electronic Stability Control (ESC), are using several sensors as input to the control system to determine if actions are required.

The ABS for example is controlled by measuring the deceleration of the individual wheels and it intervenes to optimize the braking force at the wheel/road interface when locking (large deceleration) of a wheel is detected.

The ESC monitors the steering wheel angle, lateral acceleration, yaw rate and individual wheel speeds. When a probable loss of steering control is detected, by comparing the intended and actual direction of the vehicle, the systems intervenes by applying the brakes at individual wheels to create a compensating torque to redirect the vehicle into its intended direction.

These systems optimize the forces at the individual wheels to change the dynamics. A possible way to improve the algorithms behind these systems is to directly use the forces acting on the individual wheels as the control input.

To measure the forces acting at a vehicle's wheel, a Load Sensing Bearing (LSB) is developed at SKF, see Figure 1.



Figure 1 A load sensing bearing

A hub bearing unit is instrumented with six strain gauges to measure the deformation of the unit at six places along the circumference of the bearing, see Figure 2. The deformation of a bearing unit provides knowledge of the loads which are acting on it.

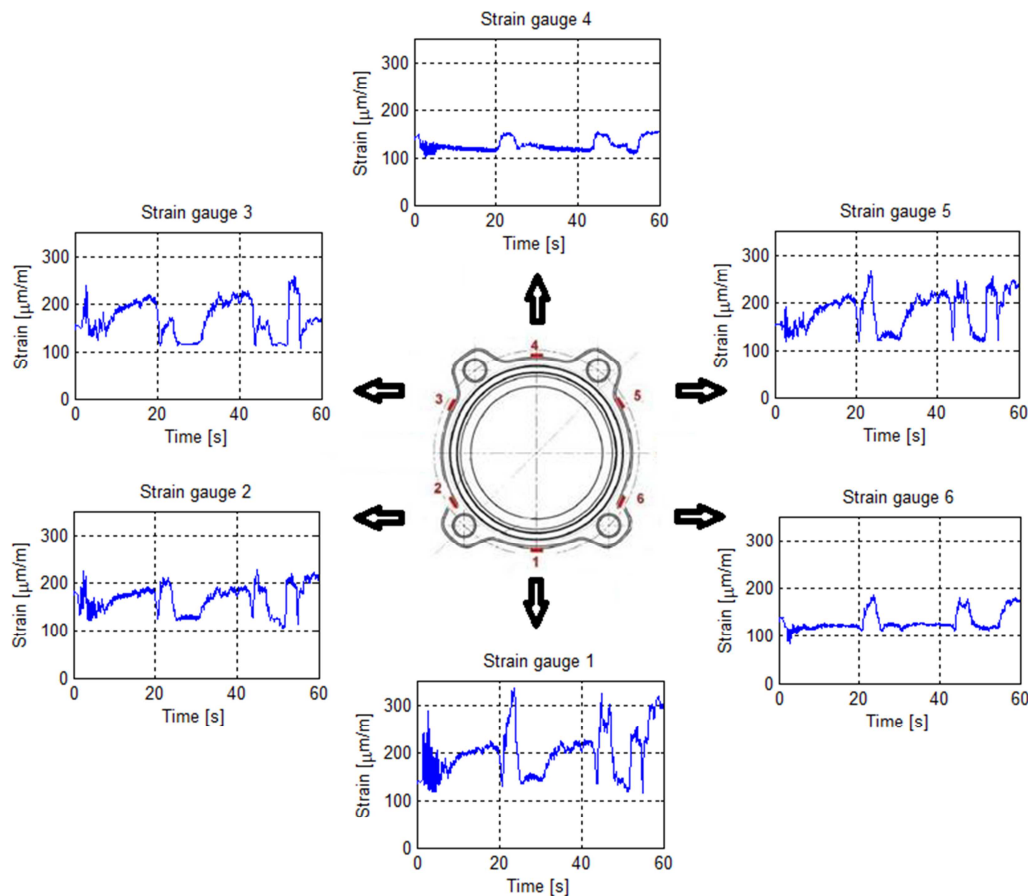


Figure 2 Bearing unit instrumented with six sensors

Whereas the longitudinal force is important for longitudinal dynamics which are controlled by the ABS, the lateral force is important, not unexpectedly, for the lateral dynamics which are controlled by the ESC. Vertical forces can play an important role to determine the loading of for example trucks.

This thesis aims to estimate the lateral force acting on the wheel of a vehicle. The lateral force is thus especially useful for the ESC which acts to improve the lateral stability of a vehicle.

The lateral force also plays an important role for the upcoming steer-by-wire systems. These systems replace the mechanical steering column by a system consisting of a sensor at the steering wheel to measure the intended steering maneuver and an electric motor/actuator at the wheel to realize a cornering maneuver. By removing the mechanical parts between the steering wheel and actual wheel touching the road the natural feeling of what is happening at the vehicle wheels is removed. By measuring the lateral force on the wheels a system can be implemented to give the driver haptic feedback on the steering wheel to restore the natural driving feeling to the driver.

Another motivation to measure forces, now from a bearing point of view, is that it creates the possibility to monitor the bearing during its lifetime. When it is known what forces have been acting/are acting on a bearing it can be predicted when and/or why a bearing will fail and when it's necessary to be replaced.

In this thesis the lateral force is first estimated using a Multivariate Linear Regression Analysis (MLRA) and six strain gauges which measure the deformation of the stationary outer ring of the bearing. Another sensor is introduced to compensate the shortcomings of the strain measurements. It measures the changed position and orientation of the inner ring with respect to the outer ring. This change in position and orientation is measured by two Eddy-current sensors using the ABS-ring which is mounted to the inner ring of the LSB. The signals from the strain gauges and Eddy-current sensors will be combined in order to improve the accuracy of the lateral force estimation.

The estimation of the lateral force will play the central role of the thesis. Besides the lateral force estimation the calibration of the LSB will also play an important role. For calibration, a test rig, the BEARING Test SYstem (BETSY), is used.

Four types of experiments are performed, see Figure 3. Two sets of BETSY experiments and two sets of field measurements. The field measurements in Papenburg have been performed in the year 2005 and contain only strain measurements. The BETSY measurements from 2011 and 2012 and the field measurements performed at the test track at SKF also include measurements with the Eddy-current sensors.

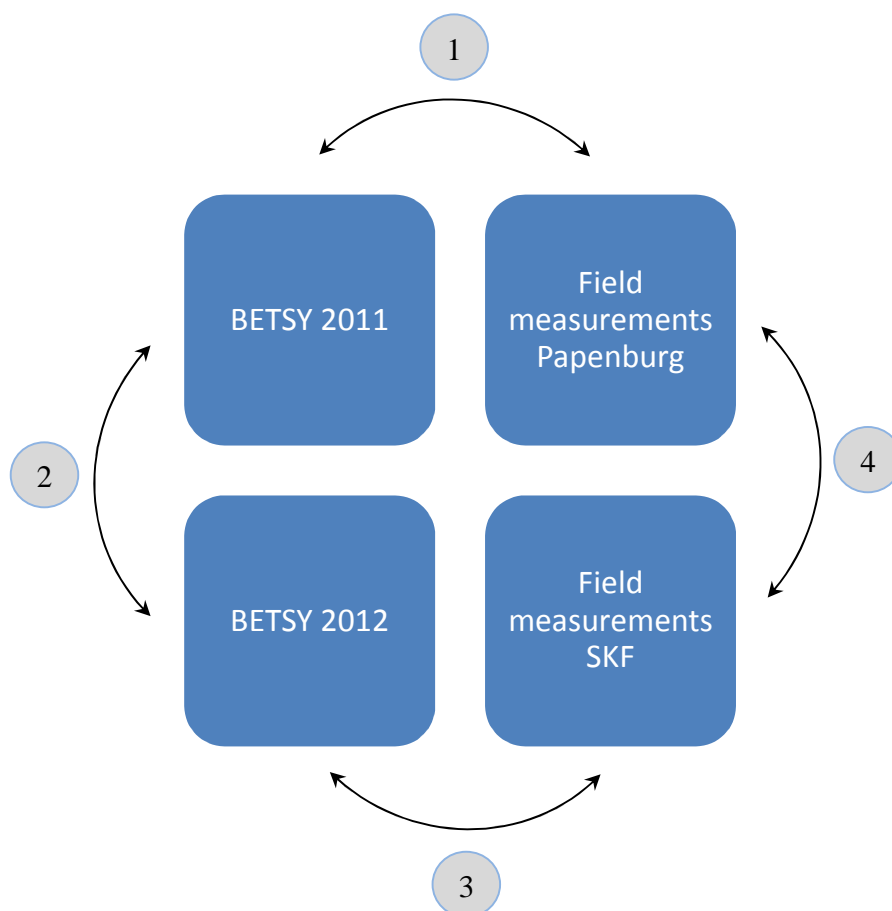


Figure 3 Performed experiments

Regarding the BETSY calibration process two aspects are of great importance.

The first is the compliance of the LSB environment. This environment plays an essential role in the sensor responses (Jayashankar, 2011), (Ballegooij, 2011). Because the environment on a test rig differs from that one found in the vehicle it is not obvious that it is possible that BETSY can be used for calibration.

The second is that the performed measurements are reproducible. As well as the measurements performed on BETSY as the measurements performed in the vehicle. Especially for the calibration of a whole production line of LSBs. If the measurements are fully reproducible, one single test on BETSY would be enough to calibrate the whole production line.

Figure 3 shows that comparisons will be made between the different types of experiments, as indicated by the numbers 1 to 4. Whether the sensor responses on BETSY are comparable with the sensor responses in the field is discussed in section 2.9 for the BETSY experiments from 2011 and the measurements in Papenburg, as indicated by the horizontal arrow 1 and in section 5.4 and section 5.7 for the BETSY experiments from 2012 at the field measurements at SKF, as indicated by arrow 3. Whether the BETSY- and the field experiments are reproducible is discussed in section 5.8 (indicated by the vertical arrows 2 and 4 respectively). The comparisons indicated by arrows 1 and 4 are only based on strain. The comparisons indicated by arrows 2 and 3 also include the Eddy-current sensor measurements.

Thesis outline

In Chapter 2 an introduction to the performed measurements at BETSY and in Papenburg will be given. First it is explained how BETSY will be used in the calibration process and what measurements are performed in the field. Based on what is measured in field it will be discussed what forces are applied to the LSB when mounted on BETSY. A sign convention will be established which is used throughout the whole thesis. Followed by the sign convention, an analysis of the measured strains and forces is given. At last a method will be derived in what way BETSY can be used as calibration system.

Chapter 3 will derive and validate the method for the lateral force estimation using a MLRA. Several improvements are dealt with and the results are shown.

In Chapter 4 the Eddy-current sensor is introduced and discussed. Force estimations are performed using the measured tilt. Chapter 3 and 4 are fully based on BETSY measurements performed in 2011.

To validate what is seen Chapter 3 and 4, LSBs are mounted into an actual vehicle and field measurements are performed. These measurements will be discussed in Chapter 5. The conclusions of the research will be given in Chapter 6, the recommendations in Chapter 7.

Chapter 8 will contain all the appendices. Finally, Chapter 9 shows the bibliography.

2 Calibration method

2.1 Introduction

The working principle of the LSB is based on measuring the deformation of the stationary outer ring of the bearing which is caused by forces acting on the bearing. These deformations are measured by six strain gauges which are placed along the circumference of the LSB, see Figure 2. By using a model that describes the relation between the deformation (strains) and forces, the forces can be estimated.

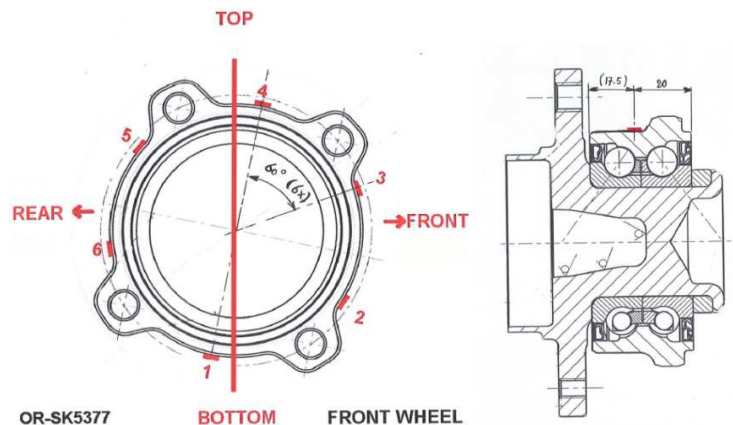


Figure 4 Placement of the strain gauges along the circumference of the LSB placed in the left front wheel

For calibration, a test rig, the BEARING Test SYstem (BETSY), is used. Calibration using a test rig is desirable, because it gives the opportunity to an in-house calibration of the LSB. The other option would be an in-situ calibration, which is time consuming and too expensive to repeat on every single vehicle when used in series production.

In a first calibration attempt the bearing was mounted onto the BETSY machine using a stiff mounting plate made of steel. Contrary, in the vehicle, the bearing is mounted in a compliant suspension consisting of the flexible knuckle/wheel carrier and control arms. Previous research (Jayashankar, 2011), (Ballegooij, 2011) has shown that the stiffness/compliance of the surrounding parts of the bearing greatly influence the response of the strain gauges. In that research the influence of the compliance of the surrounding parts of the LSB was investigated by mounting the LSB to the machine in four different set-ups where every set-up represented a different compliance.

First, as already mentioned, the LSB was mounted via a stiff disc and secondly a more flexible disc was used. Then, to obtain a more realistic behaviour, the actual knuckle was mounted on BETSY. First with rigid arms and finally with ball joints. It was shown that the sensor responses differed significantly per test case, depending on the mounting.

In this chapter the sensor responses from the case where the LSB is mounted to BETSY with the actual knuckle and ball joints, will be investigated. This is the mounting that resembles the mounting on the vehicle the most. The sensor responses will be compared with sensor responses found during field measurements in Papenburg, Germany.

In section 2.2 and 2.3 an introduction will be given to the BETSY machine and the field measurements performed in Papenburg, respectively. In section 2.4 the measured and

applied loads will be studied. In section 2.5 a sign convention is established to define the positive and negative directions of the loads acting on the bearing. Section 2.6 will guide the reader through the signal conditioning process of the BETSY and the field measurements followed in section 2.7 and section 2.8 by a global analysis of the measured forces and strains respectively. Finally this leads to strain force curves of the BETSY and the field measurements in section 2.9. Also explained in this section is how a transformation will be made from what is measured on BETSY to what is measured in the vehicle. So in what way BETSY can be used for calibration. The final conclusion to the question if BETSY can be used to calibrate the LSB has to wait until Chapter 5 where a new bearing of the same type is calibrated and tested and the reproducibility of the measurements is analyzed.

2.2 Bearing calibration system: Bearing test system (BETSY)

The Bearing Test System is a 5 Degree of Freedom (DoF) system, where forces and moments are applied in 5 DoF by hydraulic actuators in the range up to 15kN for forces and 2.5 kNm for moments, see Figure 5.

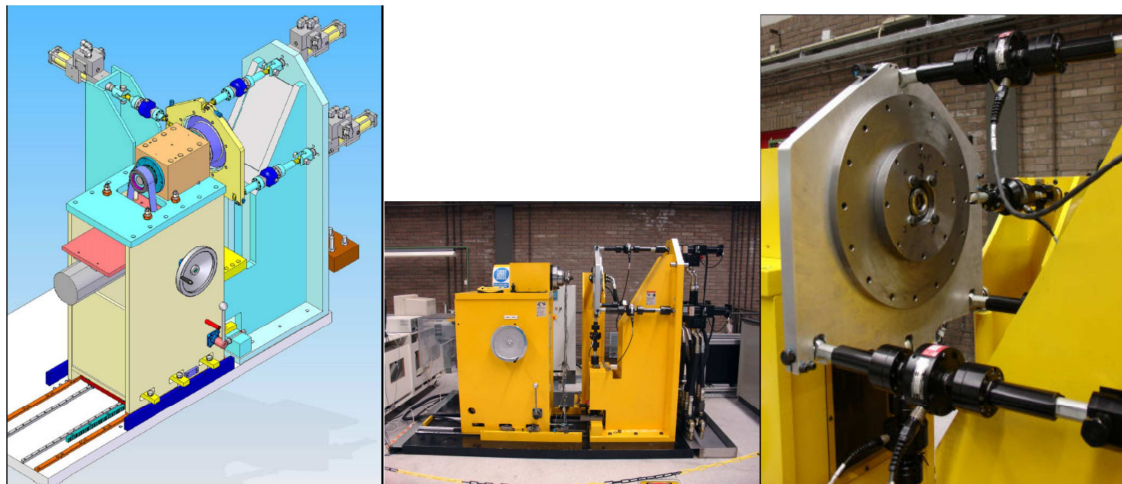


Figure 5 The bearing test system

The system consists of a mechanical structure, hydraulic actuators, a pump and a control PC. This system is used to apply forces to the knuckle/bearing arrangement. The coordinate system used for BETSY is shown in Figure 6.

BETSY can be used to calibrate the Load Sensing Bearing (LSB) by applying predefined loads to a LSB mounted on the machine. When measuring the signals from the strain gauges simultaneously with the applied forces, the applied forces can be considered as inputs and the strains as outputs to determine the input-output relation.

Table 1 shows an overview of the measured signals during the BETSY measurements. It shows that the speed, the lateral force F_y , the vertical force F_z , the moment around the x-axis M_x and the strain gauges signals are measured. Another four variables are measured which give information about the deformation of the knuckle and the tilt of the bearing during the tests.

Table 1 Measured signals during the BETSY tests with the appropriate scaling factors

Channel	Parameter	Scaling
1	Speed	300 [rpm/V]
2	F_x	1.5 [kN/V]
3	F_y	-1.5 [kN/V]
4	F_z	-1.5 [kN/V]
5	M_x	0.265 [kNm/V]
6	Strain A4	200 [$\mu\text{m}/\text{m}/\text{V}$]
7	Strain A5	200 [$\mu\text{m}/\text{m}/\text{V}$]
8	Strain B2	200 [$\mu\text{m}/\text{m}/\text{V}$]
9	Strain B3	200 [$\mu\text{m}/\text{m}/\text{V}$]
10	Strain C1	200 [$\mu\text{m}/\text{m}/\text{V}$]
11	Strain C6	200 [$\mu\text{m}/\text{m}/\text{V}$]
12	Strain A, knuckle	200 [$\mu\text{m}/\text{m}/\text{V}$]
13	Strain B, knuckle	200 [$\mu\text{m}/\text{m}/\text{V}$]
14	ABS-ring, top displacement	1 [$\mu\text{m}/\text{m}/\text{V}$]
15	ABS-ring, bottom displacement	1 [$\mu\text{m}/\text{m}/\text{V}$]

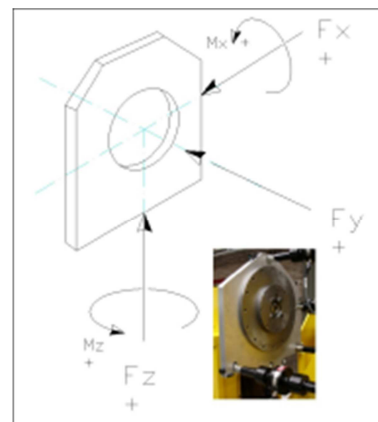


Figure 6 BETSY load and moment convention

A cycle consisting of 24 load steps is taken as a reference, see Figure 7. In this load-cycle combinations of the vertical force F_z and the lateral force $F_y + M_x$ are applied with 10 seconds of duration, with a ramp up/down time of 1 second. Between each load step a 10 seconds interval of running without load is inserted. On the load values a random noise signal with frequencies between 1 Hz and 9 Hz is superimposed on either the vertical load, the lateral load or for both to retain information about the dynamic response of the strain gauges to an applied load. Figure 7 and Figure 8 show the cycles without and with superimposed noise on both F_y and F_z , respectively. Due to an inclination misalignment of the LSB on BETSY, a wobble, with a frequency equal to the frequency of rotation (500 rpm = 8.33 Hz), is also superimposed to the static load.

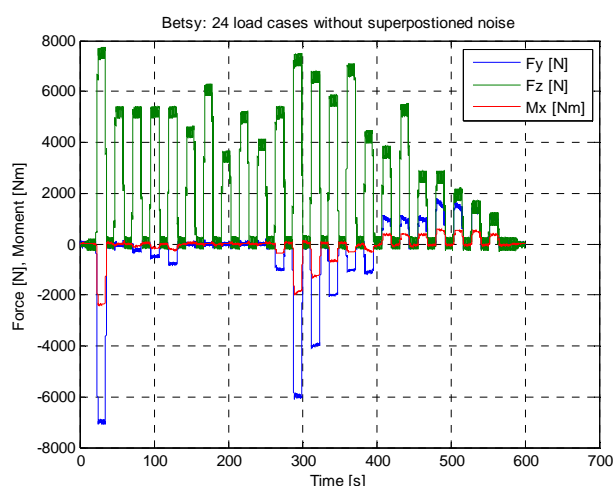


Figure 7 The load cycle consisting of 24 load steps without superimposed noise

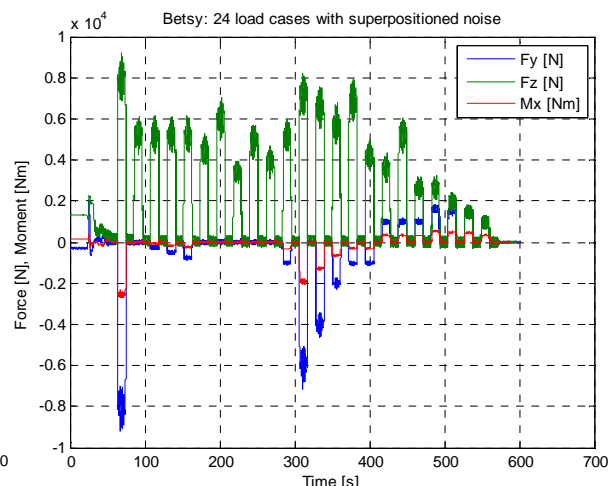


Figure 8 The load cycle consisting of 24 load steps with superimposed noise

In Table 2 the test procedure is shown. The total test procedure consists of four sessions. Every session consists of two runs. The first runs consist of a load cycle of three load

steps to check if everything is working correctly. Every second run is basically the same experiment and consists of the following four load cycles of 24 load steps:

- 1) Static lateral force F_y , static vertical force F_z , see Figure 7.
- 2) Static lateral force F_y + superimposed dynamic lateral force F_y , static vertical force F_z + superimposed dynamic vertical force F_z , see Figure 8.
- 3) Static lateral force F_y + superimposed dynamic lateral force F_y , static vertical force F_z
- 4) Static lateral force F_y , static vertical force F_z + superimposed dynamic vertical force F_z

Between each session the bearing-knuckle assembly is dismantled and mounted again to study the reproducibility of the measurements under possible different mounting stresses.

Table 2 BETSY test procedure

Test procedure BETSY September 2011			
<div style="border: 1px solid black; padding: 5px; margin-bottom: 5px;">Session 1 Bearing left front 2</div> <div style="border: 1px solid black; padding: 5px; margin-bottom: 5px;">Run 1 Test</div> <div style="border: 1px solid black; padding: 5px;">Run 2 - Static F_y, static F_z - Noise F_y, static F_z - Static F_y, noise F_z - Noise F_y, noise F_z</div>	↓	Disassembly / Assembly	↓
<div style="border: 1px solid black; padding: 5px; margin-bottom: 5px;">Session 2 Bearing right front 1</div> <div style="border: 1px solid black; padding: 5px; margin-bottom: 5px;">Run 1 Test</div> <div style="border: 1px solid black; padding: 5px;">Run 2 - Static F_y, static F_z - Noise F_y, static F_z - Static F_y, noise F_z - Noise F_y, noise F_z</div>	↓	Disassembly / Assembly	↓
<div style="border: 1px solid black; padding: 5px; margin-bottom: 5px;">Session 3 Bearing left front 3</div> <div style="border: 1px solid black; padding: 5px; margin-bottom: 5px;">Run 1 Test</div> <div style="border: 1px solid black; padding: 5px;">Run 2 - Static F_y, static F_z - Noise F_y, static F_z - Static F_y, noise F_z - Noise F_y, noise F_z</div>	↓	Disassembly / Assembly	↓
<div style="border: 1px solid black; padding: 5px; margin-bottom: 5px;">Session 4 Bearing right front 4</div> <div style="border: 1px solid black; padding: 5px; margin-bottom: 5px;">Run 1 Test</div> <div style="border: 1px solid black; padding: 5px;">Run 2 - Static F_y, static F_z - Noise F_y, static F_z - Static F_y, noise F_z - Noise F_y, noise F_z</div>	↓	Disassembly / Assembly	↓

Figure 9 shows the LSB when installed on BETSY with knuckle with ball joints.

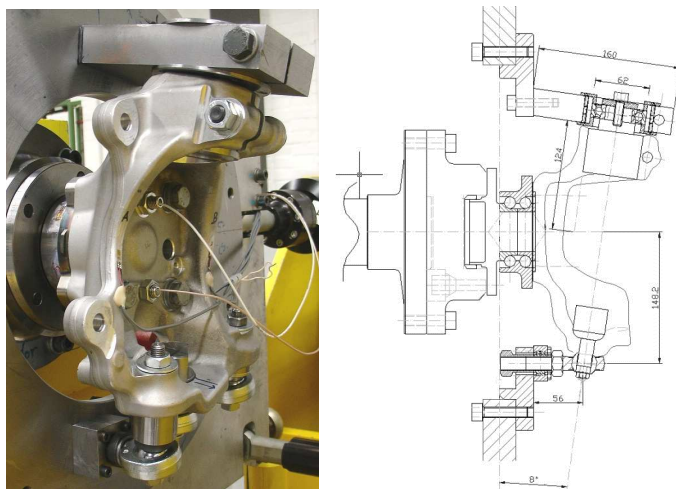


Figure 9 LSB mounted on BETSY with a knuckle with ball joints

2.3 Field measurements: Papenburg (Zaaijer, 2005)

In 2005 field measurements have been performed by SKF in Papenburg, Germany. A copy of the collected data was given to the TU Delft and Fontys. The objective was to drive a number of predefined maneuvers to collect load data over a large range of forces and moments from both the LSBs and the MTS wheel force transducers for post processing like calibration of the LSBs.

To measure the forces and moments in six degrees of freedom, four MTS force measurement wheels are used, see Figure 10.

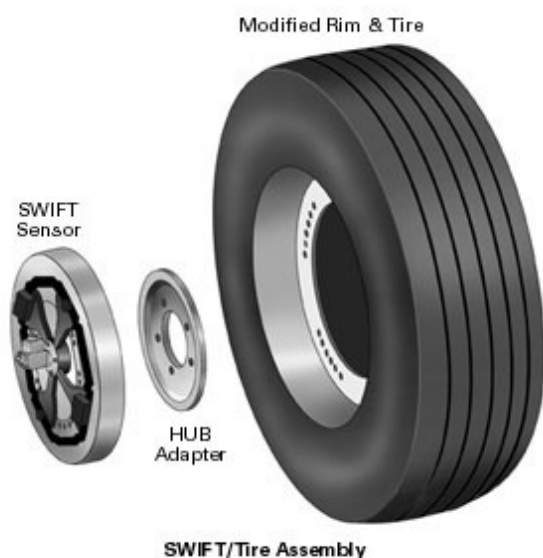


Figure 10 MTS wheel force transducer assembly (Swift version)

A total of 117 channels of data ranging from accelerometers to gear positions were recorded using a dSPACE Autobox System. Each LSB has six strain gauges and one temperature sensor. This required 28 channels only for the LSBs. Additionally 32 channels were required for the MTS wheels and all data was captured at 500 Hz. The list of all measured variables can be found in appendix A. A total of 480 maneuvers were driven during 4 days of testing. All maneuvers were performed twice (i.e. 240 individual maneuvers). The objective was to collect as much data as possible covering a wide range of loads and moments. Up front it was nearly impossible to predict what exact maneuvers would be required to cover the large range of forces and combination of forces, therefore a selection of predefined ISO standard maneuvers was made. Next, a description of the main maneuvers performed, together with the expected types of loads.

A wheel force transducer is a rotating load cell with strain gauges (or piezo electric sensors depending on the type) that is placed between the rim/tire and the hub unit. Forces acting on the tire are transferred to the hub through the wheel force transducer. This calibrated "sensor plate" then sends out the forces and moments applied on the wheel, together with its rotation angle using a resolver.

The BMW E60 545i is the car that is used for the measurements. Four LSBs were mounted on this vehicle, together with the four MTS wheels, Figure 10. Additionally, a number of accelerometers and two speed sensors were added. The measurements were performed at the ATP test track in Papenburg, Germany.



Figure 11 MTS wheel force transducer assembly (Swift version)

- Clockwise and counter-clockwise circular driving on fixed radii from zero speed to maximum (lateral and vertical load)
- J-turns at different steering angles (different lateral acceleration)
- Slalom at different speeds (lateral and vertical load)
- Braking in a straight line (braking loads including vertical loads)
- Braking in a turn (braking loads including lateral and vertical loads)
- Lane change (vertical and lateral loads)
- Vertical input (vertical loads)
- Wancken/Nicken. Wancken is the rotational motion around axis in driving direction due to a wavy road which is 180° out of phase between the left and right side of the vehicle. Nicken is the rotational motion along left/right axis due to a wavy road where the left and right side of the vehicle are in phase.
- Hill sections (traction, vertical and driving and braking loads)
- Banked roads (constant vertical/lateral loads)
- Durability track (large variations of different loads)

2.4 Applied loads to the LSB mounted on BETSY

To investigate whether the responses of the strain gauges on BETSY are equal to the response of the strain gauges measured during the field measurements, the LSB is mounted on BETSY and is loaded with lateral forces F_y and vertical forces F_z as explained in section 2.2.

During the field measurements in Papenburg it turned out that F_y and F_z are strongly correlated with each other. The relation between F_y and F_z is shown in Figure 12. In this figure the two forces are plotted versus each other for different kinds of tests performed in Papenburg. For all tests, except for the ‘wanken-nicken’ test, the forces lie on the same curve. These forces are measured, as explained in section 2.3, using the MTS force measuring wheels.

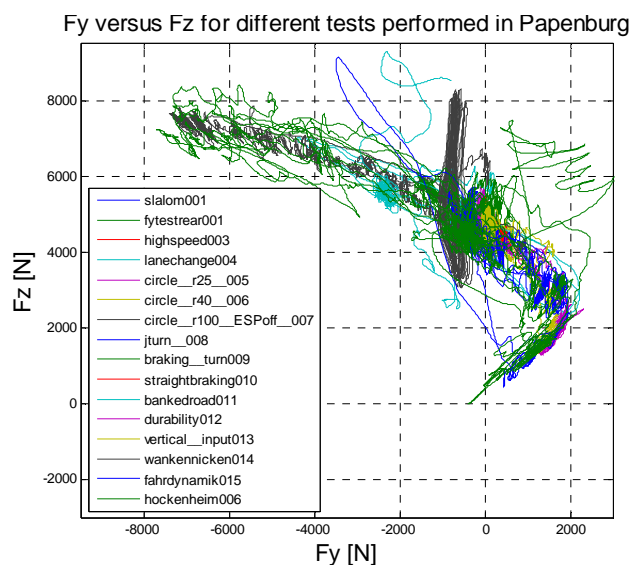


Figure 12 The lateral force F_y versus the vertical force F_z measured during all different tests performed in Papenburg

The load sensing bearing is loaded with forces which follow this measured curve. The load profile, the cycle of 24 load steps, is shown in Table 3. During load case 1 no load is applied to the bearing. Between each load case, load case 1 is executed, to be able to observe the temperature influence on the strain gauges. The actual load profile is thus: 1,2,1,3,1,4,1,5 .. and so on.

Table 3 The 24 load cases on BETSY

Load case	F_y [N]	F_z [N]	M_x [Nm]
1	0	0	0
2	-7260	7700	-2340,8
3	0	5300	0
4	-250	5300	-76
5	-500	5300	-152
6	-750	5300	-228
7	0	4500	0
8	0	6200	0
9	0	3500	0
10	0	5100	0
11	0	4000	0
12	-1000	5300	-304
13	-6000	7400	-1824
14	-4000	6700	-1216
15	-2000	5750	-608
16	-1000	7000	-304
17	-1000	4300	-304
18	1000	3700	304
19	1000	5400	304
20	1000	2700	304
21	1600	2700	486,4
22	1500	2000	456
23	1400	1500	425,6
24	1000	1000	-304

In Figure 13, the applied lateral force is plotted again versus the applied vertical force, but this time for the BETSY tests. The forces measured during the tests in Papenburg are following the same shaped curve as the forces applied on BETSY. As a matter of fact, it is a prerequisite that the loads are the same in both situations to be able to make a fair comparison. Unfortunately, due to a functional restriction of the BETSY machine, it was only possible to apply half of the intended loads to the bearing. Therefore the lateral-vertical force combinations applied on BETSY are not exactly occurring in the actual vehicle, but the ratio of the applied forces is equal to what is occurring in an actual vehicle. It will be shown in section 2.9 that the relation between force and strain is linear and therefore these tests can legitimately be used for analysis.

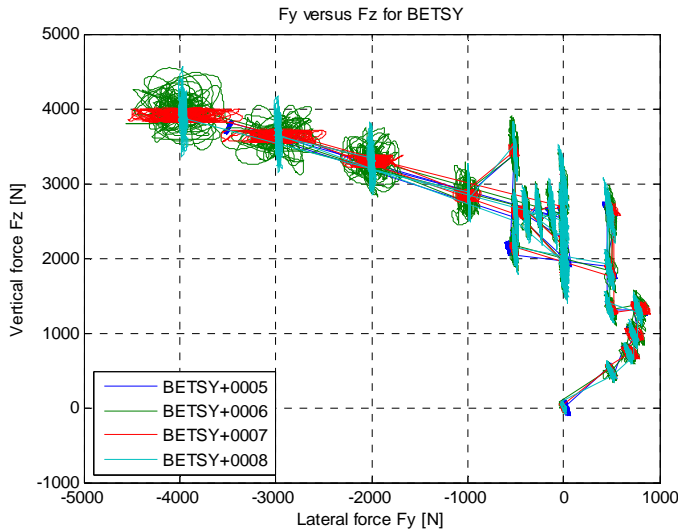


Figure 13 The lateral force F_y versus the vertical force F_z measured during a test run performed on BETSY.

In Figure 14, the measured and applied forces are plotted in the same figure. The Papenburg measurements are shown in blue and the BETSY measurements in green. In the left graph the original measured lateral and vertical forces are shown. On the right the BETSY forces are multiplied by two to show that the forces on BETSY are exactly one half of the forces measured during Papenburg and are thus applied in the same ratio on BETSY.

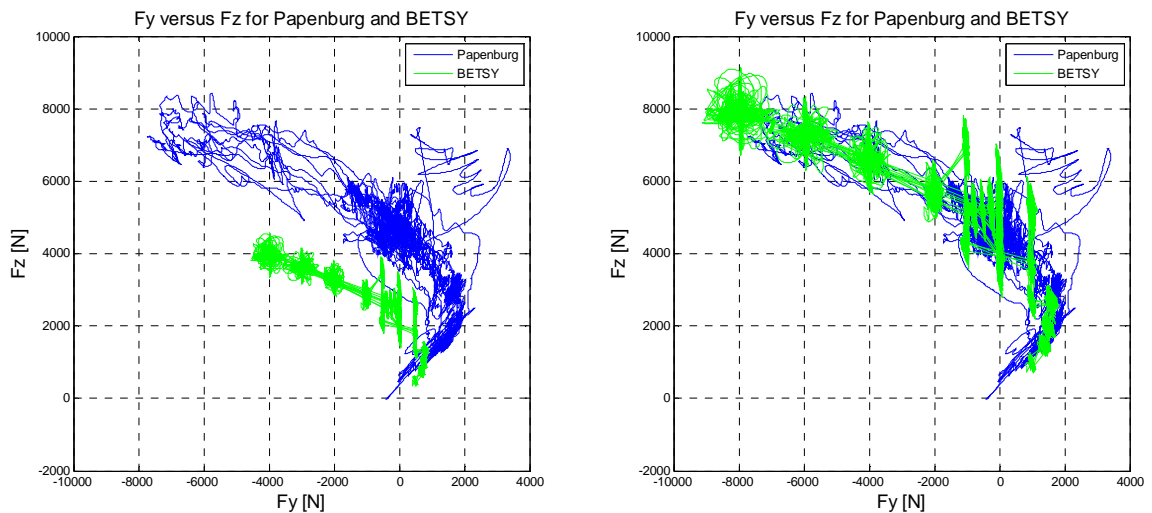


Figure 14 The lateral force F_y versus the vertical force F_z measured during tests performed in Papenburg and a test run performed on BETSY

2.5 Sign convention

The sign convention used during the measurements on BETSY differs from the sign convention used during the Papenburg measurements. To assimilate BETSY and Papenburg the following sign convention for the positive and negative forces and moments will be used. The stated sign convention is as seen from the driver's perspective.

- The longitudinal force F_x is positive when the vehicle is accelerating and it is negative during braking.
- The lateral force F_y is positive to the left and negative to the right.
- The vertical force F_z is positive downward and negative upward. This implies that the weight of the vehicle is positive.
- A positive lateral force F_y introduces a positive moment around the x-axis M_x , whereas a negative F_y introduces a negative moment around the x-axis M_x .
- A positive longitudinal force F_x introduces a positive moment around the x-axis M_y , whereas a negative F_x introduces a negative moment around the y-axis M_y .

All the available MTS wheel data is available subject to the sign convention stated above and as shown in the left figure of Figure 15.

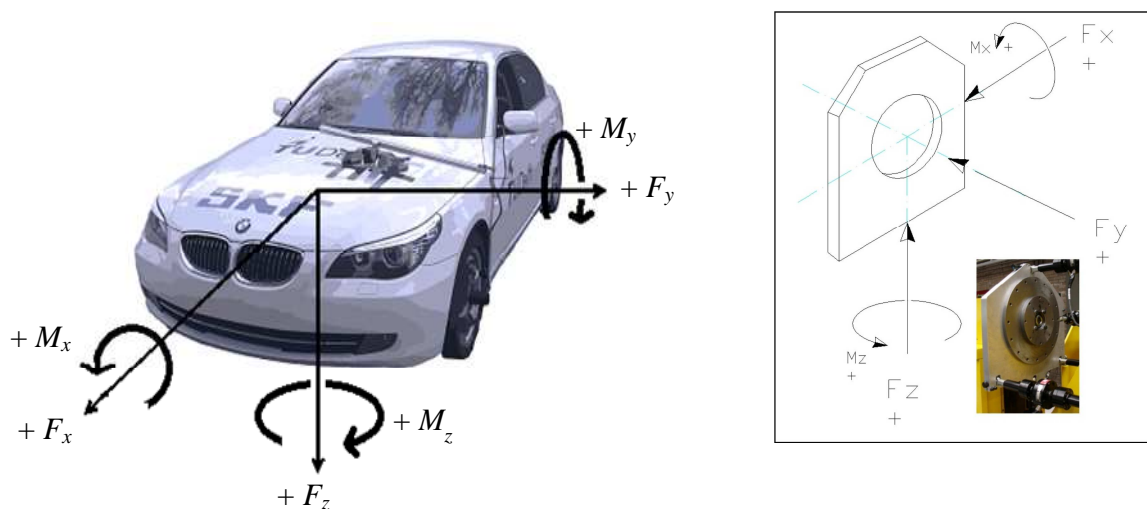


Figure 15 Coordinate systems. Left: Papenburg. Right: BETSY

In the right figure of Figure 15 the coordinate system used for BETSY is shown. The sign conventions for the lateral and vertical force used during the BETSY measurements are exactly the opposite of the preferred sign convention. All the forces at BETSY are changed to the sign convention used during the field measurements.

2.6 Signal conditioning

In this section the signal conditioning processes will be discussed. First for the data from the tests performed at BETSY and secondly for the tests performed in the field.

2.6.1 BETSY

2.6.1.1 Strain gauges and applied forces

In Figure 16 the unconditioned strain gauge signals are shown. Several unwanted measuring phenomena are observed. To be able to use the measured signals, the signals should be well conditioned. In this section it will be explained what steps are taken in the conditioning process of the BETSY signals.

The raw data is available in a compressed Labview format, an .FLD file. These files store the data as single precision 4 byte vectors. As a first step, the data vectors are splitted from the .FLD file, to be able to treat them separately.

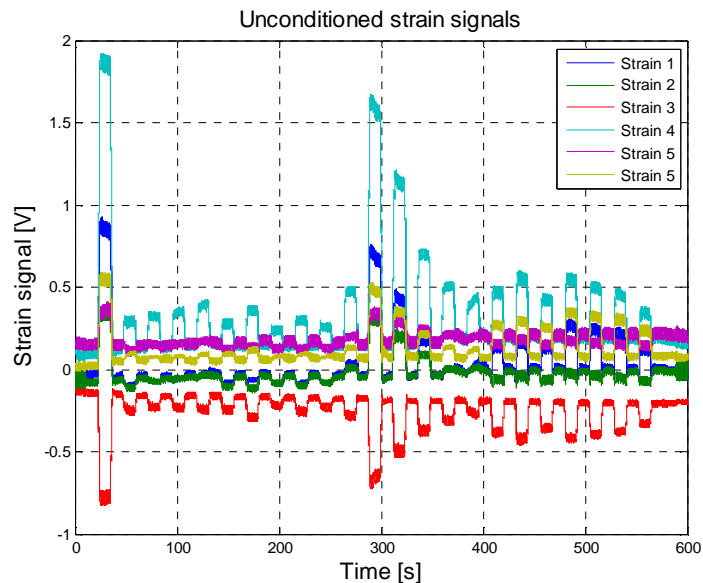


Figure 16 Unconditioned strain signals for BETSY +0005

The measurements are carried out with a sampling rate of 5000 Hz. Because the Papeburg data is available with a sampling rate of 500 Hz and to save computer memory, the BETSY signals are downsampled to a sampling rate of 500 Hz. A Labview program is available which can transform the BETSY data into a .csv format, which can be read by Matlab.

The steps taken in the conditioning process are listed as follows:

Filtering

The frequency content in the signals in the range up to 10 Hz is of interest. Therefore, the signals are filtered with a second or fourth order Butterworth low-pass filter with a cut off frequency of $\omega_c = 10$ Hz. The filtering process will be discussed in more detail in section 2.6.3

Static offset and drift

A DC-offset is observed in the first seconds although in these first seconds no load is applied.

Next to this static offset the sensors signals tend to drift during the measurements due to thermal gradient in the bearing outer ring (Bot, 2009). To compensate for these two unwanted effects, only the absolute in- or decrease in strain during the load intervals will be taken into account. This is accomplished by taking the signal during a load step and subtracting the average value of the no-load interval preceding the particular load step. See $\Delta\varepsilon$ in Figure 17.

Inverted signal strain gauge 3

The signal of strain gauge 3, behaves oppositely to the signals of the other strain gauges. This is not expected from the geometrical location so the plus- and minus terminal of the amplifier were connected oppositely. To compensate, the signal is therefore multiplied by a factor of -1 in the software.

No-load intervals

Next, the ‘no-load’ intervals are removed from the data. To be more specific, only the middle eight seconds of the ten second intervals are studied. See Δt in Figure 17.

Scaling

Then, to put the strain- and force signals into the physical dimensions, the signals are multiplied with a proper strain conversion factor as discussed in section 2.5. The conditioned signals are shown in Figure 18.

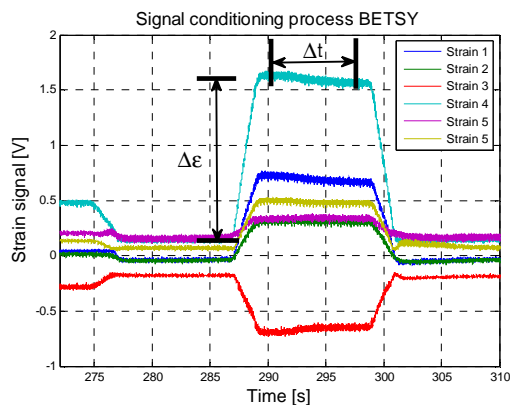


Figure 17 Conditioned strain signals for BETSY +0005

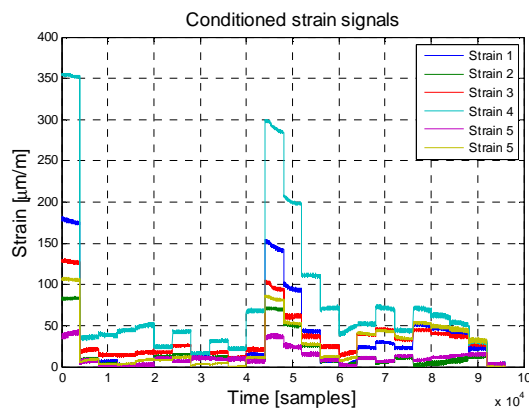


Figure 18 Conditioned strain signals for BETSY +0005

2.6.2 Field measurements

2.6.2.1 Strain gauges

The unconditioned strain gauge signals are shown in Figure 19. The measured forces and moment are not shown here but will undergo the same process. The signals undergo a process of three steps. First the signals are low pass filtered, secondly the offset is removed and finally the signals are converted to the physical dimensions.

Low pass filter

The frequency content in the signals range up to 10 Hz is of interest. Therefore, the signals are low pass filtered with a fourth order Butterworth low pass filter with a cutoff frequency of $\omega_c = 10$ Hz. This results in the signals in Figure 20. The filtering process will be discussed in more detail in section 2.6.3.

Offset

As for BETSY an offset is observed in the first seconds. This offset has several causes. First, the conditioning electronics can introduce an offset as a consequence of an unbalanced bridge of Wheatstone. Second, the mounting torque of the bolts which hold the bearing and knuckle/wheel carrier together has its influence. Also the difference in thermal expansion coefficient of the aluminum knuckle the and steel bearing and the thermal gradients in the bearing introduce offsets. At last an offset is introduced by the static vertical load resulting from the weight of the vehicle.

By removing this offset also the static vertical load information is removed. The focus lies on the relative changes in load and strain and mainly the lateral force will be of importance, so by keeping in mind that the information about the static vertical load is removed, it is allowed to perform this step.

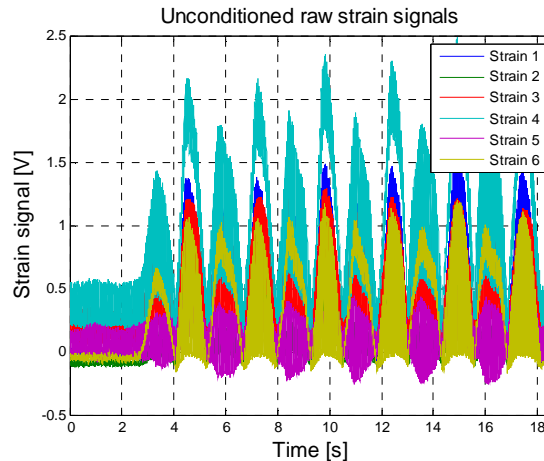


Figure 19 Unconditioned raw strain gauge signals. Field measurement: Papenburg - slalom008

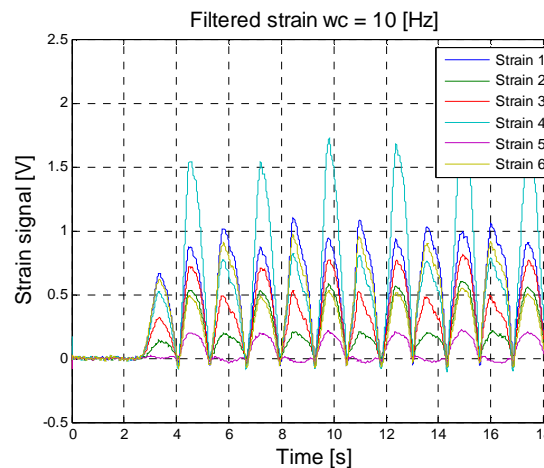


Figure 20 Filtered strain gauge signals $\omega_c = 10$ Hz. Field measurement: Papenburg - slalom008

Scaling

Thirdly, to put the signals into the physical dimensions, $\varepsilon = \mu\text{m}/\text{m}$, the signals are scaled with a proper scaling as discussed in section 2.5. The scaling factor for the strain gauges to convert the voltage to strain is $200 \mu\text{m}/\text{m}/\text{V}$.

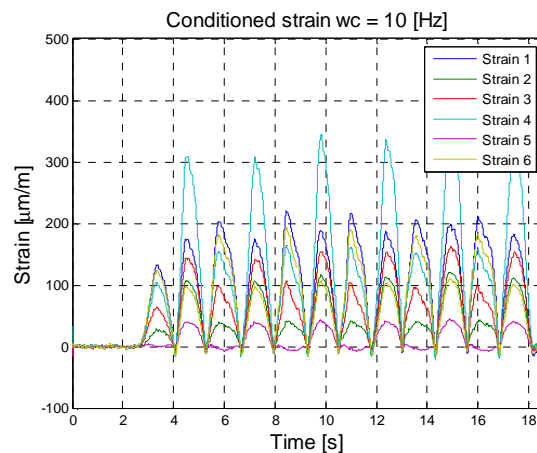


Figure 21 Conditioned strain gauge signals.
Field measurement: Papenburg - slalom008

2.6.2.2 Measurement wheel: Vehicle load sensor (VELOS)

With the multi-axial load sensor it is possible to determine the longitudinal, vertical and lateral forces as well as the respective moments introduced into the rolling wheel under operational conditions. These loads are measured to represent as close as possible the load at the point of load introduction, the tire contact patch.

Within the VELOS measuring wheel the forces and moments are measured in the rotating wheel frame by eight flexmembers wired up to 6 full Wheatstone bridges, one for each individual load component. The design leads to a complete decoupling of the individual forces and moments. The wheel rotation angle is measured by an angle resolver providing a sine- and cosine-signal. This angle resolver allows the transformation from the forces measured in the rotating frame to the stationary vehicle frame.

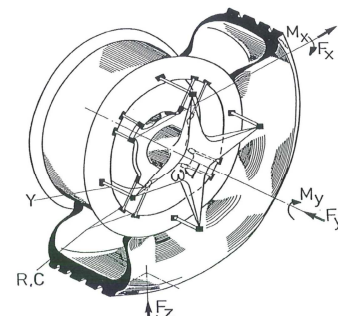


Figure 22 VELOS measuring wheel

The wheel rotation angle is measured by an angle resolver providing a sine- and cosine-signal. This angle resolver allows the transformation from the forces measured in the rotating frame to the stationary vehicle frame.

The measured signals in mV of one measuring wheel are stated in Table 4 and shown in Figure 23.

Table 4 Measured signals by the VELOS measuring wheel

Channel	Signal	Quantity	Signal offset [V]
1	MFY.DAT	For the lateral force	0,0906
2	MR13.DAT	For the radial force	-0,1379
3	MR24.DAT	For the radial force	0,5787
4	MMY.DAT	For the brake and acceleration moment	-0,6879
5	MM13.DAT	For the radial moment	-0,0334
6	MM24.DAT	For the radial moment	-0,0285
7	MSIN.DAT	Rotation angle sinus	-0,0289
8	MCOS.DAT	Rotation angle cosine	0,0012

For the conversion of these measured signals in [mV] to the physical units [N,Nm], the linear calibration factors are provided, see Table 5. (Kistler)

Table 5 Linear calibration factors

Calibration factor	Value	Unit
K(FY)	2.530	N/mV
K(R13)	3.476	N/mV
K(R24)	3.368	N/mV
K(MY)	0.580	Nm/mV
K(M13)	0.638	Nm/mV
K(M24)	0.638	Nm/mV
K(SIN)	0.222	1/4500 [1/mV]
K(COS)	0.222	1/4500 [1/mV]

These forces are de-rotated to the stationary coordinate system of the vehicle by the following formulas:

$$\begin{aligned}
 F_y &= K(F_y) \cdot MF_y \\
 M_y &= K(M_y) \cdot MM_y \\
 F_x &= MR_{13} \cdot K(R_{13}) \cdot MSin \cdot K(Sin) - MR_{24} \cdot K(R_{24}) \cdot MCos \cdot K(Cos) \\
 F_z &= -MR_{13} \cdot K(R_{13}) \cdot MCos \cdot K(Cos) - MR_{24} \cdot K(R_{24}) \cdot MSin \cdot K(Sin) \\
 M_x &= -MM_{13} \cdot K(M_{13}) \cdot MCos \cdot K(Cos) - MM_{24} \cdot K(M_{24}) \cdot MSin \cdot K(Sin) \\
 M_z &= -MM_{13} \cdot K(M_{13}) \cdot MSin \cdot K(Sin) + MM_{24} \cdot K(M_{24}) \cdot MCos \cdot K(Cos)
 \end{aligned} \tag{2.1}$$

During preparation of the system all the signals are adjusted to have zero mean. Small offsets within the signal introduce a considerable sinusoidal (with a frequency equal to the rotational frequency of the wheel) error superimposed on the expected signals. These small offsets can still be present in the signals after the every channel has been, as accurately as possible, zeroed. Therefore, before performing tests with the wheel, a first short time reference measurement is performed (Rolling straight on flat surface without braking or accelerating at a low speed of about 30 km/h) to determine inaccuracies and errors which may still be present.

Inaccuracies and errors during set-up may also lead to inaccurate definition of the wheel rotation angle with reference to the stationary wheel coordinate system. A correction can be made during post processing by the angle shift $\Delta\varphi$. Also the offsets can be compensated for during post processing.

The offsets and the angle shift $\Delta\varphi$ are determined using the short time reference measurement by

$$\Delta\varphi = \text{mean} \left\{ \arctan \frac{[MR_{24} - O(R_{24})]}{[MR_{13} - O(R_{13})]} - \arctan \frac{[MSin - O(Sin)]}{[MCos - O(Cos)]} \right\} \tag{2.2}$$

After calculation, by inserting the signals into (2.2), the angle shift turned out to be $\Delta\varphi = -0.1273 \text{ rad} = -7.3^\circ$.

The conversion to the stationary frame including the offsets and angle shift is performed as follows in (2.3):

$$F_y = K(F_y) \cdot [MF_y - O(F_y)]$$

$$M_y = K(M_y) \cdot [MM_y - O(M_y)]$$

$$F_x = [MR_{13} - O(R_{13})] \cdot K(R_{13}) \cdot \{[MSin - O(Sin)] \cdot K(Sin) \cdot \cos(\Delta\varphi) + [MCos - O(Cos)] \cdot K(Cos) \cdot \sin(\Delta\varphi)\} - [MR_{24} - O(R_{24})] \cdot K(R_{24}) \cdot \{[MCos - O(Cos)] \cdot K(Cos) \cdot \cos(\Delta\varphi) - [MSin - O(Sin)] \cdot K(Sin) \cdot \sin(\Delta\varphi)\}$$

$$F_z = -[MR_{13} - O(R_{13})] \cdot K(R_{13}) \cdot \{-[MSin - O(Sin)] \cdot K(Sin) \cdot \sin(\Delta\varphi) + [MCos - O(Cos)] \cdot K(Cos) \cdot \cos(\Delta\varphi)\} - [MR_{24} - O(R_{24})] \cdot K(R_{24}) \cdot \{[MCos - O(Cos)] \cdot K(Cos) \cdot \sin(\Delta\varphi) + [MSin - O(Sin)] \cdot K(Sin) \cdot \cos(\Delta\varphi)\} \quad (2.3)$$

$$M_x = -[MM_{13} - O(M_{13})] \cdot K(M_{13}) \cdot \{-[MSin - O(Sin)] \cdot K(Sin) \cdot \sin(\Delta\varphi) + [MCos - O(Cos)] \cdot K(Cos) \cdot \cos(\Delta\varphi)\} - [MM_{24} - O(M_{24})] \cdot K(M_{24}) \cdot \{[MCos - O(Cos)] \cdot K(Cos) \cdot \sin(\Delta\varphi) + [MSin - O(Sin)] \cdot K(Sin) \cdot \cos(\Delta\varphi)\}$$

$$M_z = -[MM_{13} - O(M_{13})] \cdot K(M_{13}) \cdot \{[MSin - O(Sin)] \cdot K(Sin) \cdot \cos(\Delta\varphi) + [MCos - O(Cos)] \cdot K(Cos) \cdot \sin(\Delta\varphi)\} - [MM_{24} - O(M_{24})] \cdot K(M_{24}) \cdot \{[MCos - O(Cos)] \cdot K(Cos) \cdot \cos(\Delta\varphi) - [MSin - O(Sin)] \cdot K(Sin) \cdot \sin(\Delta\varphi)\}$$

Where the offsets of the signal are given by $O(\Omega)$, $\Omega \in \{F_y, M_y, R_{13}, R_{24}, M_{13}, M_{24}\}$. With R_{dyn} the dynamic roll radius, the wheel speed v of the measuring wheel can be calculated by using the sin- and cos-signal of the angle resolver by:

$$v = \left\{ \frac{d(MSin)}{dt} \cdot [MCos - O(Cos)] - \frac{d(MCos)}{dt} \cdot [MSin - O(Sin)] \right\} \cdot R_{dyn} \cdot K(Sin)^2 \cdot 3.6 \quad (2.4)$$

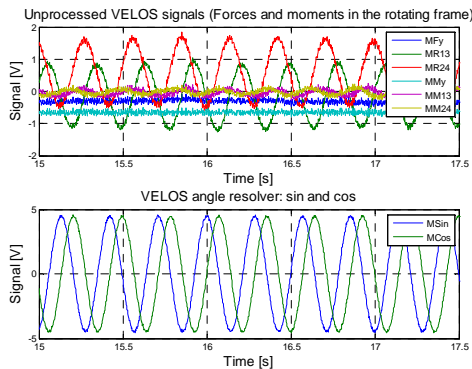


Figure 23 Measured VELOS signals.
Upper plot: The six signals from the six full Wheatstone bridges. Lower plot: The signals of the angle resolver

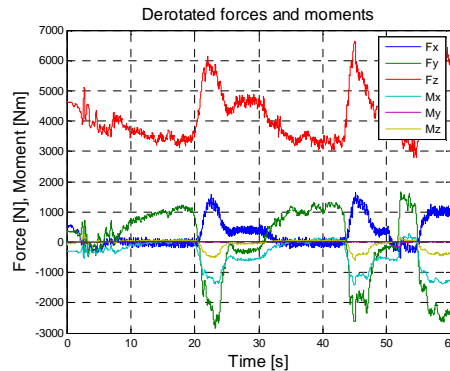


Figure 24 Processed VELOS signals. Forces and moments in the vehicle coordinate system.

After the calculation has been done the signals are low pass filter with a cutoff frequency of $\omega_c = 10$ Hz.

2.6.3 Low- and high pass filtering

Both the signals from the strain gauges and the measuring wheel are divided in two frequency bandwidths. The low frequent, quasi-static part will be represented by the frequency content from 0 Hz up to 1 Hz. The high frequent, dynamic part contains the frequencies from 1 Hz up to 10 Hz.

In Figure 25 the block diagram of the first attempt to separate the semi-static content from the dynamic content is shown. The separation is performed by two filters. A low pass filter with $\omega_c = 1$ Hz and a bandpass filter $\omega_{c,low} = 1$ Hz and $\omega_{c,high} = 10$ Hz is used. Because of different characteristics in the lower and upper path of the separation, the sum of the two paths does not equal the original signal, see Figure 26 and Figure 27.

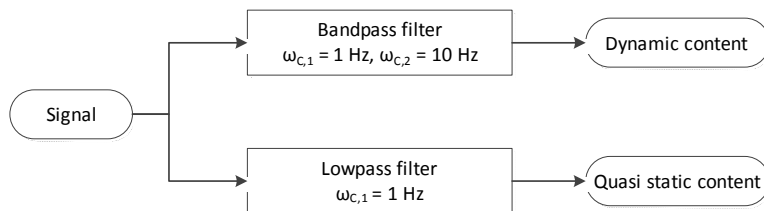


Figure 25 Block diagram of the filter process

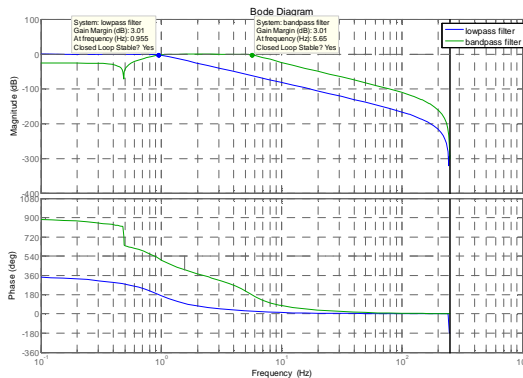


Figure 26 Bode diagram on a logarithmic scale of the two filters. Blue: Low pass filter. Green: Bandpass filter

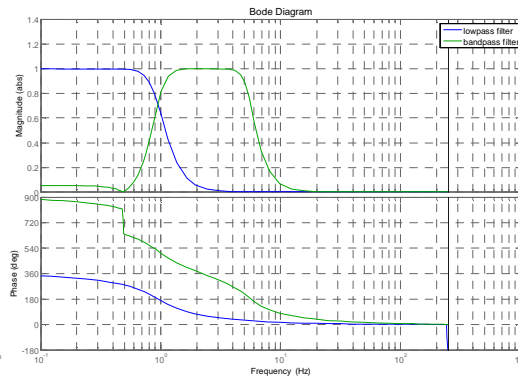


Figure 27 Bode diagram on an absolute scale of the two filters. Blue: Low pass filter. Green: Bandpass filter

Therefore, the filter process is improved so that both parts are complementary and the sum of the two paths results in the original signal again. (Mol, 2010) Two fourth order Butterworth low pass filters with cutoff frequencies of $\omega_1 = 1$ Hz and $\omega_2 = 10$ Hz are used.

First the signals are low pass filtered to get the low frequent semi-static content from 0 Hz up to 1 Hz. For the high frequent, dynamic part, the low frequent part is subtracted from the original signal. This results in two complementary signals, which when added up, result in the original signal. The dynamic content is then filtered with a low pass filter with $\omega_2 = 10$ Hz. To limit its frequency range up to $\omega_2 = 10$ Hz. The block diagram is shown in Figure 28 and the Bode plots are shown in Figure 29. The signals are filtered during the post-processing using the Matlab function *filtfilt*. This function compensates the introduced time shifts, so no time delay difference is present between the static and dynamic parts.

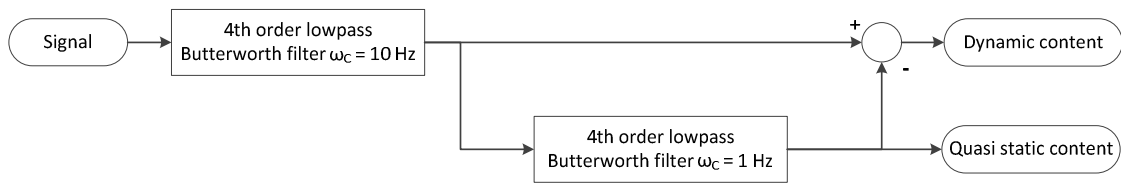


Figure 28 Block diagram of the improved separation process of the two frequency ranges

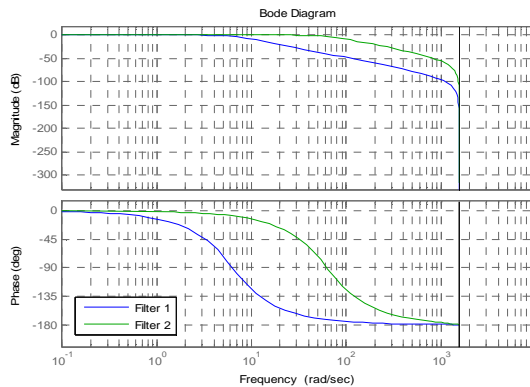


Figure 29 Bode diagram of the improved separation process of the two frequency ranges

2.7 Analysis of the forces

2.7.1 Global behaviour

Used tests:

Papenburg: [slalom008_FyFzMx_s1-s6.txt](#)

Betsy: [BMW0005_FyFzMx_s1-s6.txt](#)

See Figure 30. The two left graphs of this figure show the measured loads during the field measurements (upper left graph) and the applied loads on BETSY (lower left graph). The shown data is the data from the front left wheel. The vertical force measured during Papenburg shows a positive static force $F_{z,static} \approx 4900$ N during the first seconds (upper left graph). This is in agreement with the coordinate system for the car; a positive downward vertical gravitational force due to the weight of the vehicle is expected.

At approximately $t = 3$ s, a decrease in vertical force accompanied by an increase in lateral force is observed. Because the left wheel is analyzed this vertical unloading of the wheel indicates a clockwise roll angle which in turn indicates cornering to the left. The upper left graph indeed shows that the decrease in vertical force is accompanied by a positive lateral force. The moment around the x-axis, M_x , is proportional to the lateral force so $M_x = c \cdot F_y$.

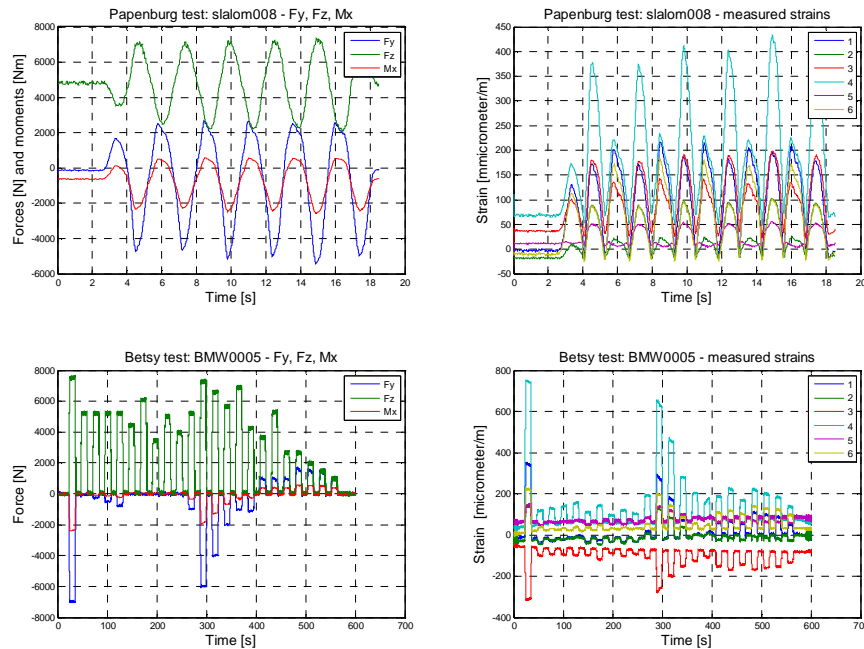


Figure 30 Measured forces, moments and strains. Above: Papenburg ‘slalom008’, Below: Betsy ‘BWM+0005’

The lower left figure shows the forces applied on Betsy. Again in agreement with the sign convention; a positive lateral force is accompanied by a decrease in vertical force and vice versa. The signals are transformed to the frequency domain by a Fourier transform and the frequency content is analyzed in Appendix C.

2.8 Analysis of the strains

2.8.1 Global behaviour

See Figure 30. The two right graphs of this figure show the measured strains during the field measurements (upper right graph) and the measured strains on BETSY (lower right graph). First of all, the ‘absolute value problem’ can be observed. Whenever a positive or negative lateral force is measured (in the field) or when applied (on BETSY), there will always be measured a positive strain. This is a great disadvantage because it excludes the possibility of recognizing left and right turns. In section 2.9.1.1 the absolute value problem is discussed in greater detail.

When observing the strains measured during a left corner during the field measurements of Papenburg, a strict pattern is observed in the sensitivity of the sensors.

From most sensitive to least sensitive the order of the strain gauges for a left cornering move is: 6, 1, 4, SKF

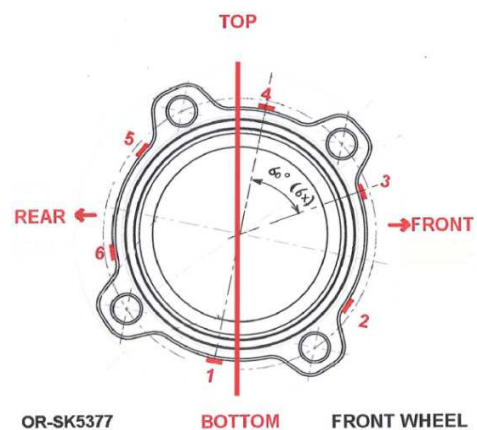


Figure 31 Placement of the strain gauges along the circumference of the load sensing bearing

3, 2, 5. When observing a right cornering move the order from most sensitive to least sensitive is: 4, 1, 3, 6, 2, 5. This time the signals of the sensors 6 and 2 are very close to each other.

When observing the load situations on Betsy for left turning the order of sensitivity of the strain gauges is: 4, 6, 3, 1, 5, 2. For right turning it is 4, 1, 3, 6, 2, 5. In section 2.9 the same order of sensitivity is seen by looking at the steepness of the lines in the force – strain graphs. As for the load signals, also the strain signals are transformed to the frequency domain by a Fourier transform and analyzed in Appendix C.

2.9 Relation between the lateral force F_y and strain ϵ

In this section the relation between the lateral force F_y and the strain gauges will be shown. First for the Papenburg test and secondly for the BETSY tests.

2.9.1.1 Papenburg $F_y - \epsilon$ graphs

In Figure 33, six graphs are shown. Every graph shows the relation between the lateral force and one particular strain gauge. For every graph six tests are used.

The first thing that can be observed is the V-shape. The response is piecewise linear with two linear segments, one for $F_y < 0$ and one for $F_y > 0$. Both left cornering maneuvers, $F_y > 0$ N, and right cornering maneuvers, $F_y < 0$ N, show a positive linear response in strain. This is called the ‘absolute value problem’. As a result of this absolute value problem left and right corners cannot be distinguished. An extra input/sensor is needed to make the distinction. As will be seen in Chapter 4, the addition of Eddy-current sensors, which do not show the ‘absolute value problem’, are able to detect whether the vehicle is making a turn to the left or a turn to the right.

The origin of the absolute value problem lies in the small separation distance between the two ball-rows of the bearing, see Figure 32. (Henk Mol, 2010). The load transfer takes place via the balls in the two ball rows. The two load lines of these two ball rows (shown in thick black) cross the strain gauge (shown in red), resulting positive strain for both left- and right cornering maneuvers.

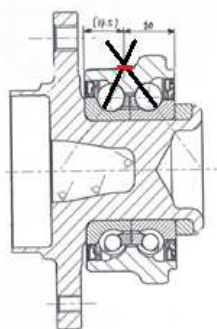


Figure 32 Load lines of the two ball rows

Papenburg: Lateral force F_y versus strain

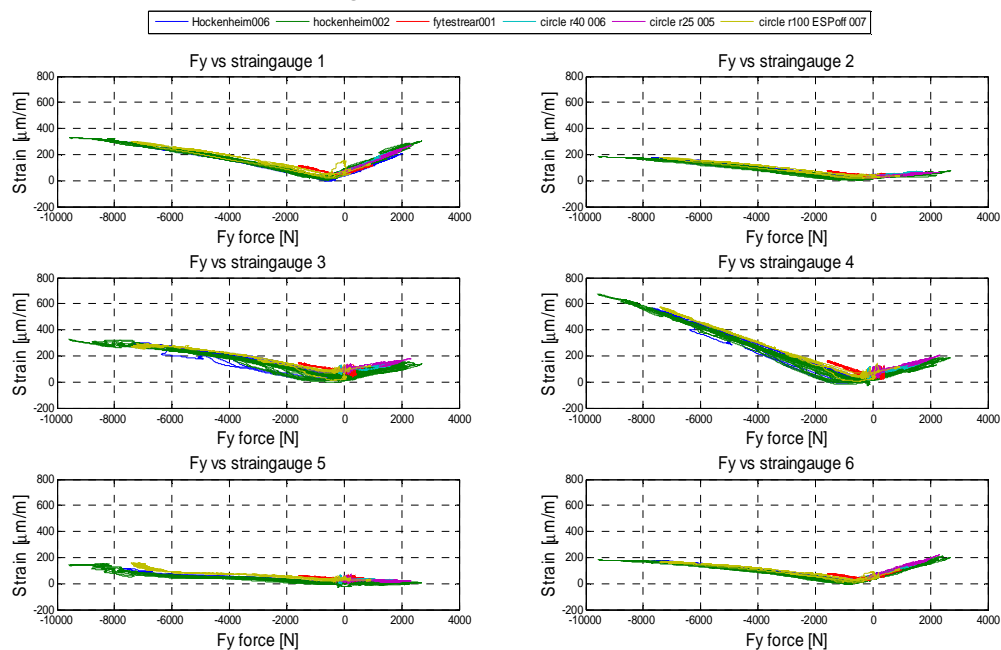


Figure 33 Lateral force vs. strain for tests performed at Papenburg

The second thing that can be observed is the difference in sensitivity of the strain gauges and the difference in sensitivity between left- and right turning. The steepness of both sides of the V-shape indicates the sensitivity and differs for both sides.

The order of strain gauge sensitivity from most sensitive (high steepness) to least sensitive (low steepness) can be determined in a blink of an eye; 4,1,3,6,2,5 for both left- and right turning. Interesting to note is that strain gauge 2 and 5 show hardly any response for left turning maneuvers, but do show response for right turning maneuvers. This can be explained by the change in the loaded zones of the LSB. The forces at the tire contact patch are transmitted from the inner bearing ring via the bearing balls to the outer ring. By turning the wheel and thereby changing the loads acting at the tire contact patch, in this case positive or negative lateral force, different sections of the ball rows will transmit the force and thereby changing the response of the strain gauges.

As told in the introduction the compliance/stiffness of the bearing support greatly influences the response of the strain gauges. In earlier research several attempts have been done to calibrate the LSB on BETSY. During these earlier tests the LSB was mounted on BETSY via a rigid disc, a flexible disc and a knuckle which was rigidly fixed. All these attempts resulted in strain which was not comparable to the strain measured during the field measurements as shown in Figure 33.

One of the questions which will be answered in this thesis is whether it is possible to use BETSY to calibrate the LSBs where the LSB is mounted on BETSY with a knuckle fixed with ball joints. The beginning of answering this question will be made in this section by graphically observing the relations of both the field measurements performed at Papenburg and the BETSY measurements.

In section 2.9.1.4, the V-shapes of all the strain gauges will be described by two linear relations. One for the left side and one for the right side; $\epsilon_{left} = c_{1,left} \cdot F_{y,left} + c_{2,left}$ and $\epsilon_{right} = c_{1,right} \cdot F_{y,right} + c_{2,right}$. Possibly, differences in sensitivity (steepness $c_{1,left}$ and $c_{1,right}$) or differences in offset ($c_{2,left}$ and $c_{2,right}$) can be observed. By describing the relations like this with two coefficients, transformation coefficients can be established to transform the relations measured during the tests performed at BETSY to the relations measured during the field measurements and vice versa.

When using BETSY for calibration of a complete production line of LSBs, an important requirement to use a set of transformation coefficients to transform between the BETSY and the vehicle response is that the measurements are reproducible. Only then the obtained coefficients will be valid for every particular LSB. The reproducibility of the strain measurements will be investigated in section 5.8 for both the BETSY- and the field measurements using the $F_y - \epsilon$ relations curves.

These reproducibility analyses are thus necessary to be able to draw meaningful conclusion about the question whether BETSY can be used to calibrate to LSBs. In the next section the force – strain relations are shown for the BETSY tests.

2.9.1.2 BETSY $F_y - \epsilon$ graphs

To start answering the question whether BETSY can be used to calibrate the LSB, in this section the force - strain curves are shown for the BETSY tests.

In Figure 34, six graphs are shown. Every graph shows again the relation between the lateral force and one particular strain gauge. For every graph one test run consisting of four experiments is used, see the legend.

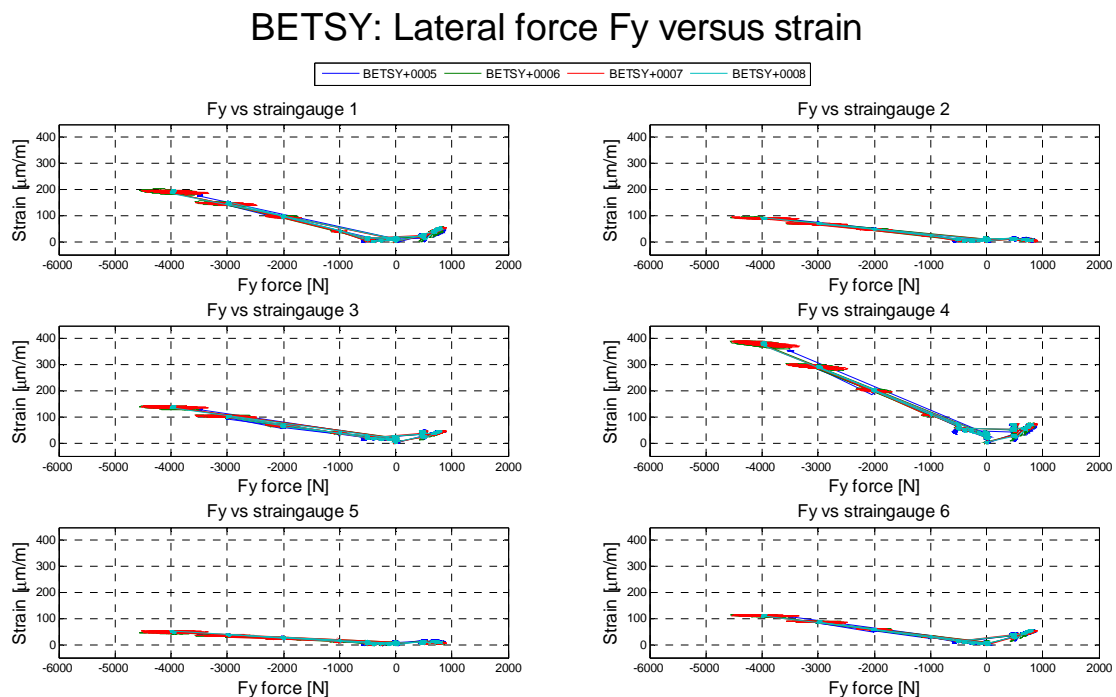


Figure 34 Lateral force vs. strain for tests performed at BETSY

In all graphs the typical V-shape is present that can be related to the absolute value problem. The same order of strain gauge sensitivity as for the field measurements can be observed; 4,1,3,6,2,5 from most sensitive to least sensitive strain gauge. Again, strain gauge 2 and 5 show hardly any response for left turning maneuvers, but do show response for right turning maneuvers.

In the next section it is shown to which extent the $F_y - \epsilon$ graphs for the field- and BETSY measurements are equivalent.

2.9.1.3 Comparison of the $F_y - \epsilon$ curves for tests at BETSY and tests performed in Papenburg

To get a better view about whether the strain gauge responses are comparable for the BETSY tests and the field measurements both responses are combined in Figure 35. Every graph in Figure 35 contains a $F_y - \epsilon$ curve for one strain gauge.

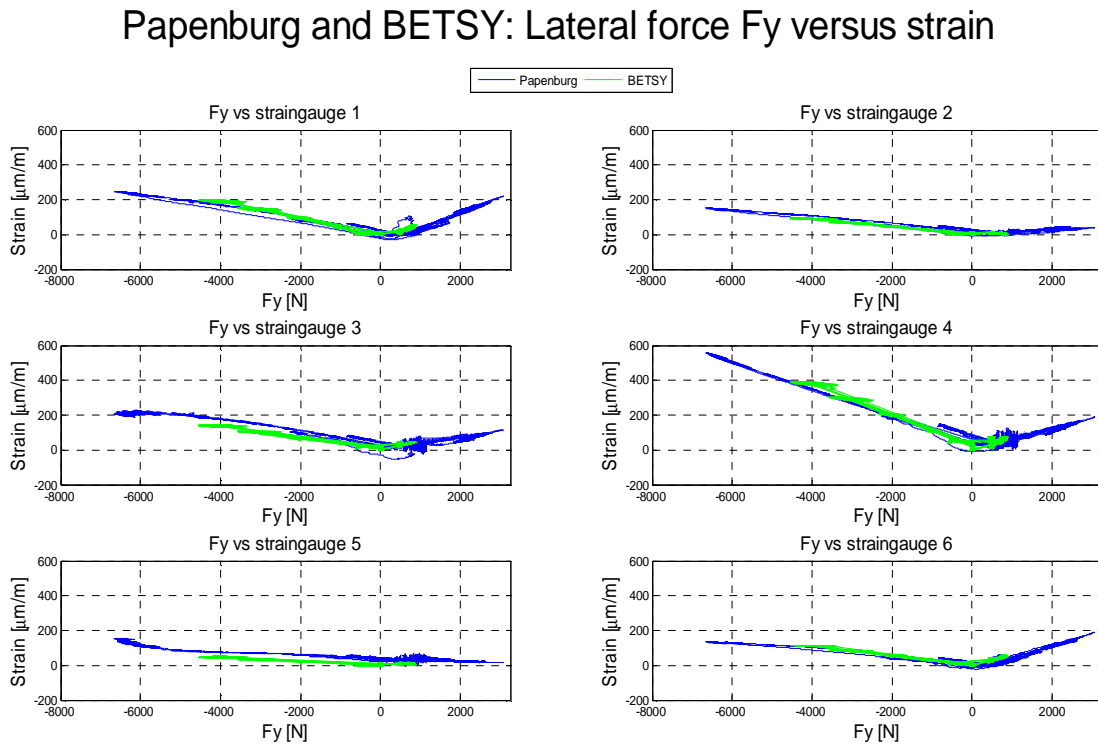


Figure 35 Lateral force vs. strain for tests performed at BETSY and in Papenburg

It has to be noticed from Figure 33 that a negative offset of 400 N was present in the measured lateral force F_y . This offset might have originated from an offset in the measured signal in rotated wheel frame of the measurement wheel which is used for the determination of the lateral force. Another cause may be the camber- and toe angle of the wheel. These angles introduce a lateral force on the wheel even while driving straight. Regardless of the cause, this offset have been compensated for in order to exclude the influence of the camber- and toe angle and to obtain zero lateral force when standing still or driving straight. In this way only the lateral force resulting from the introduction of a

slip angle (steering action) or a secondary effect like for example side wind influences the measured strain.

In section 2.6.2 it is explained that the offset in the strain gauges signals has also been compensated for. These offsets are the result of the static vertical loads of the vehicle like the weight and cargo of the vehicle. Thus, by removing the offsets in the signal, information about the vertical load is removed. One has to notice that for the estimation of the vertical force, this removed information is of great importance when one would like to estimate F_z . The vertical force estimation should therefore run simultaneous with the estimation of the lateral force. The offset-compensated signals can then be used for the lateral force estimation and the non-compensated signals for the vertical force estimation.

This implies that before any force estimation can start the offset in the strain gauge signals have to be determined and adjusted to zero. Figure 35 shows that the strain gauge responses for BETSY and Papenburg are comparable. To quantify the comparability, the V-shapes of all the F_y – strain curves will, in the next section, be described by two linear relations as explained in section 2.9.1.1.

2.9.1.4 Linear relations F_y - ϵ

In this section, the V-shapes of all the strain gauges will be described by two linear relations. One for left cornering and one for right cornering

$$\epsilon_{left} = c_{1,left} \cdot F_{y,left} + c_{2,left} \quad (2.5)$$

$$\epsilon_{right} = c_{1,right} \cdot F_{y,right} + c_{2,right} \quad (2.6)$$

One has to notice that by the sign convention the left cornering is associated with positive F_y and is thus located at the right side of the F_y – ϵ graph.

By describing the relations with two coefficients, c_1 and c_2 , transformation coefficients can be established to transform the relations measured during the tests performed at BETSY to the relations measured during the field measurements and vice versa. This will be the foundation of using BETSY as calibration system.

After checking the reproducibility of the measurements at BETSY and the measurements in the field in section 5.8 a solid ground is established to draw conclusions whether BETSY is usable as the calibration system of the LSB.

In Figure 36 the F_y – strain curves for BETSY are shown again, but now including two red lines approximating the left- and right- turning behaviour by a linear relation. In Figure 37 the same is done for the Papenburg measurements.

BETSY: Lateral force F_y versus strain including linear fits

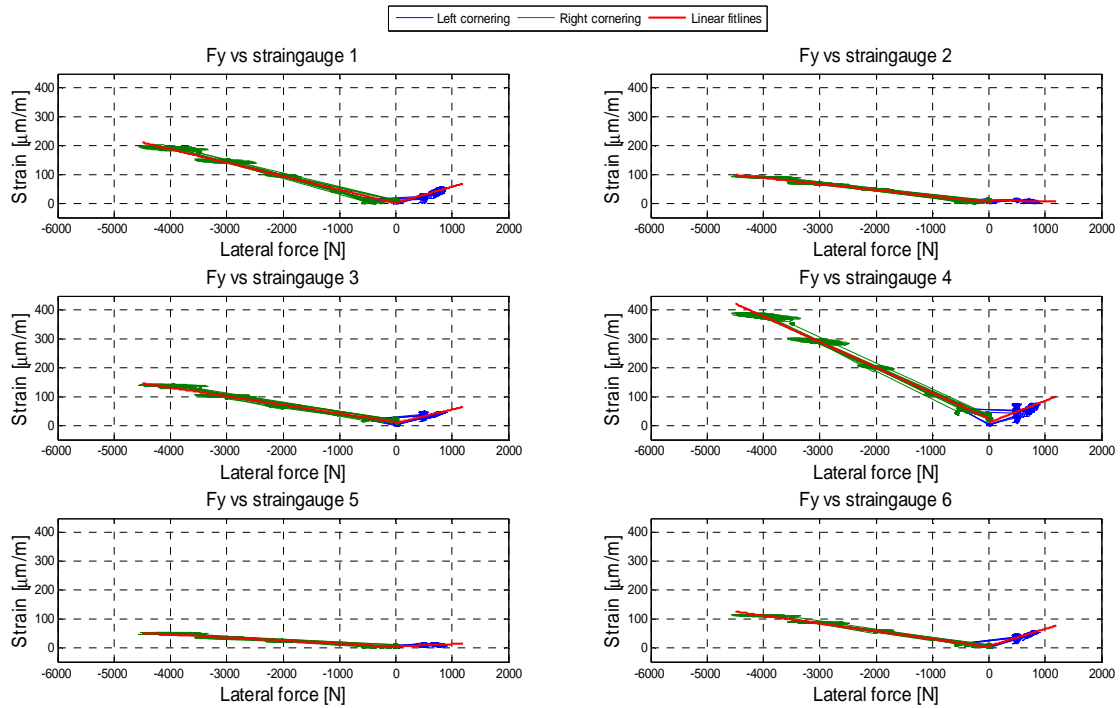


Figure 36 Lateral force vs. strain for tests performed at BETSY including linear fit lines

Papenburg: Lateral force F_y versus strain including linear fits

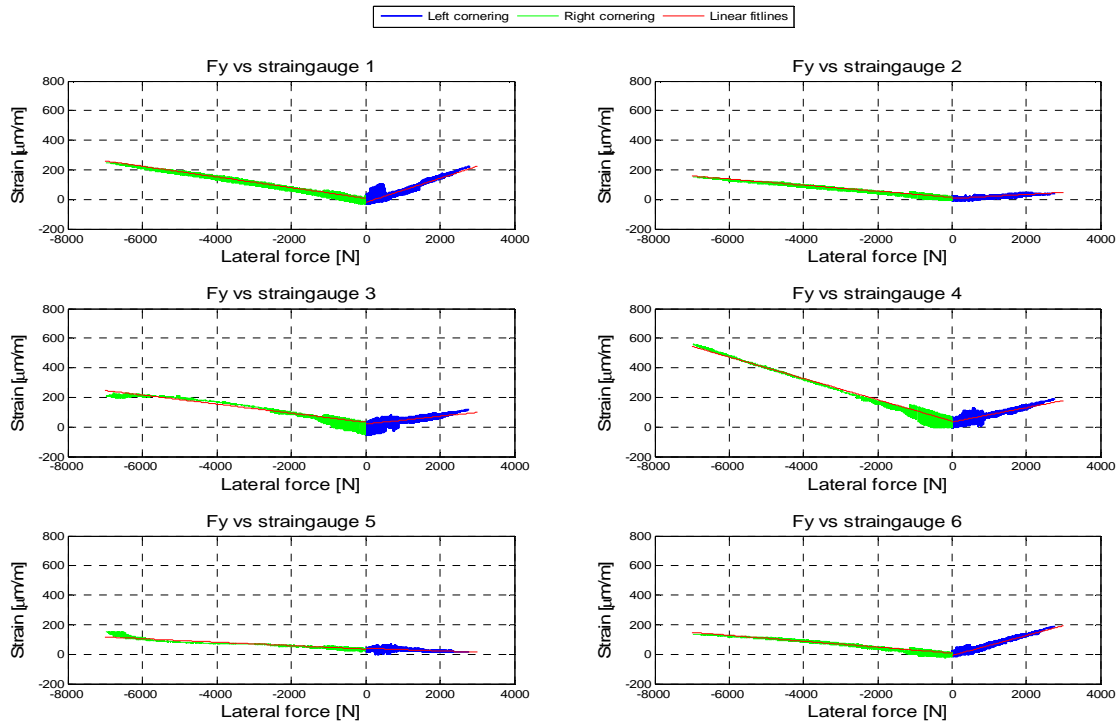


Figure 37 Lateral force vs. strain for tests performed at Papenburg including linear fit lines

In Table 6 the coefficients c_1 = slope and c_2 = offset of the linear fits are shown for BETSY and the Papenburg tests. Both tests are divided in a left and right part. Each left and right column is in turn divided in a column for the slope and a column for the offset.

Both the strain signals from the BETSY- and the field experiments have been compensated for the offsets in the conditioning process. Because this does not mean that the strain gauges show zero strain when no lateral force is applied, the coefficients c_2 and c_4 are non-zero. If they would have shown zero strain at zero lateral force, then ideally the c_2 and c_4 coefficients should be zero and could be left out of the analysis.

The offsets observed for the BETSY tests are almost constant as shown in Table 36. When comparing the field tests from Papenburg and SKF this is not true. For future work it is advised to set the strain signals in the vehicle to zero by adjusting the conditioner boxes. Only then the values in Table 6 and Table 36 will be constant. For the calibration process on BETSY it is necessary for the coefficients to be constant (reproducible), as explained in 2.9.1.1.

Table 6 F_y - strain linear fit coefficients

Strain gauge	BETSY				Papenburg			
	Right		Left		Right		Left	
	Slope [$\mu\text{m}/\text{m}/\text{N}$] = $c_{1,\text{right}}$	Offset [$\mu\text{m}/\text{m}$] = $c_{2,\text{right}}$	Slope [$\mu\text{m}/\text{m}/\text{N}$] = $c_{1,\text{left}}$	Offset [$\mu\text{m}/\text{m}$] = $c_{2,\text{left}}$	Slope [$\mu\text{m}/\text{m}/\text{N}$] = $c_{3,\text{right}}$	Offset [$\mu\text{m}/\text{m}$] = $c_{4,\text{right}}$	Slope [$\mu\text{m}/\text{m}/\text{N}$] = $c_{3,\text{left}}$	Offset [$\mu\text{m}/\text{m}$] = $c_{4,\text{left}}$
1	-0,047	0,107	0,057	-0,048	-0,036	8,179	0,081	-21,318
2	-0,021	3,714	-0,005	10,207	-0,021	14,660	0,013	6,806
3	-0,030	11,846	0,047	7,736	-0,031	32,007	0,026	19,061
4	-0,089	23,996	0,076	8,532	-0,072	40,423	0,048	32,782
5	-0,010	3,259	0,006	4,966	-0,012	35,555	-0,009	41,662
6	-0,027	2,311	0,060	4,266	-0,020	8,776	0,067	-8,664

When BETSY is used as calibration system a model will be obtained to transform the strain measured on BETSY to the forces applied to the LSB on BETSY. Therefore, in case of a LSB mounted in an actual vehicle, it is necessary to transform the strains measured in the vehicle to the strain which would be found on BETSY when loaded with the same lateral force.

In other words, when a lateral force $F_y = F_{y,\text{test}}$ is acting on the LSB, different strains will be measured dependent on whether the LSB is mounted on BETSY or in an actual vehicle.

For BETSY one finds

$$\varepsilon_{\text{BETSY}} = c_1 \cdot F_{y,\text{test}} + c_2 \quad (2.7)$$

whereas in the actual vehicle one would find

$$\varepsilon_{\text{vehicle}} = c_3 \cdot F_{y,\text{test}} + c_4 \quad (2.8)$$

When using BETSY as calibration system, a model will be available to transform $\varepsilon_{\text{BETSY}}$ to $F_{y,\text{test}}$. So as the strain in the actual vehicle $\varepsilon_{\text{vehicle}}$ can be transformed to $\varepsilon_{\text{BETSY}}$ an estimation can be given for the lateral force in the actual vehicle.

Thus, for a load $F_{y,\text{test}}$ one finds (2.7) on BETSY and (2.8) in the vehicle. When combining (2.7) and (2.8) and writing $F_{y,\text{test}}$ as a function of $\varepsilon_{\text{BETSY}}$ and $\varepsilon_{\text{vehicle}}$ one gets

$$F_{y,\text{test}} = \frac{\varepsilon_{\text{BETSY}} \cdot c_1 - c_2}{c_3} = \frac{\varepsilon_{\text{vehicle}} \cdot c_1 - c_4}{c_3} \quad (2.9)$$

a relation can be obtained to express $\varepsilon_{\text{BETSY}}$ as a function of $\varepsilon_{\text{vehicle}}$

$$\varepsilon_{\text{BETSY}} = \frac{c_1 \cdot (\varepsilon_{\text{vehicle}} - c_4)}{c_3} + c_2 = \frac{c_1 \cdot \varepsilon_{\text{vehicle}} - c_1 \cdot c_4}{c_3} + c_2 = c_A \cdot \varepsilon_{\text{vehicle}} + c_B \quad (2.10)$$

Where $c_A = \frac{c_1}{c_3}$ and $c_B = c_2 - \frac{c_1 \cdot c_4}{c_3}$

For both left and right cornering and for every strain gauge two parameters c_A and c_B are needed to transform $\varepsilon_{\text{vehicle}}$ to $\varepsilon_{\text{BETSY}}$. c_A can be seen as the slope transformation and c_B can be seen as the offset transformations factor. Table 7 shows all the coefficients.

Table 7 Transformation coefficients

Strain gauge	Right		Left	
	c_A	c_B	c_A	c_B
1	1,30	-10,55	0,70	14,81
2	1,03	-11,36	-0,36	12,66
3	0,97	-19,35	1,80	-26,49
4	1,23	-25,87	1,59	-43,53
5	0,90	-28,63	-0,66	32,46
6	1,36	-9,64	0,89	11,98

Ideally $c_A = c_B = 1$. Table 7 shows that there are differences between the $F_y - \varepsilon$ curves for the BETSY and the field measurements. Slope and offset differences, c_A and c_B , for left and right cornering can be observed.

The slope transformation c_A for right maneuvers shows differences in sensitivity up 36% for strain gauge 6. For left turning maneuvers strain gauge 2 and 5 show hardly any response and will be taken out of the analysis. When excluding these two strain gauges still differences in the slope transformation c_A starting from 11% up to 80% for left cornering are found.

A couple of causes can be mentioned to explain the differences.

- The first can be accounted to compliance differences. This was the problem during the earlier BETSY tests where the LSB was mounted on BETSY via a stiff disc, and this issue remained in the tests with a flexible disc and a knuckle which was rigidly fixed. There are still differences in the final set-up where the LSB is connected to BETSY with knuckle + ball joints. This compliance difference can originate from different cases.

- Difference in pre-tension of the balls between the inner- and outer ring

- Differences in mounting torque of the bolts which connect the bearing to the knuckle
 - Differences in the surrounding stiffness. Whereas on BETSY the bearing is connected to the plate, where the forces are applied, via the knuckle with ball joints. In the real vehicle these ball joints are connected via supporting arms and rubbers to the chassis.
- A second cause for the difference can be accounted to differences in the coordinate system. Whereas in the vehicle the LSB is positioned as in the left of Figure 38, the LSB is slightly rotated when mounted on BETSY as shown in the right of Figure 38. Due to this difference in mounting angle the BETSY test set-up is slightly different from the set-up in the actual vehicle and differences are introduced.

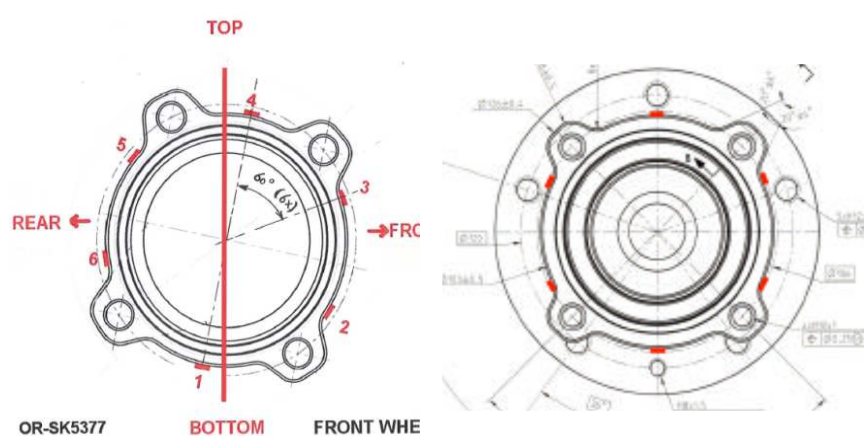


Figure 38 Left: LSB in vehicle. Right: LSB on BETSY

2.10 Conclusions

In this chapter several aspects have been dealt with. The chapter began with an introduction to BETSY and to measurements performed in the field. A sign convention is established to define the positive and negative directions of the load. The signal conditioning process of all the measured signals has been discussed. A global analysis has been done with respect to the measured strains and forces to justify the correctness of what was seen during the measurements and the established sign convention.

In the last paragraph the $F_y - \varepsilon$ curves are given. Hereby we have encountered the ‘absolute value problem’ and have observed that there are still differences between what is measured in the vehicle and what is measured on BETSY (where the LSB is mounted on BETSY including the knuckle and ball joints).

A method is given to correct for these differences. So to transform the $F_y - \varepsilon$ relations found on BETSY to the $F_y - \varepsilon$ found in the vehicle and vice versa.

To answer the question if BETSY can be used for calibration it is necessary that the observed differences (Table 7) are structural so that the measurements are reproducible to a certain level. As well as what is measured on BETSY as what is measured in the

vehicle needs to be reproducible in order to transform the one to the other using the coefficients in Table 7. The reproducibility analysis is given in Chapter 5. A set of transformation coefficients is determined based on a different set of tests performed on BETSY and in the field. The conclusion will therefore be saved until Chapter 5.

3 Lateral force estimation by the deformation of the bearing outer ring using a Multivariate Linear Regression Analysis

In this chapter the deformations of the outer ring of the LSB will be used for estimation of the lateral force F_y . A Multivariate Linear Regression Analysis (MLRA)(Douglas C. Montgomery) will be derived for the estimation of the lateral force F_y and implemented in Matlab.

In section 3.1 it will be discussed what a MLRA analysis is. It will be applied to the measurements performed at BETSY and the results will be shown. Then in section 3.2 to section 3.5 refinements of MLRA will be treated which will increase the accuracy of the lateral force estimation. First, in section 3.2 the data will be divided into two sections. One for left cornering maneuvers ($F_y > 0$) and one for right cornering maneuvers ($F_y < 0$). This will then result into two MLRAs which will be used for lateral force estimation separately. In section 3.3 another separation is introduced. This time in the frequency domain. In section 3.4 it will be discussed what or order of the MLRA is best suitable for the purpose. Then in section 3.5 it is investigated if the accuracy can be further improved by taking out the strain gauges which show the lowest correlation with the applied lateral force. Finally in section 3.6 the chapter will be summarized with a conclusion.

3.1 Multivariate Linear Regression Analysis

For the estimation of the lateral force F_y a MLRA will be used. With a MLRA the output is assumed to be a linear combination of the measured strains and possibly higher order terms of the strains ε , ε^2 , ε^3 , .. and a constant term β_0 , see (3.1).

$$F_{t_k} = \beta_0 + \beta_1 \varepsilon_{t_k} + \beta_2 \varepsilon_{t_k}^2 + \dots + \beta_n \varepsilon_{t_k}^n + E_{t_k} \quad (3.1)$$

Where

F_{t_k} = Output forces/moments on time instant t_k , for $k = \{1, 2, 3, \dots, N\}$, with N the number of samples

β_i = Parameters to be determined, for $i = \{1, 2, 3, \dots, n\}$, with n the highest order

ε^i = Measured strains at the circumference of the bearing, for $i = \{1, 2, 3, \dots, n\}$

E_{t_k} = Error at time instant t_k

Although the right hand side contains quadratic and higher order terms of ε it is linear in the coefficients β_i .

The estimated force is given by

$$\hat{F}_{t_k} = \beta_0 + \beta_1 \varepsilon_{t_k} + \beta_2 \varepsilon_{t_k}^2 + \dots + \beta_n \varepsilon_{t_k}^n \quad (3.2)$$

This results in the error

$$E = F - \hat{F} \quad (3.3)$$

The coefficients β_i will be calculated in a linear least square way to minimize the error squared.

$$\underbrace{\sum_{k=1}^N E(\beta_i)^2}_{\text{minimal}} = \sum_{k=1}^N (F_{t_k} - \hat{F}_{t_k})^2 = \sum_{k=1}^N (F_{t_k} - \beta_0 - \beta_1 \varepsilon_{t_k} - \beta_2 \varepsilon_{t_k}^2 - \dots - \beta_n \varepsilon_{t_k}^n)^2 \quad (3.4)$$

Three forces and three moments can act on the bearing: F_x , F_y , F_z , M_x , M_y and M_z . The focus in this thesis is towards the estimation the lateral force F_y . The implementation in Matlab however is focused on F_y and F_z . The equations can easily be extended to include the omitted forces and moments. With six inputs and two outputs this becomes

$$\underbrace{[F]}_{2 \times N} = \underbrace{[\beta_0]}_{2 \times 1} \underbrace{[1]}_{1 \times N} + \underbrace{[\beta_1]}_{2 \times 6} \underbrace{[\varepsilon]}_{6 \times N} + \underbrace{[\beta_2]}_{2 \times 6} \underbrace{[\varepsilon^2]}_{6 \times N} + \dots + \underbrace{[\beta_n]}_{2 \times 6} \underbrace{[\varepsilon^n]}_{6 \times N} + \underbrace{[E]}_{6 \times N} \quad (3.5)$$

Where $[\beta_0][1]$ represents the constant term, $[\beta_1][\varepsilon]$ the first order term and $[\beta_n][\varepsilon^n]$ the n-th order term.

$$\text{With } [F] = \begin{bmatrix} F_y \\ F_z \end{bmatrix} = \begin{bmatrix} F_{y,t_k} & \dots & F_{y,t_N} \\ F_{z,t_k} & \dots & F_{z,t_N} \end{bmatrix}, [\beta_0] = \begin{bmatrix} \beta_{0,F_y} \\ \beta_{0,F_z} \end{bmatrix}$$

$$[\beta_1] = \begin{bmatrix} \beta_{11,F_y} & \beta_{21,F_y} & \beta_{31,F_y} & \beta_{41,F_y} & \beta_{51,F_y} & \beta_{61,F_y} \\ \beta_{11,F_z} & \beta_{21,F_z} & \beta_{31,F_z} & \beta_{41,F_z} & \beta_{51,F_z} & \beta_{61,F_z} \end{bmatrix}, [\varepsilon] = \begin{bmatrix} \varepsilon_{1,t_k} & \dots & \varepsilon_{1,t_N} \\ \varepsilon_{2,t_k} & \dots & \varepsilon_{2,t_N} \\ \varepsilon_{3,t_k} & \dots & \varepsilon_{3,t_N} \\ \varepsilon_{4,t_k} & \dots & \varepsilon_{4,t_N} \\ \varepsilon_{5,t_k} & \dots & \varepsilon_{5,t_N} \\ \varepsilon_{6,t_k} & \dots & \varepsilon_{6,t_N} \end{bmatrix}$$

$$[\beta_2] = \begin{bmatrix} \beta_{12,F_y} & \beta_{22,F_y} & \beta_{32,F_y} & \beta_{42,F_y} & \beta_{52,F_y} & \beta_{62,F_y} \\ \beta_{12,F_z} & \beta_{22,F_z} & \beta_{32,F_z} & \beta_{42,F_z} & \beta_{52,F_z} & \beta_{62,F_z} \end{bmatrix}, [\varepsilon^2] = \begin{bmatrix} \varepsilon_{1,t_k}^2 & \dots & \varepsilon_{1,t_N}^2 \\ \varepsilon_{2,t_k}^2 & \dots & \varepsilon_{2,t_N}^2 \\ \varepsilon_{3,t_k}^2 & \dots & \varepsilon_{3,t_N}^2 \\ \varepsilon_{4,t_k}^2 & \dots & \varepsilon_{4,t_N}^2 \\ \varepsilon_{5,t_k}^2 & \dots & \varepsilon_{5,t_N}^2 \\ \varepsilon_{6,t_k}^2 & \dots & \varepsilon_{6,t_N}^2 \end{bmatrix}$$

Where ε_{m,t_k} is the measured strain of strain gauge m at time t_k , for $1 < m < 6$ and $1 < k < N$ with N the number of samples.

The matrices β_i , for $i = \{1, 2, 3, \dots, n\}$, with n the order of the MLRA, contain the coefficients to be determined. In the matrices the coefficients $\beta_{mi,F}$ represent the coefficient for strain gauge m with order i to output F for $1 < m < 6, 1 < i < n$ and $F = \{F_y, F_z\}$

We can also write \hat{F} (3.2) as the following sum

$$\hat{F} = \begin{bmatrix} 6 \times 1 \\ \beta_0 \end{bmatrix} \begin{bmatrix} 1 \times N \\ 1 \end{bmatrix} + \sum_{i=1}^n \begin{bmatrix} \beta_{1i,F_y} & \beta_{2i,F_y} & \beta_{3i,F_y} & \beta_{4i,F_y} & \beta_{5i,F_y} & \beta_{6i,F_y} \\ \beta_{1i,F_z} & \beta_{2i,F_z} & \beta_{3i,F_z} & \beta_{4i,F_z} & \beta_{5i,F_z} & \beta_{6i,F_z} \end{bmatrix} \begin{bmatrix} \varepsilon_{1,t_k}^i & \dots & \varepsilon_{1,t_N}^i \\ \varepsilon_{2,t_k}^i & \dots & \varepsilon_{2,t_N}^i \\ \varepsilon_{3,t_k}^i & \dots & \varepsilon_{3,t_N}^i \\ \varepsilon_{4,t_k}^i & \dots & \varepsilon_{4,t_N}^i \\ \varepsilon_{5,t_k}^i & \dots & \varepsilon_{5,t_N}^i \\ \varepsilon_{6,t_k}^i & \dots & \varepsilon_{6,t_N}^i \end{bmatrix} \quad (3.6)$$

The coefficients $\beta_{mi,F}$ will again be calculated in a linear least square way to minimize the error squared.

$$\underbrace{\sum_{k=1}^N [E(\beta_i)]^2}_{\text{minimal}} = \sum_{k=1}^N \left([F]_{t_k} - [\hat{F}]_{t_k} \right)^2 = \sum_{k=1}^N \left([F]_{t_k} - [\beta_0][1] - [\beta_1][\varepsilon]_{t_k} - \dots - [\beta_n][\varepsilon]^n \right)^2 \quad (3.7)$$

Expanding (3.7) in all its terms gives:

$$F_y = \beta_{0,F_y} + \beta_{11,F_y} \varepsilon_1^1 + \beta_{21,F_y} \varepsilon_2^1 + \dots + \beta_{61,F_y} \varepsilon_6^1 + \beta_{12,F_y} \varepsilon_1^2 + \beta_{22,F_y} \varepsilon_2^2 + \dots + \beta_{62,F_y} \varepsilon_6^2 + \dots + \sum_{m=1}^6 \beta_{mn,F_y} \varepsilon_m^n$$

$$F_z = \beta_{0,F_z} + \beta_{11,F_z} \varepsilon_1^1 + \beta_{21,F_z} \varepsilon_2^1 + \dots + \beta_{61,F_z} \varepsilon_6^1 + \beta_{12,F_z} \varepsilon_1^2 + \beta_{22,F_z} \varepsilon_2^2 + \dots + \beta_{62,F_z} \varepsilon_6^2 + \dots + \sum_{m=1}^6 \beta_{mn,F_z} \varepsilon_m^n$$

The equations can be written in a more compact matrix form as

$$[F] = [\beta][\varepsilon_{total}] = \begin{bmatrix} [\beta_0] & [\beta_1] & [\beta_2] & \dots & [\beta_n] \end{bmatrix} \begin{bmatrix} [1] \\ [\varepsilon] \\ [\varepsilon]^2 \\ \dots \\ [\varepsilon]^n \end{bmatrix} \quad (3.8)$$

Where

$$\begin{aligned}
 [F] &= \begin{bmatrix} F_y \\ F_z \end{bmatrix} \\
 [\beta] &= \begin{bmatrix} \beta_{0,F_y} & \beta_{11,F_y} & \beta_{12,F_y} & \cdots & \beta_{61,F_y} & \beta_{12,F_y} & \beta_{22,F_y} & \cdots & \beta_{62,F_y} & \cdots & \beta_{1n,F_y} & \beta_{2n,F_y} & \cdots & \beta_{6n,F_y} \\ \beta_{0,F_z} & \beta_{11,F_z} & \beta_{21,F_z} & \cdots & \beta_{61,F_z} & \beta_{12,F_z} & \beta_{22,F_z} & \cdots & \beta_{62,F_z} & \cdots & \beta_{1n,F_z} & \beta_{2n,F_z} & \cdots & \beta_{6n,F_z} \end{bmatrix} \\
 &= \begin{bmatrix} [\beta_0] & [\beta_1] & [\beta_2] & \cdots & [\beta_n] \end{bmatrix} \\
 [\varepsilon_{total}] &= \begin{bmatrix} 1 & \cdots & 1 \\ \varepsilon_{1,t_k} & \cdots & \varepsilon_{1,t_N} \\ \varepsilon_{2,t_k} & \cdots & \varepsilon_{2,t_N} \\ \cdots & & \\ \varepsilon_{6,t_k} & \cdots & \varepsilon_{6,t_N} \\ \varepsilon_{1,t_k}^2 & \cdots & \varepsilon_{1,t_N}^2 \\ \varepsilon_{2,t_k}^2 & \cdots & \varepsilon_{2,t_N}^2 \\ \cdots & & \\ \varepsilon_{6,t_k}^2 & \cdots & \varepsilon_{6,t_N}^2 \\ \cdots & & \\ \varepsilon_{1,t_k}^n & \cdots & \varepsilon_{1,t_N}^n \\ \varepsilon_{2,t_k}^n & \cdots & \varepsilon_{2,t_N}^n \\ \cdots & & \\ \varepsilon_{6,t_k}^n & \cdots & \varepsilon_{6,t_N}^n \end{bmatrix} = \begin{bmatrix} [\varepsilon]^0 \\ [\varepsilon]^1 \\ [\varepsilon]^2 \\ \cdots \\ [\varepsilon]^n \end{bmatrix}
 \end{aligned}$$

When expanding to more outputs extra rows can easily be added to the matrices $[F]$ and $[\beta]$.

The matrix with coefficients can be calculated by first multiplying the left and right side of the equation (3.8) by ε^T to get a square matrix which can be inverted

$$[F][\varepsilon_{total}]^T = [\beta][\varepsilon_{total}][\varepsilon_{total}]^T \quad (3.9)$$

Then by taking the inverse of $\varepsilon_{total}\varepsilon_{total}^T = (\varepsilon_{total}\varepsilon_{total}^T)^{-1}$ and post multiplying both sides of equation (3.9) with this inverse, this results in

$$[F][\varepsilon_{total}]^T ([\varepsilon_{total}][\varepsilon_{total}]^T)^{-1} = [\beta][\varepsilon_{total}][\varepsilon_{total}]^T ([\varepsilon_{total}][\varepsilon_{total}]^T)^{-1} = [\beta][I] \quad (3.10)$$

And finally

$$[\beta] = [F][\varepsilon_{total}]^T ([\varepsilon_{total}][\varepsilon_{total}]^T)^{-1} \quad (3.11)$$

3.1.1 Result

The matrix β is determined by using seven different BETSY experiments. Subsequently an eighth experiment is used to determine the accuracy of a force estimation using this matrix β . The calibration experiments that are selected are: BMW+0005, BMW+0007, BMW+0008 and the experiments BMW+0015 to BMW+0018. Experiment BMW+0006 is used for the validation.

The quality of the estimation of the lateral force will be quantified through the root mean squared error

$$RMSE = \sqrt{\frac{1}{N} \sum_{k=1}^{k=N} E^2} \quad (3.12)$$

Where E is the estimation error at time sample k and N is the total amount of samples.

Figure 41 shows the error distribution of the upcoming estimation. The error is approximately Gaussian distributed. A further quantification will therefore be given by the mean and standard deviation of the estimation error.

$$f(x; \mu, \sigma^2) = \frac{1}{\sigma\sqrt{2\pi}} e^{-\frac{1}{2}\left(\frac{x-\mu}{\sigma}\right)^2} \quad (3.13)$$

Where μ is the mean or expected value, σ^2 the variance and σ the standard deviation.

When a variable has a normal distribution, 68% of the values lie within one standard deviation σ away from the mean, 95% lie within two standard deviations from the mean and 99.7% lie within three standard deviations away from the expected value.

Therefore the standard deviation σ provides information about the lower- and upper bound of the estimation error. The lower- and upper bound are given by

$$\mu - 3\sigma > E > \mu + 3\sigma \quad (3.14)$$

Figure 39 shows the applied- and estimated force. The applied force is shown in blue and the estimated one in green. Figure 40 shows the estimated force versus the applied force.

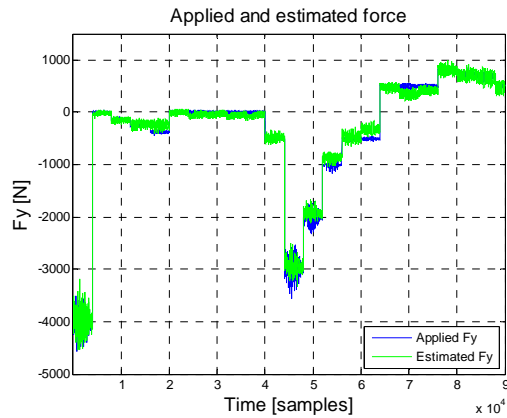


Figure 39 Applied and estimated lateral force

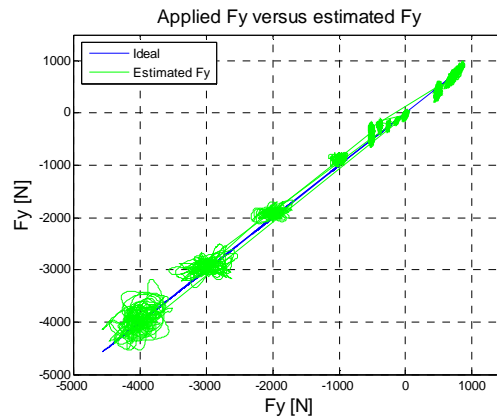


Figure 40 Applied force plotted versus the estimated force

Table 8 shows the quantification of the estimation error. A RMS-error 108 N (8.85%) is obtained. Figure 41 shows the distribution of the estimation error.

Table 8 Estimation error

RMS error [N]	Mean μ [N]	Standard deviation σ [N]	RMS Applied F_y [N]	Percent error [%]
108,17	-11,3	107,59	1222,00	8,85

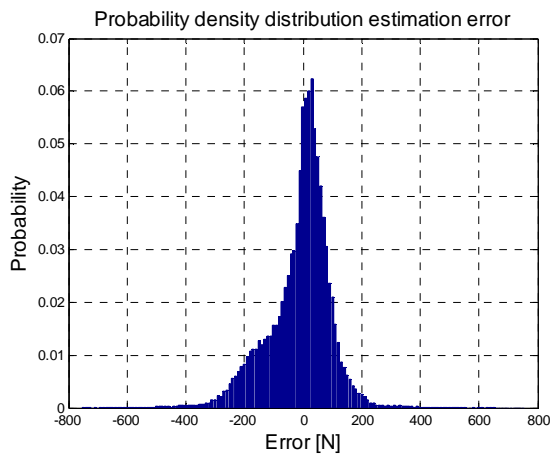


Figure 41 Error distribution

3.2 Separate estimation for positive- and negative lateral force

The first step in improving the lateral force estimation in the previous section is to treat the left- and right cornering behaviour separately. As seen in section 2.9, the force-strain graphs are piecewise linear with two linear segments, $F_y < 0$ and $F_y > 0$. To improve the estimation a MLRA analysis will be performed on both segments. This approach is motivated by:

Difference in sensitivity for positive and negative lateral force

By looking at the $F_y - \varepsilon$ graphs in section 2.9 different sensitivities can be observed for positive lateral force ($F_y > 0$) and negative lateral force ($F_y < 0$). The difference in sensitivity is quantified by the slopes for the positive and negative F_y in the $F_y - \varepsilon$ graphs. These slopes are shown in Table 36.

Correlation coefficients

When looking at the correlation coefficients between the applied F_y and the measured strain a difference in correlation is observed for both positive- and negative F_y and strain, indicating a difference in response. The second column of Table 9 shows the correlation coefficient between the applied F_y and measured strain wherefore left and right are not partitioned. For the last two columns the left and right cornering data has been separated.

Table 9 Correlation between force and strain

Strain gauge	Correlation coefficient between F_y and strain		
	R_{xy}	$R_{xy,left}$	$R_{xy,right}$
1	-0,82	0,95	-0,98
2	-0,92	-0,73	-0,97
3	-0,80	0,40	-0,99
4	-0,91	0,42	-1,00
5	-0,86	0,03	-0,96
6	-0,64	0,87	-0,99

An increase in correlation for negative F_y is observed whereas a decrease is observed in correlation for positive F_y . Even though a decrease is observed in correlation for positive F_y a better estimation of F_y is expected for both positive and negative lateral force, because the calibration matrices will be solely based on their own behaviour. The increase in accuracy can be found in section 3.2.1. The separation between positive and negative lateral force is manually performed by looking at the applied load profile. The first 16 of the 24 load steps consist of negative F_y and represent right cornering maneuvers whereas the last 8 load steps consist of positive F_y and represent left cornering maneuvers. When implemented in an actual vehicle this separation is less straightforward, because the strain gauges suffer from the 'absolute value' problem. Therefore an extra sensor is needed for the determination of the direction. In the next chapter this extra sensor, the Eddy-current sensor, will be introduced.

3.2.1 Result: Left, right and total

Figure 42 and Figure 43 show the result of using separate calibration matrices for positive and negative F_y . These matrices will be called β_{left} and β_{right} . The matrix β from the previous section will from now on be called the β_{global} , the global calibration matrix, because it is based on all data. In the upper graph the force is estimated by only using the calibration matrix β_{left} which is calculated by left cornering data, thus $F_y > 0$. It shows that when using this matrix only the positive lateral force is estimated accurately. For the middle graph the estimation is based on the calibration matrix calculated by right cornering data β_{right} and only the negative lateral force is estimated accurately. In the lower graph both are combined to have a more accurate estimated over the full range of lateral force.

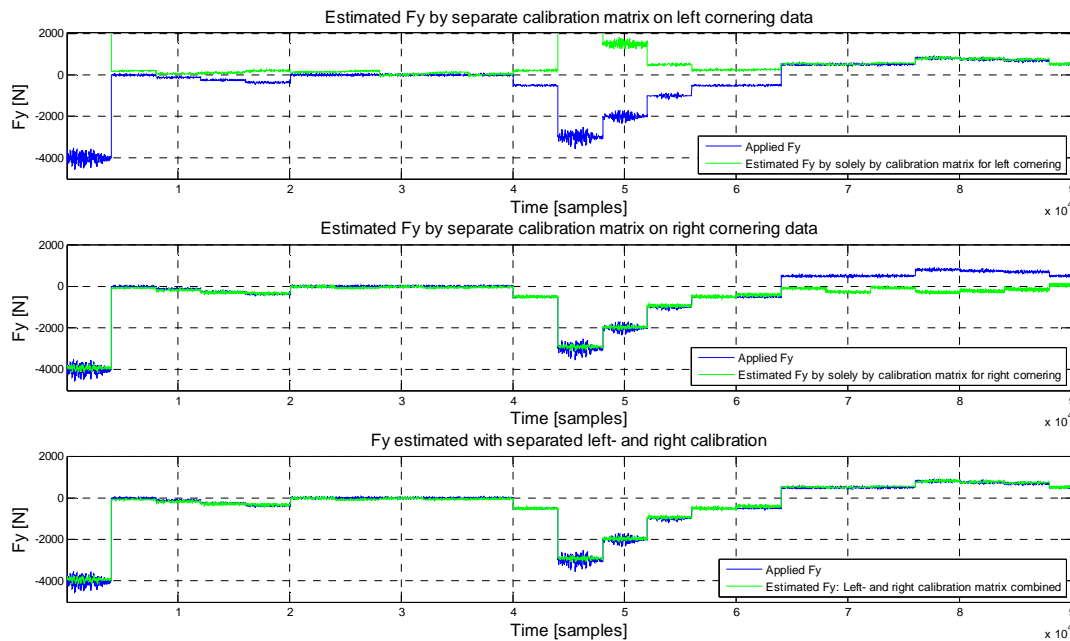


Figure 42 F_y estimation where two calibration matrices are used. One for left- and one for right cornering data. Upper plot: . Middle plot: Estimation using calibration matrix calculated by right cornering data. Lower plot: Combined estimation

Figure 43 shows the estimated force versus the applied force. In magenta the estimated force using the matrix β_{left} is shown and in cyan the estimated force using a matrix β_{right} based on negative F_y . The deviation from the ideal blue line indicated that only a certain range of F_y is estimated in an accurate way for both estimations.

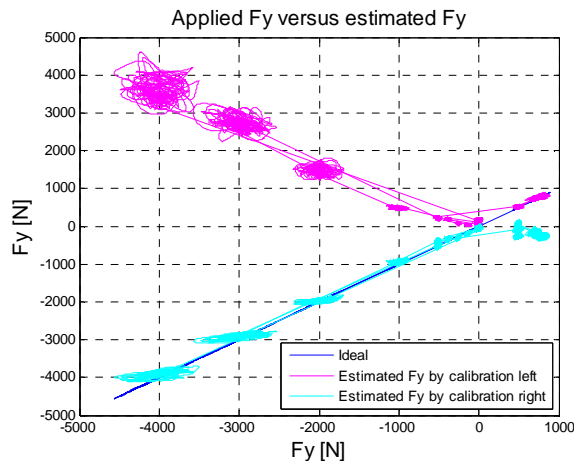


Figure 43 applied force versus the estimated force where a calibration is performed on left- and right cornering data separately

Table 10 shows the improvement of the accuracy when using two calibration matrices. Whereas for the global calibration matrix an error of 13.15 % and 9.59 % is obtained for the positive and negative F_y respectively, errors of 7.44% and 7.15% are obtained when using separate matrices.

Table 10 Accuracy improvement of the left/right separation

	RMS error [N]	Mean μ [N]	Standard deviation σ [N]	RMS Applied F_y [N]	Percent error [%]
Left determined by own calibration	46,26	-25,72	38,45	621,81	7,44
Right determined by own calibration	87,40	-4,92	87,26	1222,50	7,15
Left determined by global calibration	81,77	41,88	70,24	621,81	13,15
Right determined by global calibration	117,21	-32,90	112,50	1222,50	9,59

Figure 44 shows the estimation results using global and separate matrices. The estimated F_y is plotted versus time as well as versus the applied force. Table 11 shows the quantization of the error for the estimation using separate matrices.

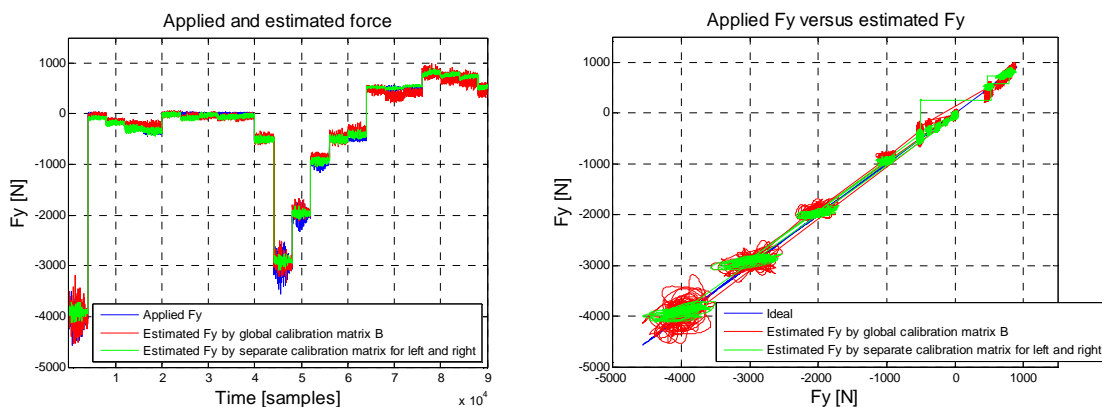


Figure 44 F_y estimation using a global and separate calibration matrices.

A RMS-error of 77.78 N (5.58%) is obtained, whereas an error of 108.17 N (8.85%) was obtained when using a global matrix.

Table 11 Error quantification using separate calibration matrices for positive and negative F_y

RMS error [N]	Mean μ [N]	Standard deviation σ [N]	RMS Applied F_y [N]	Percent error [%]
77,78	-10,93	77,01	1394,50	5,58

3.3 Separation into two frequency bands

The second step in improving the lateral force estimation of the previous section is to introduce two frequency bandwidths and treat the behaviour of the two bandwidths separately. The two frequency bands will consist of a low frequent semi-static bandwidth, 0 Hz to 1 Hz, and a high frequent dynamic bandwidth, 1 Hz – 10 Hz.

A MLRA analysis will then be performed on left- and right cornering data but also on both frequency bands separately. This approach is motivated by:

Difference in response

A difference in response is observed when separating the applied force and strain into two frequency bands. Figure 45 shows this idea. For every load step the content is divided into two frequency regions. The dynamic part of the measured strain has been approximated by a first order polynomial as a function of the applied force. These approximation do not coincide with the observed V-shape which indicates the strain gauge response of the low frequent content of force and strain.

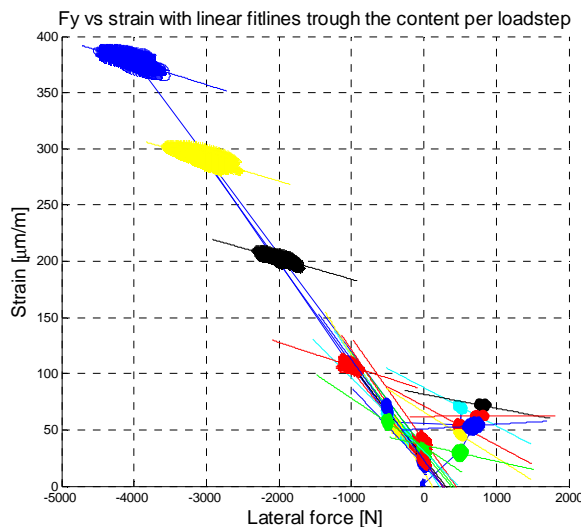


Figure 45 Lateral force vs. strain with linear fit lines through the content per load step

Absolute value problem/temperature induced strain in low frequent content

As is discussed in the Chapter 2.9.1.1, the direction of the lateral force cannot be distinguished using the strain gauges because of the absolute value problem. Also the strain gauges are subject to low frequent drift due to temperature induced strain. Because of this low frequent contamination in the frequency domain an extra degree of freedom will be introduced in Chapter 4 to substitute the strain gauges in the semi-static frequency region to solve these problems. Therefore a separation in the frequency domain is carried out.

Correlation

Table 12 and Table 13 show the correlation coefficients R_{xy} for the static and dynamic parts for positive and negative lateral force respectively. The first column shows that for the semi-static content a slight increase in correlation is introduced. For the dynamic part coefficients smaller than 0.05 are found, indicating uncorrelated response of the strain gauges to dynamic changes in load.

Table 12 Correlation coefficients between applied F_y and measured strain for positive lateral force

Strain gauge	Correlation coefficient between F_y and strain for positive F_y		
	$R_{xy, \text{left}}$	$R_{xy, \text{left}}$, semi-static content	$R_{xy, \text{left}}$, dynamic content
1	0,95	0,96	0,00
2	-0,73	-0,87	0,01
3	0,40	0,40	0,03
4	0,42	0,45	-0,03
5	0,03	0,01	-0,04
6	0,87	0,88	0,01

Table 13 Correlation coefficients between applied F_y and measured strain for negative lateral force

Strain gauge	Correlation coefficient between F_y and strain for negative F_y		
	$R_{xy, \text{right}}$	$R_{xy, \text{right}}$, semi-static content	$R_{xy, \text{right}}$, dynamic content
1	-0,98	-0,98	-0,02
2	-0,97	-0,97	0,02
3	-0,99	-0,99	0,00
4	-1,00	-1,00	0,00
5	-0,96	-0,97	0,03
6	-0,99	-0,99	-0,02

The low correlation coefficients of the dynamic content indicate that little useful information is contained within that bandwidth and that the higher frequent content only disturbs the lower frequent content. Despite the disappointing dynamic response, in the next section a model will be derived including these dynamics.

3.3.1 Theory MLRA

As motivated in sections 3.2 and in this section 3.3 the signals are divided in a part representing left cornering maneuvers and a part representing right cornering maneuvers. Besides that separation both part are divided in a semi-static- and dynamic part. This results in four different sections.

- 1) The low frequent content representing the left cornering behaviour.
- 2) The low frequent content representing the right cornering behaviour.
- 3) The high frequent content representing the left cornering behaviour.
- 4) The high frequent content representing the right cornering behaviour.

For the four different datasets, a matrix β with parameters for a MLRA will be determined.

The four different matrices which have to be determined are called $\beta_{low_frequent,left}$, $\beta_{low_frequent,right}$, $\beta_{high_frequent,left}$, $\beta_{high_frequent,right}$. Where the subscripts ‘low_frequent’ and ‘high_frequent’ refer to the low- and high frequent content of the data and the subscripts ‘left’ and ‘right’ refer to the left- and right cornering behaviour respectively. In the same way the estimated forces belonging to the four different cases will be denoted by $F_{low_frequent,left}$, $F_{low_frequent,right}$, $F_{high_frequent,left}$ and $F_{high_frequent,right}$ and the strains by $\epsilon_{low_frequent,left}$, $\epsilon_{low_frequent,right}$, $\epsilon_{high_frequent,left}$ and $\epsilon_{high_frequent,right}$

The total estimated force is the sum of the four forces estimated by the four separations:

$$\begin{aligned} F_{total} &= F_{low_frequent,left} + F_{low_frequent,right} + F_{high_frequent,left} + F_{high_frequent,right} \\ &= \beta_{low_frequent,left} \cdot \epsilon_{low_frequent,left} + \beta_{low_frequent,right} \cdot \epsilon_{low_frequent,right} \\ &\quad + \beta_{high_frequent,left} \cdot \epsilon_{high_frequent,left} + \beta_{high_frequent,right} \cdot \epsilon_{high_frequent,right} \end{aligned} \quad (3.15)$$

This gives us in matrix form the following equation

$$[F] = \begin{bmatrix} [\beta_{low_frequent,left}] \\ [\beta_{low_frequent,right}] \\ [\beta_{high_frequent,left}] \\ [\beta_{high_frequent,right}] \end{bmatrix}^T \begin{bmatrix} [\epsilon_{low_frequent,left}] \\ [\epsilon_{low_frequent,right}] \\ [\epsilon_{high_frequent,left}] \\ [\epsilon_{high_frequent,right}] \end{bmatrix} = [\beta][\epsilon] \quad (3.16)$$

Where for the low frequent, left part it holds

$$[F] = \begin{bmatrix} F_y \\ F_z \end{bmatrix}$$

$$[\beta_{low_frequent,left}] = \begin{bmatrix} [\beta_{0,low_frequent,left}] & [\beta_{1,low_frequent,left}] & [\beta_{2,low_frequent,left}] & [\beta_{n,low_frequent,left}] \end{bmatrix}$$

$$[\epsilon_{low_frequent,left}] = \begin{bmatrix} [1] \\ [\epsilon_{low_frequent,left}] \\ [\epsilon_{low_frequent,left}]^2 \\ \dots \\ [\epsilon_{low_frequent,left}]^n \end{bmatrix}$$

The remaining matrices for the high frequent left- and right behaviour and the low frequent right behaviour are constructed in the same way.

As in section 3.1, the calibration matrices are calculated by

$$\left[\beta_{low_frequent,lef} \right] = \left[F_{low_frequent,lef} \right] \left[\epsilon_{low_frequent,lef} \right]^T \left(\left[\epsilon_{low_frequent,lef} \right] \left[\epsilon_{low_frequent,lef} \right]^T \right)^{-1} \quad (3.17)$$

Figure 46 shows the block diagram of the process. The upper part of the figure shows the calibration process and the lower part the estimation process.

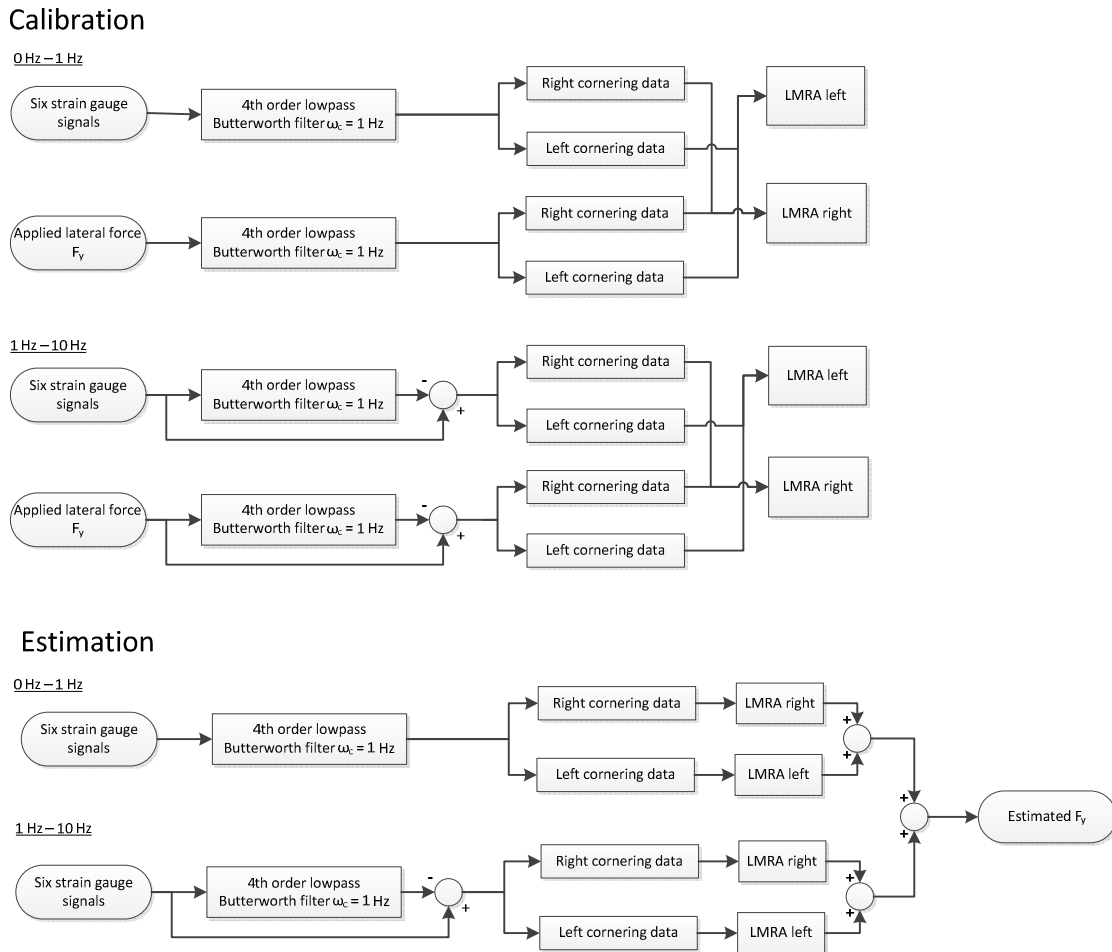


Figure 46 Block diagram

3.3.2 Result

Table 14 gives an overview of the obtained estimation errors using four estimation sections. The total error shows a slight increase when compared to the case where two sections are used (left/right separation). However, looking at static and dynamic parts separately, an accurate estimation is observed for the static part with an error of 4.31% where the dynamic part shows an error of 87.08%.

Table 14 Result lateral force estimation using four different section

Estimation by separate calibration for left, right, semi-static and dynamic					
	RMS error [N]	Mean μ [N]	Standard deviation σ [N]	RMS Applied F_y [N]	Percent error [%]
Total	81,48	-12,07	80,59	1222,50	6,67
Total, semi-static	52,62	-12,56	51,10	1221,00	4,31
Total, dynamic	62,35	0,49	62,35	71,61	87,08
Semi-static, left	33,30	-21,78	25,19	621,24	5,36
Semi-static, right	58,74	-8,83	58,08	1392,80	4,22
Dynamic, left	26,84	-0,20	26,84	26,89	99,83
Dynamic, right	71,94	0,77	71,93	71,61	100,46

3.4 Changing the order of the MLRA

This section will investigate the order of the MLRA to be used. First to fourth order estimations are performed. Table 15 shows the correlation coefficients between F_y and ε , ε^2 , ε^3 and ε^4 . Significant correlation coefficients are found for the first four orders of strain. Increasing the order to the third and higher results in a decrease. Table 16 shows the results of including the different orders. After the second order no significant better result is obtained and it can be stated that using a second order is best option for the force estimation.

Table 15 Correlation between F_y and strain/higher order of the strain

Correlation coefficient between F_y and strain and higher order of strain (ε , ε^2 , ε^3 , ε^4)				
Strain gauge	1st order strain: ε	2nd order strain: ε^2	3th order strain: ε^3	4th order strain: ε^4
1	-0,82	-0,88	-0,86	-0,82
2	-0,92	-0,91	-0,86	-0,82
3	-0,80	-0,86	-0,84	-0,81
4	-0,91	-0,91	-0,87	-0,83
5	-0,86	-0,87	-0,82	-0,77
6	-0,64	-0,79	-0,83	-0,82

Table 16 Results of the lateral force estimation using first to fourth order estimations

Estimation by separate calibration for left, right, semi-static and dynamic					
	RMS error [N]	Mean μ [N]	Standard deviation σ [N]	Percent error [%] Applied $F_y = 1222.5$ N	RMS
1st order	95,58	-2,44	95,55	7,82	
2nd order	81,48	-12,07	80,59	6,67	
3th order	79,08	-0,13	79,08	6,47	
4th order	81,75	1,86	81,73	6,69	

3.5 Reduction of the used strain gauges. Removal of poorly correlated strain gauges

As is seen in section 3.2 where the left/right separation is discussed several strain gauges show bad correlation between F_y and ε for positive lateral force. In this section an estimation will be performed using only the good correlated strain gauges. Table 9 shows that only strain gauge 1 and 6 show a good correlation ($R_{xy} > 0.8$) for positive F_y . Strain gauge 2 to 5 will be disregarded for the MLRA for positive F_y .

3.5.1 Result

Because only the MLRA for the positive F_y is changed, only the outcome of this estimation will be discussed. In section 3.3 it is seen that for positive F_y a RMS-error is obtained of 33.3 N for the low frequent bandwidth and a RMS-error of 26.84 N for the dynamic bandwidth. By disregarding strain gauge 2 to 5 the RMS-errors turn out to be 36.27 N and 26.88 N. No significant improvement has been obtained and there is thus no necessity of disregarding strain gauges which show a lower correlation coefficient from the LMRA.

3.6 Conclusion

In this section a MLRA has been set up and refined. First the separation into a MLRA for both positive and negative lateral force increased the accuracy of the estimation from 8.85% to 5.58%. It has to be noticed that, despite the absolute value problem of the strain gauges, the separation between positive and negative F_y had been made possible by looking at the load profile which had been applied to LSB. When implemented in an actual vehicle this is not possible and an extra sensor is needed for the determination of the direction. In the next chapter this extra sensor, the Eddy-current sensor, will be introduced.

The second separation into two frequency bands did not increase the overall accuracy (6.67%) of the lateral force estimation but did show accurate results for the low frequent content (4.31%). Also, this separation does lead to the possibility to substitute the low frequent force estimation by a more appropriate way to overcome the problem of the temperature induces strain and the 'absolute value problem. The dynamic response turned out to be badly correlated with the lateral force and the performed estimation in the dynamic range showed errors up to 100%. However, the dynamic force estimation is included in the algorithm.

In the end, F_y is estimated using four MLRAs. Two (one for the semi-static force and one for the dynamic force) estimating the positive F_y and two estimating the negative F_y .

The influence of the order of the MLRA has been investigated and it is seen that a second order is best suitable.

By taking out the strain gauges which show the lowest the correlation with the applied F_y , no improvement in the accuracy of the estimation is gained.

4 Sensor fusion; addition of Eddy-current sensors

This chapter introduces the measurement of an extra degree of freedom; the tilting movement of the ABS-ring. The ABS-ring is integrated in the seal of the bearing and is mounted to the inner ring of the bearing, see Figure 47. The tilting movement of the ABS-ring provides information about the changed position and orientation of the inner ring with respect to the outer ring. It will turn out that measuring the tilt of the ABS-ring/inner bearing ring can provide an accurate estimate of the lateral force acting on the tire contact patch. This will be further explained in section 4.1 and 4.2.

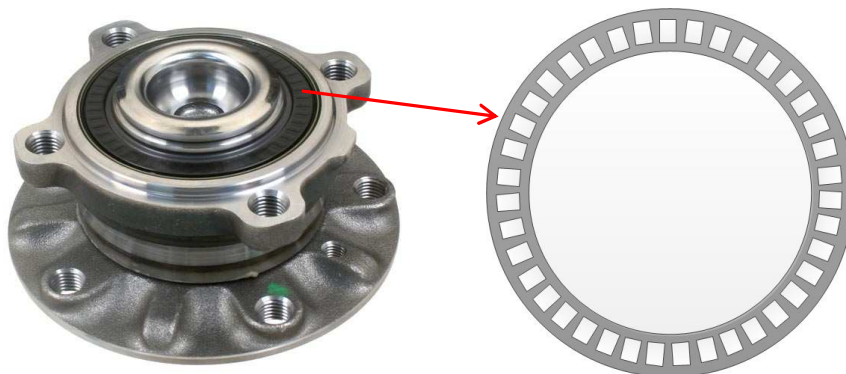


Figure 47 Integrated steel ABS-disc in the rubber bearing sealing

Measuring the tilting movement of the ABS-ring is mainly motivated to overcome two problems of which the first has already been discussed in section 2.9.1.1 and is known as the absolute value problem.

To recapitulate, the absolute value problem causes that left and right cornering forces cannot be distinguished by the strain. Both positive and negative F_y show positive strain values resulting in the piecewise continuous V-shaped $F_y - \varepsilon$ graphs from section 2.9.

The second problem to overcome is that the strain gauges are subject to drift due to thermal gradients within the outer ring of the LSB which result from heat generated in the bearing by friction of the rolling balls with the inner- and outer ring of the bearing and due to heat from the outside generated by the brake disc and –caliper. This heat deforms the bearing and induces, next to the force induced strain, unwanted temperature induced strain in the strain gauges, which cannot be distinguished from the mechanically introduced strain. This temperature drift is of a low frequent nature (large time constant). It is shown that the largest eigenvalues lie between $-3.7 \cdot 10^{-3}$ Hz and $-5.7 \cdot 10^{-3}$ Hz. The temperature dynamics are therefore dominated by a set of time constants between 175 s and 270 s (Bot, 2009).

The low frequent content of the measured strains, giving the necessary information about the semi-static loads acting on the wheel, is therefore not reliable and should therefore be omitted from the force estimation.

Next to the six strain gauges measuring the deformation of the LSB, two Eddy-current sensors are installed in the knuckle to measure the tilting movement of the ABS-ring as shown in Figure 48 and as explained in section 4.2.

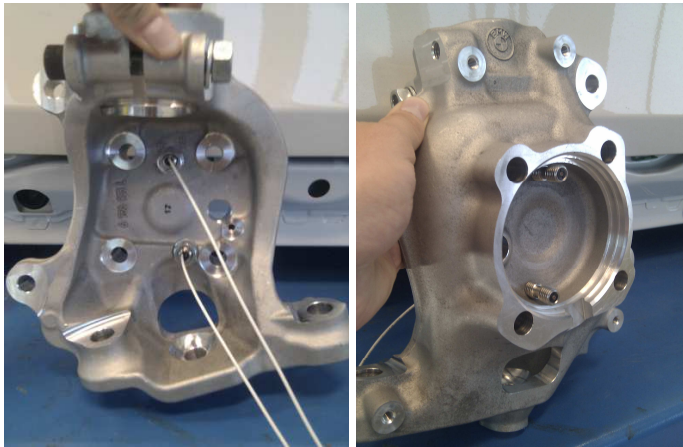


Figure 48 Eddy-current sensors installed in the knuckle



Figure 49 Eddy-current sensor

The Eddy-current sensors will provide the information about the low frequent semi-static lateral force and the strain gauges will provide the information for the estimation of the higher frequent dynamic lateral force.

The working principle of the Eddy-current sensor is discussed in section 4.1, whereas the extraction of usable information, to estimate the low frequent lateral force from the sensors, is discussed in section 4.2. Section 4.3 shows the relations between the lateral force F_y and the Eddy-current signals. Finally in section 4.4 lateral force estimations are carried out. These force estimation are first based on only the Eddy-current sensors and are later complemented by the strain gauges. The force estimations are based on measurements performed at BETSY. Force estimations including the performed field measurements at the test track of SKF are saved for Chapter 5.

4.1 Eddy-current sensors

Eddy-Current sensors are noncontact devices capable of measuring displacement of a target based on a change in electromagnetic induction.

The sensor creates an alternating current in the sensing coil in the end of the probe. This creates an alternating magnetic field which induces small circling currents in the target material; these currents are called Eddy-currents. The Eddy-currents create an opposing magnetic field which resists the field being generated by the probe coil by mutual inductance. The interaction of the magnetic fields is dependent on the distance between the probe and the target. As the distance changes, the electronics sense the change in the field interaction and produce a voltage output which is proportional to the change in distance between the probe and target.

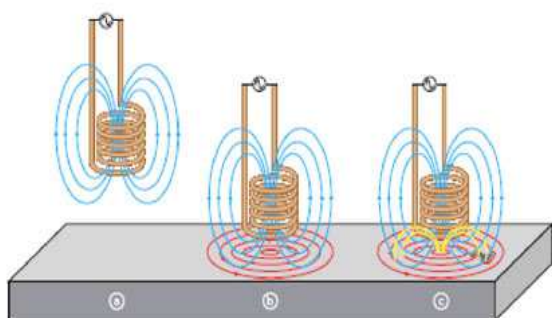


Figure 50

a: The alternating current flowing through the coil at a chosen frequency generates a magnetic field around and through the coil.

b: When the coil is placed close to an electrically conductive material, eddy-currents are induced in the material.

c: The induced magnetic field by the Eddy currents interact with the magnetic field of the probe changing the impedance of the sensor coil.

Nonconductive materials intervening between the sensor and target have little or no effect on system output. Because of this, environmental contaminants, such as oil, dirt, and humidity have virtually no effect on system performance and makes them very suitable for an automotive application.

The Eddy-currents sensors are produced by the company Kaman Sensors and can be found under the name Kaman Precision Products KD-2300 The sensor itself is shown in Figure 49.

A sensor signal conditioning electronics box, shown in Figure 51, is connected to the sensors. It is powered by three connection terminals; -15 V, 0 V and +15 V. Figure 51 shows four conditioner boxes. The conditioner box contains a balanced bridge network of which the sensor makes up one leg. The box also contains an electronic oscillator/demodulator to produce the alternating current. In Figure 48 the placement of the Eddy-currents sensor in the knuckle is shown.



Figure 51 Eddy-current signal conditioning electronics

4.2 Eddy-current sensor conditioning

4.2.1 BETSY

Figure 48 and Figure 49 show the two Eddy-current distance sensors installed in the knuckles. They point into the direction of the bearing with ABS-ring to measure the deflection of the top and bottom of the ring. The ABS-ring is a steel ring with 48 holes in the axial direction. When the bearing rotates the Eddy-current sensors ‘see’ during every rotation of the wheel 48 holes and 48 spokes passing by.

When a hole is passing by the sensor signal will rise to its maximum value and as soon as a spoke is ‘seen’, the sensor lowers its signal to a value proportional to the distance

between the Eddy-current sensor and the ABS-ring. A signal consisting of peaks is thus created. See Figure 52 for 10 of these peaks.

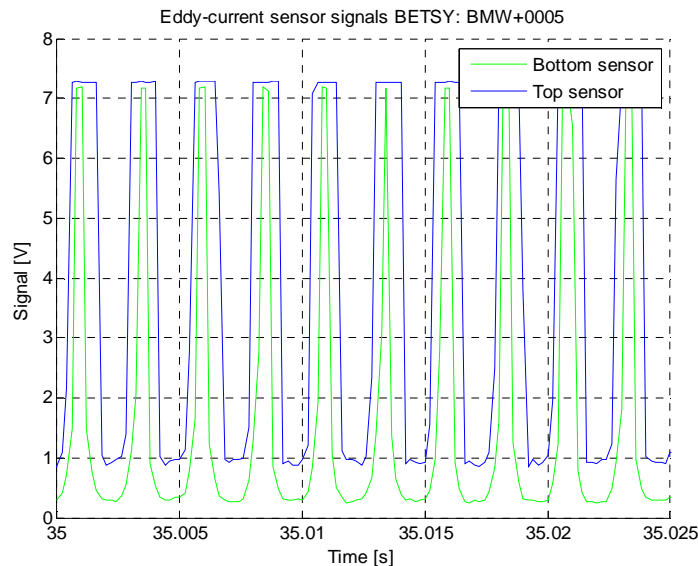


Figure 52 Eddy-current sensor signals. Test BMW+0005.

Since the ABS-ring is mounted to the inner ring of the bearing, the lower values of the sensor signal provide information about the changed position and orientation of the inner ring with respect to the outer ring. 1 mV of signal corresponds to 1 micron distance between the sensor and the ABS-ring. The sensitivities of the Eddy-current sensors are therefore 1 mV/ μm .

In section 4.3 this tilting is shown to be a direct measure of the lateral force acting on the wheel.

The conditioning process of the Eddy-current signals will therefore consist of the extraction of these lower values from the whole signal.

The algorithm to extract the lower values is explained as follows.

To extract the lower values of the signals, an algorithm is written. The algorithm takes the raw Eddy-current sensor signal as its input. The output of the algorithm will be the set of all the low values. The algorithm compares the input signal, sample by sample with certain conditions. When a flat plateau is detected the output will be equal to the input. When a rising edge of a peak is encountered the output will hold its value of the last valley until a new value is detected. A valley is detected as soon as two conditions are met:

The first condition is the derivative of the signal. When the derivative is between certain bounds y_{low} and y_{high} it means that the signal is not in- or decreasing and so the sensor is pointed straight into a hole or straight at the ring. The lower bound of the derivative is set on $y_{low} = -0.06$. The higher bound is set on $y_{high} = 0.06$. When the derivative of the signal falls outside this domain the signal is either increasing to its maximum value or decreasing to its minimum value. In theory, the lower bound could be set to be 0, but due to small signal variations during the flat plateaus, the lower bound is set on y_{low} . This will greatly improve the robustness of the algorithm.

This first condition on the domain of the derivative is met at two events; During the lower plateaus, but also at the top of the peaks, because there, the signal is also constant. To forbid the output to take over these higher values, a second condition is set: the maximum change in output per sample, Δy_{max} . In this way the output will hold the last value sensed during a valley and is updated only when a new valley is detected.

An initial value y_0 is also required. y_0 is equal to the sensed value when the bearing is unloaded. This is necessary to prevent the output to follow the peak values. This would be the case when the signal starts at a peak. In Figure 53 the flowchart of the algorithm is shown.

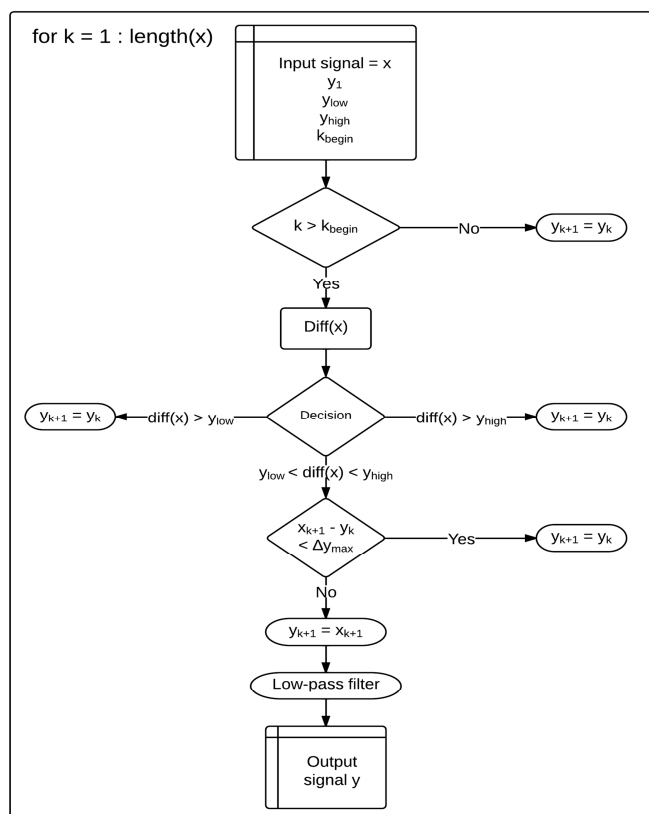


Figure 53 Flow chart low of the value algorithm

After the algorithm, the output signal is a stepwise function jumping from one value to the other; see the red lines in the upper graphs of Figure 54. Both the left- and right side of Figure 54 show the same signal. However, the left side shows the signal on a shorter timespan to visualize time signal peaks.

The output of the algorithm is low pass filtered to transform it into a smooth function which coincides with the lower values of the sensor signal; see the green lines in the lower graphs of Figure 54.

The extracted low values give a measure of the distance between the sensor and the ABS-ring. During installation the sensors are mounted in the knuckle at a finite distance from the ring. This finite distance will be subtracted from the signal in order to get the deflection from its 'equilibrium' position.

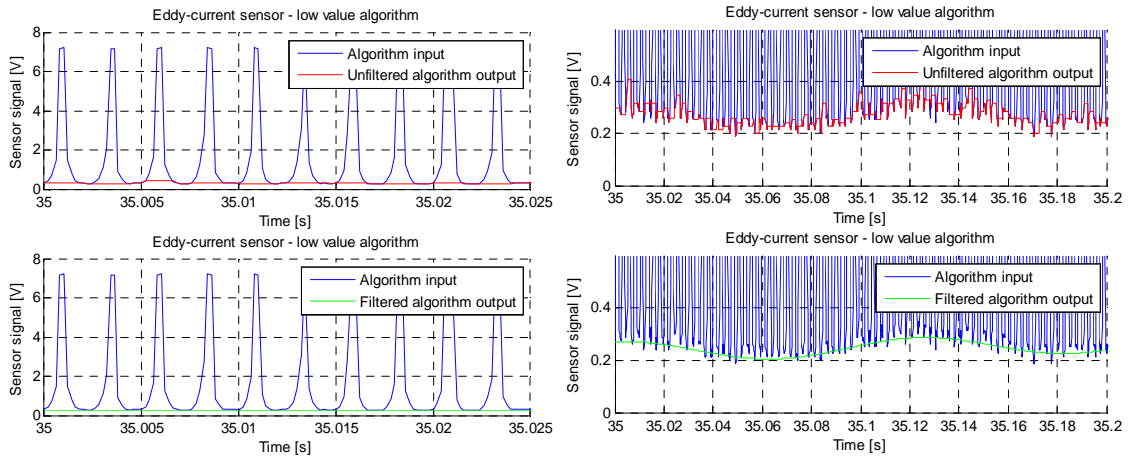


Figure 54 Upper figures: The low values of Eddy-current sensor signal before the low pass filter. Lower figures: The low values of Eddy-current sensor signal after the low pass filter

The flowchart in Figure 53 shows that at time instant k the derivative of the upcoming interval between k and $k+1$ is checked. If this derivative falls outside the domain $\{y_{low} .. y_{high}\}$ then the output at $k+1$ is equal to the output at time instant k . When the derivative condition is met it is checked if the difference of the input signal at $k+1$ and the output at k is smaller than Δy_{max} . If this is true the output signal at $k+1$ will become equal to the input signal at $k+1$. If this condition is not true it means that we are located at the constant signal at the top of a peak and then the output at $k+1$ is again equal to the output at time instant k .

During startup the rotational velocity increases from 0 rpm to 750 rpm. During this start up the rising- and decreasing slopes of the peaks are smaller than the slopes at full speed and the possibility exist that the algorithm will follow the upper values instead of the lower ones. Therefore, another parameter k_{begin} can be set. This parameter forces the output to be equal to $y(1)$ until the rotational speed is 500 rpm and will exclude the possibility of making errors in the low value extraction.

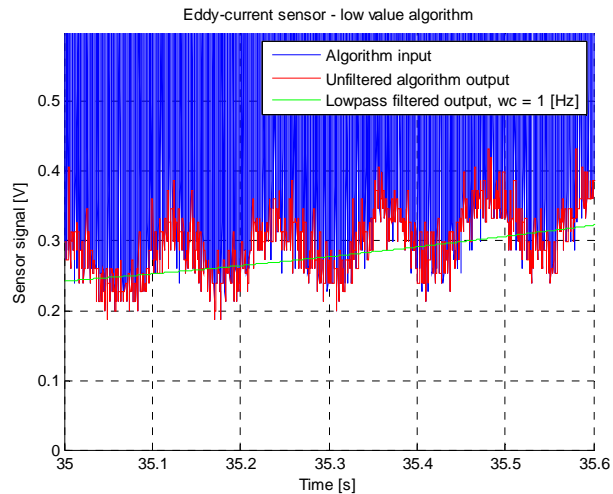


Figure 55 Filtering of the wobble on BETSY

Due to an inclination misalignment of the LSB on BETSY, a wobble, with a frequency equal to the frequency of rotation, can be observed in the measured signal. The BETSY measurements are performed at 500 rpm = 8.33 Hz. This equals a period of

$$T = \frac{1}{8.33 \text{ Hz}} = 0.12 \text{ s} \quad (4.1)$$

Figure 55 shows the wobble in the signal. Because this wobble is not of our interest and, as explained, the low frequent part is the part that is of interest, the wobble is filtered out by applying a low pass filter with a cutoff frequency of $\omega_c = 1\text{Hz}$, see the green line in Figure 55.

After these steps the signal is converted to the physical dimension. For the Eddy-current signals in this chapter the conversion is: $1\text{ V} = 200\ \mu\text{m}$. For the Eddy-current signals in the next chapter (measurements with the BMW test vehicle) the conversion is different: $1\text{ V} = 1000\ \mu\text{m}$.

4.3 Lateral force estimation using the Eddy-current sensors.

In this section the relation between the applied lateral force and the Eddy-current sensor signals will be analyzed. Both the signals from the upper- and lower sensor and the difference between the two sensors are plotted versus F_y . The found relations will be approximated by n-th order polynomials.

4.3.1 Influence of the lateral force on the tilt

The BETSY run consisting of the experiments BMW+0005 – BMW+0008 are used in the analysis. In Figure 56 the measured deflection from the equilibrium position is plotted versus F_y . The left graph shows the bottom sensor and the right graph the top sensor.

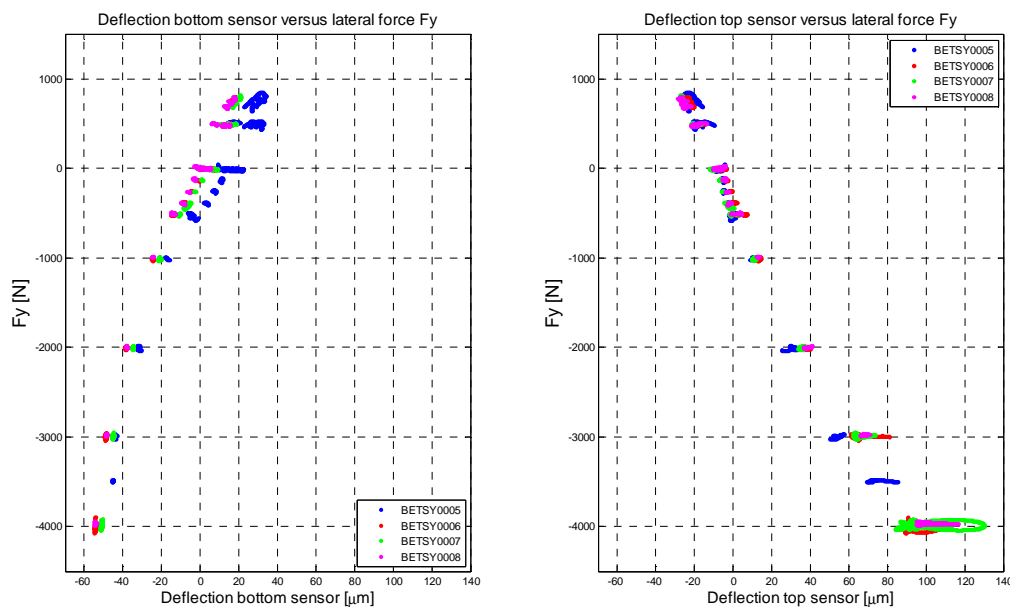


Figure 56 Lateral force versus the measured deflection. Left plot: top sensor. Right plot: bottom sensor

Sidenote: For BMW+0005 the top- and bottom sensor were mounted at 680- and 410 micron from the disc respectively, whereas the three other tests showed an equilibrium at 780 and 360 micron respectively.

A trend can be observed for both the top- and bottom sensor. The data from the test BMW+0005 shows an offset compared to the other tests. The trend for the bottom sensor shows a non-linearity in the trend whereas the top sensor's trend is more linear.

The signals can be combined by subtracting the top deflection x_{top} from the bottom deflection x_{bottom} . The difference will from now on be denoted with 'tilt', x_{tilt} . Figure 57 shows the trend between the tilt and the lateral force F_y .

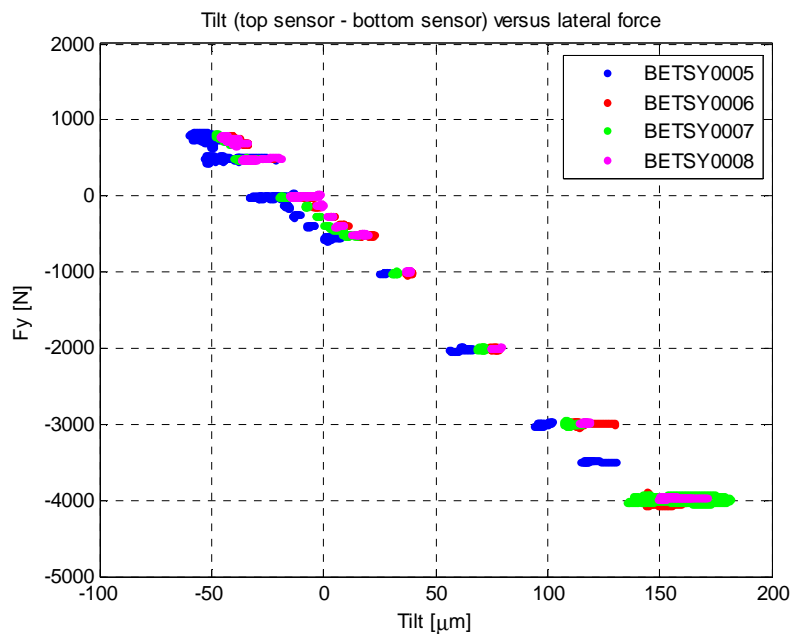


Figure 57 Tilt vs. the lateral force F_y

The observed trends can be approximated by n-th order polynomials as shown in Figure 58. From the upper left graph to the lower right graph the data is fitted with an first to sixth order polynomial. In the title the RMS error of the fit is shown. Not unexpectedly, the error decreases with increasing polynomial order. For the fourth- and sixth order an extrapolation of the curve outside the measured range of tilt will result in unrepresentative approximated force. The reduction in error for a fit with an order higher than two is not significant.

Tilt versus lateral force approximated by nth order polynomials

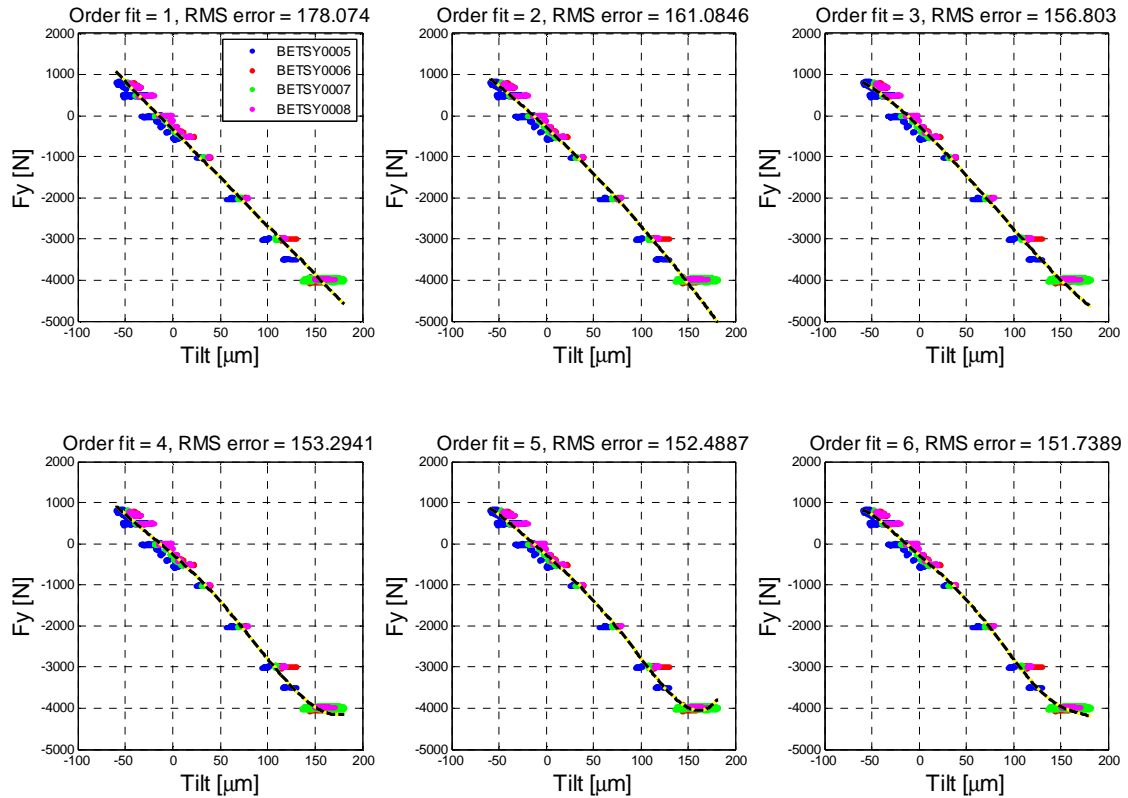


Figure 58 Tilt versus lateral force approximated by n-th order polynomials

Also the trends for the top- and bottom sensor alone can be approximated by a n-th order polynomial. In Table 17 the RMS-errors are shown for a first to sixth order fit. Same as for the tilt, increasing the order of the fit does not significantly reduce the error for orders higher than two. In Appendix E the figures are shown where the fit lines are shown through the data for the bottom- and top deflection in the same way as in Figure 58.

Table 17 Polynomial fit errors

Order	Fit errors		
	Tilt [N]	Bottom [N]	Top [N]
1	178,07	392,45	148,04
2	161,08	239,91	113,44
3	156,80	230,69	104,53
4	153,29	228,83	104,51
5	152,49	225,23	102,33
6	151,74	224,16	102,17

Based on the extrapolation characteristics and the observed errors, a second order fit will be used for the force estimation. By looking at Table 17 it seems desirable to omit the bottom sensor from the estimation and only use the top sensor because of the smaller

spread in the data. Both using the tilt and only the top sensor for the estimation will be discussed in section 4.3.

For a second order fit the equation will be: $F_y = c_1 \cdot x_{tilt}^2 + c_2 \cdot x_{tilt} + c_3$. The polynomial coefficients c_1 , c_2 , and c_3 for the top, bottom and tilt are shown in Table 18

Table 18 Fit coefficients for the top- and bottom sensor and the tilt

	c_1	c_2	c_3
Tilt	-60,84	-1032,98	-306,16
Top	-266,76	836,82	-100,24
Bottom	72,96	-1283,15	-439,96

4.3.2 Reproducibility

This paragraph will go into the reproducibility of the tilt measurement. Figure 59 shows for a second test run (different LSB than the one used in section 4.3.1) the trend between the measured tilt and the lateral force. The black line represents the second order polynomial fit of the test run. In cyan line is the second order fit from the test run used in section 4.3.1.

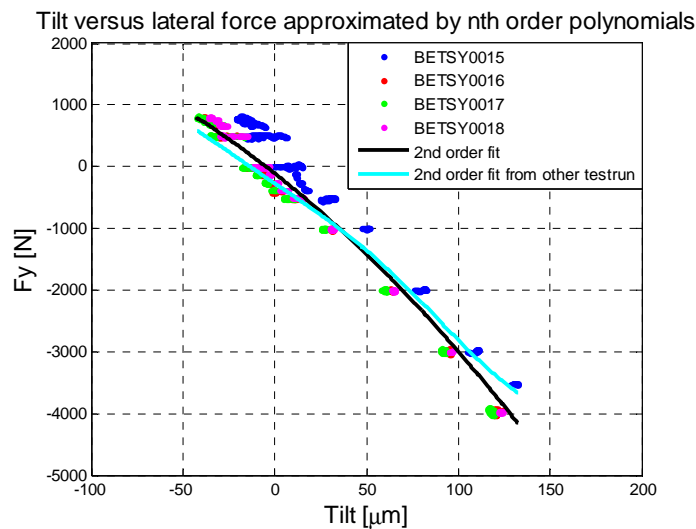


Figure 59 Reproducibility of the tilt measurement

A difference can be observed between the two testruns. The second order fits can be described by:

$$\begin{aligned} F_{y,testrun1} &= -60.84 \cdot x_{tilt}^2 - 1032.98 \cdot x_{tilt} - 306.16 \\ F_{y,testrun2} &= -87.81 \cdot x_{tilt}^2 - 982.65 \cdot x_{tilt} - 279.77 \end{aligned} \quad (4.2)$$

When inserting a range of test values into the two equations for the tilt; $-40 \mu\text{m} < x_{tilt} < 130 \mu\text{m}$, a measure can be given for the reproducibility.

The difference between the two estimations for these test values have a RMS value of 123.87 N.

When using BETSY for calibration of a complete production line of LSBs this reproducibility error is unavoidable. Next to this error another reproducibility error will originate from the reproducibility of the tilt - F_y trend measured in the real vehicle. In Chapter 5 measurements will be performed using one single bearing on BETSY and in the field. For both cases the tilt - F_y trend will be determined and used for force estimation. The reproducibility error just obtained will then not influence the force estimation.

4.4 Force estimation using the Eddy-current sensor signals

In this section the obtained extra sensor signals will be used to estimate the lateral force applied to the bearing. As explained in the introduction of this chapter the Eddy-current sensors will primarily be used to determine the low frequent (0 Hz – 1 Hz) content of the force, because this low frequent content in the strain signals is subject to unwanted thermal induced strain in the strain gauges. Next to this low frequent force estimation also an estimation will be performed for frequencies from 1 Hz to 10 Hz.

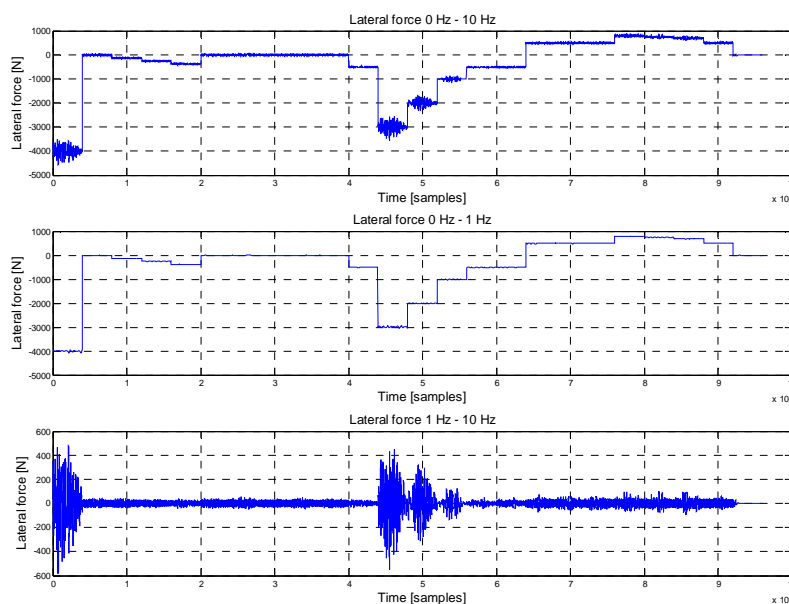


Figure 60 Frequency separation of the BETSY signals

In section 4.4.1 the results are shown for the lateral force estimation for different frequency bandwidths. First using only the top sensor, second only the bottom sensor and at last using the tilt.

The BETSY signals will again be divided as shown in Figure 60. The top graph shows the whole signal up to 1 Hz. The middle one shows the content from 0 Hz to 1 Hz and the lower graph shows the content from 1 Hz to 10 Hz

Seven BETSY experiments will be used for the calibration and one experiment will be used to validate. Tests BMW+0005, BMW+0007, BMW+0008 and BMW+0015 to BMW+0018 are used for calibration and the test BMW+0006 is used for validation.

Of course, for the estimation in one of the frequency bands, the calibration will be performed on the respective frequency bands in the calibration signals.

4.4.1 Force estimation using the tilt

Figure 61, Figure 62 and Figure 63 show the applied and estimated force using the tilt, only the top sensor and only the bottom sensor respectively.

The top graph shows the applied- and estimated force versus time. The lower left shows the applied force versus the estimated force where in blue the ideal line is shown. In the lower right graph the error distribution is shown.

Lateral force estimation based on the tilt measurement, 0 Hz - 1 Hz

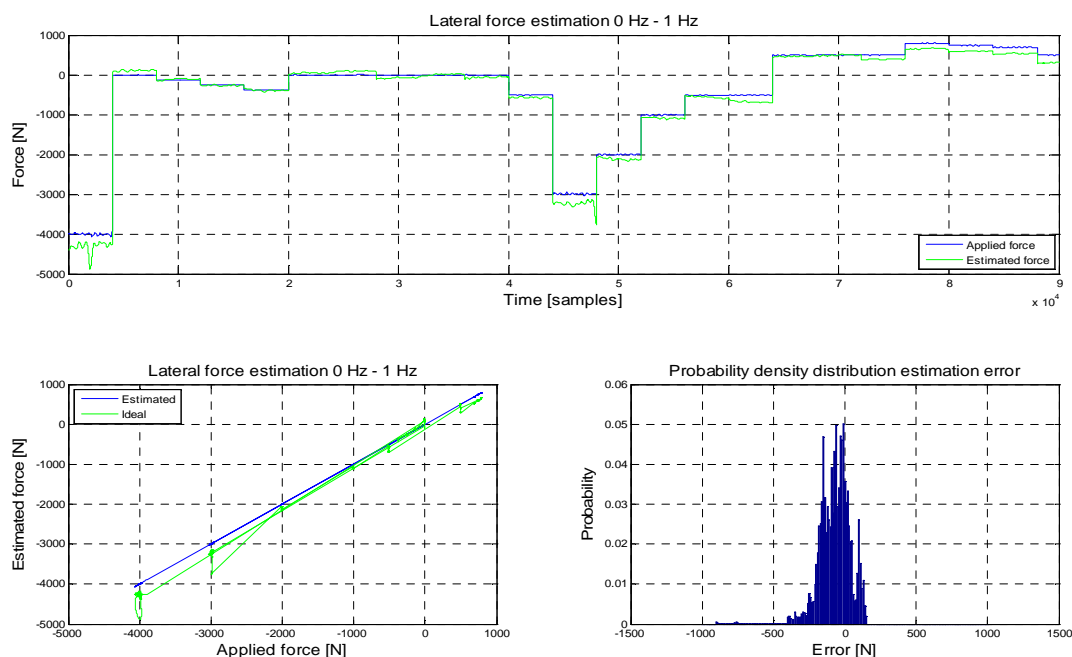


Figure 61 Low frequent force estimation using the tilt

The error is normally distributed and can therefore be described by a mean value μ and a variance σ . In Table 19 the RMS, mean and variance of the error are shown. Also shown in this table are the RMS, mean and variance of the applied F_y . These values are shown to relate the error to the applied force. Also shown is the percent error which is described by:

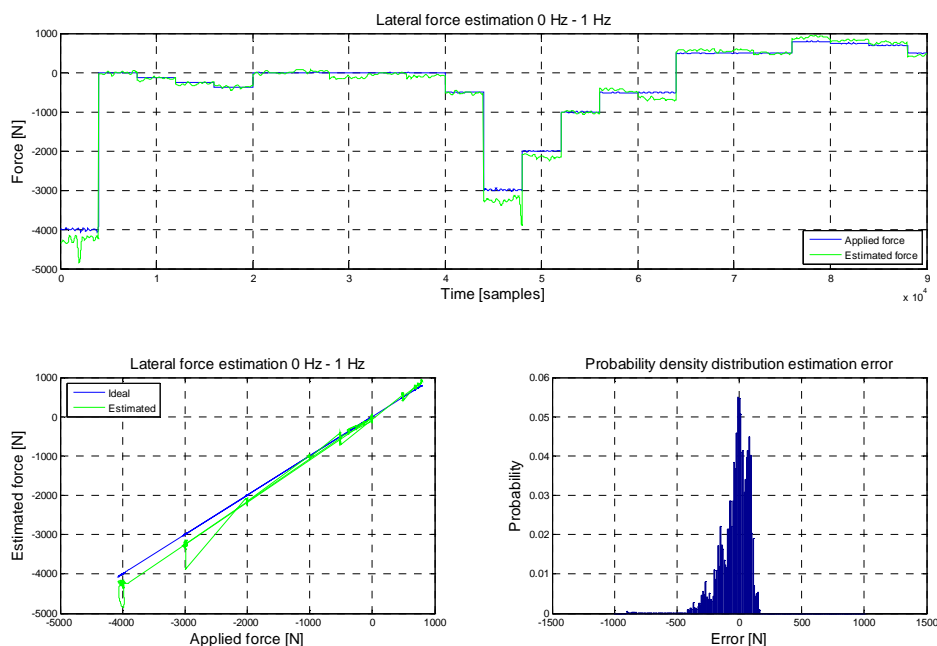
$$\text{Error [\%]} = \frac{\text{RMS}_{\text{Error}}}{\text{RMS}_{F_y}} \quad (4.3)$$

Table 19 RMS, mean and variance of the estimation error using the tilt

	0 [Hz] - 1 [Hz]			Percent error [%]
	RMS	Mean μ	Standard deviation σ	
F_y	1221,00	-339,45	1134,60	
F_y estimation error by tilt	131,83	-70,01	111,70	10,80

In Figure 62 the estimation is performed only using the top sensor. The error details are shown in Table 20. Compared to the previous case there is a slight decrease in RMS error. Contrarily there is a slight increase in the variance.

Lateral force estimation based on the top sensor measurement, 0 Hz - 1 Hz

**Figure 62 Low frequent force estimation using the top sensor****Table 20 RMS, mean and variance of the estimation error using the top sensor**

	0 [Hz] - 1 [Hz]			Percent error [%]
	RMS	Mean μ	Standard deviation σ	
F_y estimation error by the bottom sensor	122,30	-32,80	117,82	10,02

In Figure 63 the estimation is performed only using the bottom sensor. Estimation using the bottom sensor gives the worst result relative to the case where the top sensor and tilt are used. This is shown in Table 21.

Lateral force estimation based on the bottom sensor measurement, 0 Hz - 1 Hz

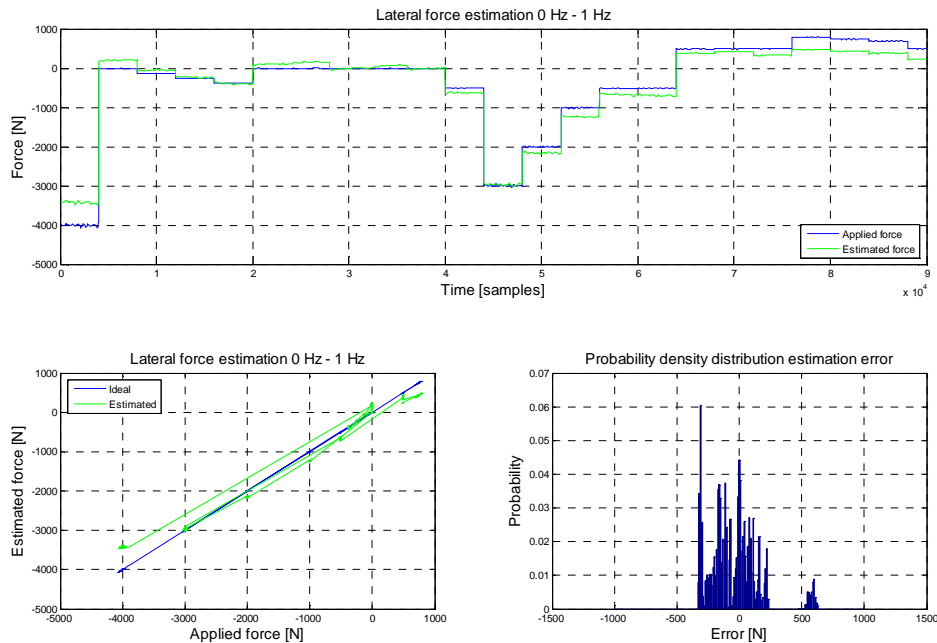


Figure 63 Low frequent force estimation using the bottom sensor

Table 21 RMS, mean and variance of the estimation error using the bottom sensor

	0 [Hz] - 1 [Hz]			Percent error [%]
	RMS	Mean	Standard deviation σ	
F_y estimation error by the top sensor	205,42	-44,61	200,52	16,82

Like the above three estimations, estimations are performed on the frequency band 1 Hz – 10 Hz and on the full frequency range of 0 Hz to 10 Hz. The figures are shown in Appendix F. An overview of the obtained errors is given in Table 22 to Table 24. The estimations including the signal content from 1 Hz to 10 Hz show significant errors. The percent errors are taken again relative to RMS values of F_y .

Table 22 Low frequent estimation errors

	0 [Hz] - 1 [Hz]			Percent error [%]
	RMS [N]	Mean [N]	Standard deviation [N]	
F_y	1221,00	-339,45	1134,60	
F_y estimation error by top sensor	122,30	-32,80	117,82	10,02
F_y estimation error by bottom sensor	205,42	-44,61	200,52	16,82
F_y estimation error by tilt	131,83	-70,01	111,70	10,80

Table 23 High frequent estimation errors

	1 [Hz] - 10 [Hz]			Percent error [%]
	RMS [N]	Mean [N]	Standard deviation [N]	
F_y	62,09	0,01	60,23	
F_y estimation error by top sensor	62,41	3,36	62,32	100,52
F_y estimation error by bottom sensor	61,24	-0,15	61,24	98,63
F_y estimation error by tilt	61,54	0,11	61,54	99,11

Table 24 Full frequency range estimation errors

	0 [Hz] - 10 [Hz]			Percent error [%]
	RMS [N]	Mean [N]	Standard deviation [N]	
F_y	1222,50	-339,44	1136,10	
F_y estimation error by top sensor	481,35	-36,64	479,95	39,37
F_y estimation error by bottom sensor	284,96	-45,58	281,29	23,31
F_y estimation error by tilt	366,38	-71,60	359,32	29,97

In order to explain why the bottom sensor is not as good as the top one and why the high frequent content gives large errors in comparison to the low frequent content, the correlation coefficients will be considered. In Table 25 to Table 27 the correlation coefficients are given. The significantly correlated ones are highlighted in green and the uncorrelated ones are highlighted in red. The top sensor and the tilt show the highest correlation coefficient for the low frequent content. The bottom sensor shows correlation but not significant. For the high frequent content there is no correlation at all. As a result the estimation error in the dynamic range shows values up to 100%.

Table 25 Correlation coefficients R_{xy} for the low frequent content

R_{xy} . 0 Hz < f < 1 Hz	F_y
Top sensor	-0,82
Bottom sensor	0,42
Tilt	-0,85

Table 26 Correlation coefficients R_{xy} for the high frequent content

R_{xy} . 1 Hz < f < 10 Hz	F_y
Top sensor	-0,13
Bottom sensor	0,11
Tilt	-0,15

Table 27 Correlation coefficients R_{xy} for the full frequency content

R_{xy} . 0 Hz < f < 10 Hz	F_y
Top sensor	-0,76
Bottom sensor	0,41
Tilt	-0,82

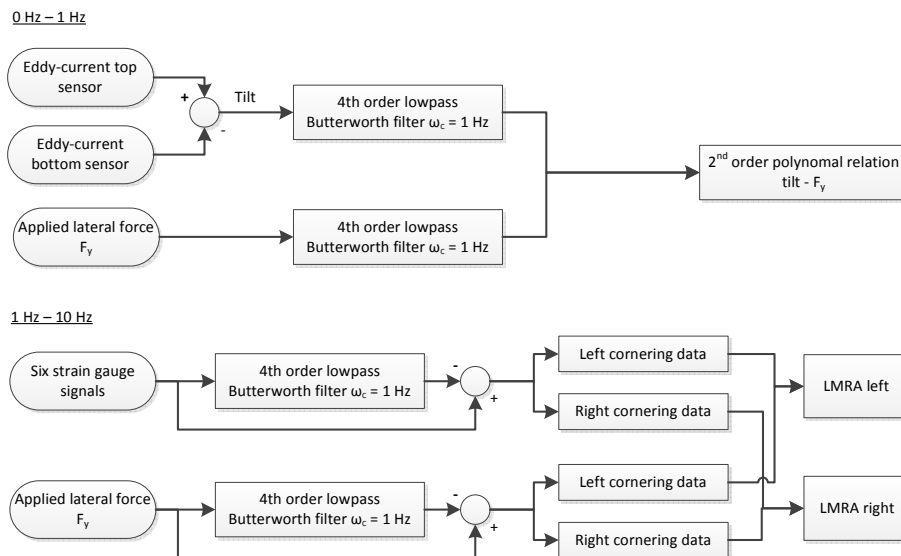
4.4.2 Lateral force estimation using the tilting movement of the ABS-ring and the deformation of the LSB outer ring

In this section the low frequent force estimation using the tilting movement of the ABS-ring from section 4.3 and the high frequent force estimation using the measured deformation of the bearing outer ring (MLRA) from Chapter 3 are combined to validate the full algorithm. The validation is performed on BETSY-test BMW+0006. This test is not used for calibration and is therefore an appropriate test candidate for validation.

In Figure 64 the block diagram is shown. The upper part represents the calibration and the lower part the estimation. Both parts are divided in a low- and high frequent part.

4.4.2.1 Block diagram

Calibration



Estimation

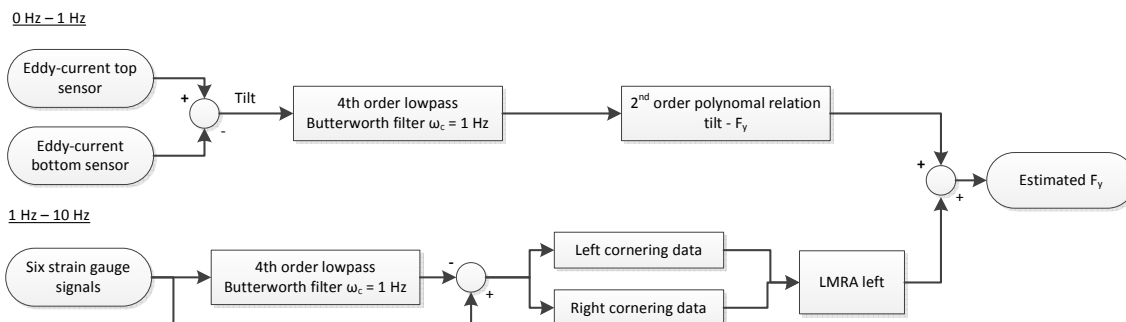


Figure 64 Block diagram of the full algorithm

4.4.2.2 Result

The applied and estimated lateral force are plotted in Figure 65 versus time. The applied force is plotted versus the estimated force in Figure 66. In Figure 66 the deviation of the green line from the ideal blue line indicates the accuracy of the estimation. The forces in the range of -2000 N to 1000 N are better approximated than force outside that range.

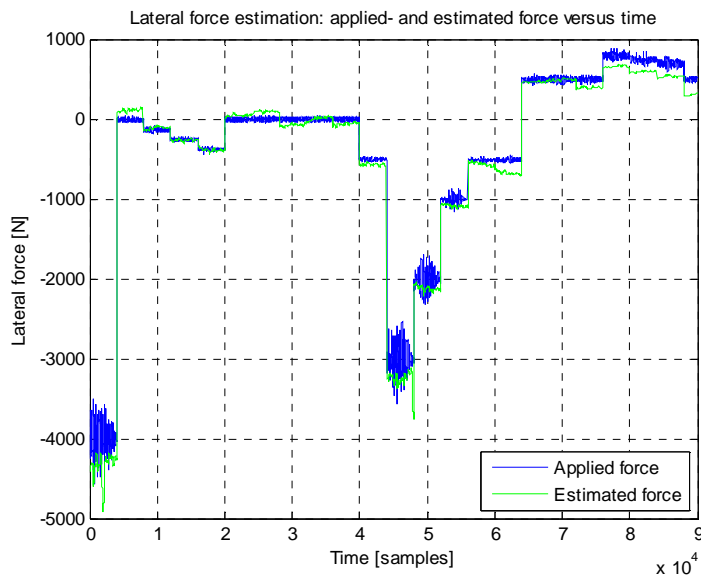


Figure 65 Applied and estimated lateral force versus time

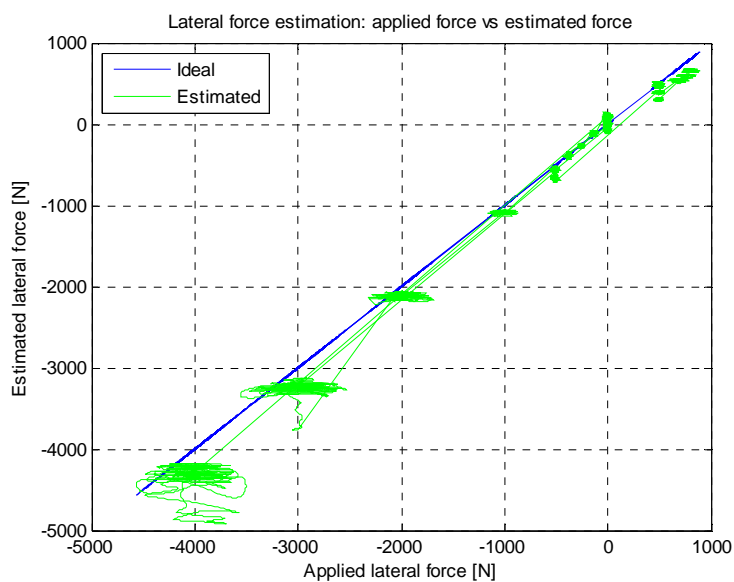


Figure 66 Applied force versus the estimated force

In Figure 67 the error distribution of the estimation is shown. Again the error can be approximated by a Gaussian distribution.

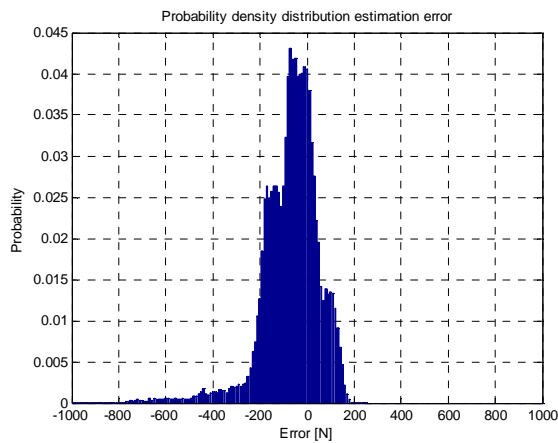


Figure 67 Error distribution

The root mean squared error is equal to 147.47 N. The mean μ is -70.50 N and the standard deviation σ is 129.53 N. The RMSE introduced by the low frequent part is 131.83 N and the RMSE introduced by the high frequent part is 62.35 N, see Table 28.

Table 28 Estimation errors

	RMS error	Mean μ	Standard deviation σ	RMS F_y	Percent error [%]
F_y estimation 0 Hz - 1 Hz	131,82	-70,02	111,7	1221,00	10,80
F_y estimation 1 Hz - 10 Hz	62,35	-0,49	62,35	62,09	100,42
Total	147,47	-70,50	129,53	1222,50	12,06

Whereas the low frequent part of the lateral force is estimated with an error of 10 %, the lateral in the dynamic range shows an error of 100%.

5 Field / validation measurements

The front wheels of the BMW E60 530i from the automotive department of the faculty 3ME, TU Delft are provided with the load sensing equipment. The equipment consists of the LSB with the six strain gauges and a knuckle accommodated with two Eddy-current sensors. Tests are first performed on the BETSY and secondly on the test track of SKF.

In section 5.1 the measurement set-up is discussed. Where section 5.2 discusses the strain and force measurements performed on BETSY, section 5.3 will discuss the strain and force measurements performed in the field. Then, in section 5.4, the strain measurements on BETSY and in the field will be compared. In section 5.5 and 5.6 the tilt measurements on BETSY and in the field will be discussed respectively. In section 5.7 the tilt measurements will be compared. Section 5.8 will discuss the reproducibility of the strain and tilt measurements. The lateral force will be estimated using an in situ- and BETSY calibration in section 5.9. For both the in-situ and the BETSY calibration the lateral force will be estimated in two ways.

The first method is only based on the measured deformation of the LSB as discussed in Chapter 3. This estimation is performed to show to what extent the developed method to use BETSY as calibration machine is applicable.

The second is the method from Chapter 4 where the low frequent part of the lateral force is estimated by the Eddy-current sensors, the tilt of the inner ring/ABS-ring of the LSB, and where the dynamic part is estimated by measured deformations using a MLRA on the strain gauges.

5.1 Field measurements set-up

The load sensing bearings and knuckles with Eddy-current sensors are installed in the vehicle at the Carlab of SKF Engineering and Research Centre in Nieuwegein. This section will show the set-up.

Load sensing bearing

The left of Figure 68 shows the actual LSB which is mounted in the vehicle. On the right the same LSB is shown in place in the vehicle.



Figure 68 Load sensing bearing. Left: Single LSB. Right: Mounted in the vehicle.

Conditioner box

Figure 69 shows a picture of the conditioner box of the strain gauges. Figure 70 shows the conditioner box installed in the vehicle. The left two pictures show the conditioner box of the left bearing and the right picture show the conditioner box of the right bearing. The left one is installed in front of the driver seat in such a way that it does not conflict with the driver seat or the feet/legs of the driver. The conditioner box is covered with a plate protecting it from potential danger. The right bearing conditioner box is placed where normally the glove box would be. As for the glove box, the conditioner box can be hinged in and out.



Figure 69 Conditioner box of the strain gauges



Figure 70 Conditioner box of the strain gauges installed in the vehicle

Knuckle + Eddy-current sensors

The Eddy-current sensors, the knuckle and the knuckle with Eddy-current sensors are shown in Figure 71. The lower sensor is not placed vertically below the upper sensor. Although that was originally the idea, it turned out to be necessary to reposition the sensor because otherwise the sensor would conflict with the strut.

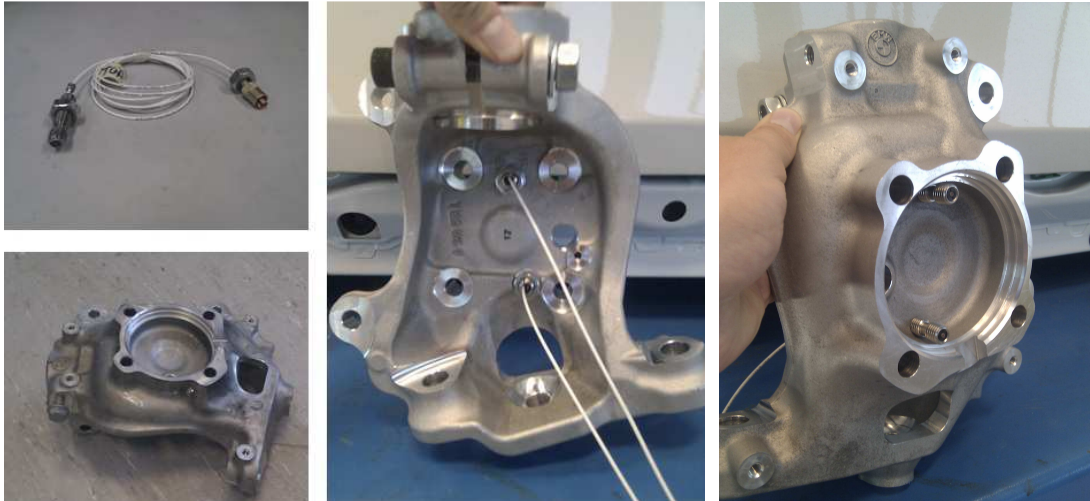


Figure 71 Eddy-current sensors and knuckle

Conditioner box

The conditioner box providing the power for the Eddy-current sensors is shown in Figure 72. All four sensors have their own box. The middle picture shows the placement of conditioners for the left side and the right picture the ones for the right side. The ones for the left front wheel are placed in the glove box on the left of the steering wheel. The ones for the right front wheel are placed behind the hinged conditioner box for the strain gauges.



Figure 72 Conditioner box Eddy-current sensor

DC/DC converter

All conditioner boxes are powered with a DC voltage. The strain gauges need a supply voltage of 0V and 15V and the Eddy-current sensors acquire a supply voltage of -15V, 0V and 15V. Therefore a DC/DC converter is installed in the vehicle. This converter converts the 12V from the vehicle battery to -15V, 0V and 15V. The converter is placed in a plastic housing containing an on/off switch and a LED as an on/off indicator. The power supply connection cables can be plugged in with banana plugs.



Figure 73 DC/DC-converter for the Eddy-current conditioner boxes

Kistler force measuring wheel: VELOS

The left front wheel is replaced by the VELOS wheel to provide the reference forces acting on the wheel. The left picture in Figure 74 is showing the VELOS wheel, the middle picture the conditioning- and power electronics and the right picture shows the VELOS wheel mounted to the vehicle.



Figure 74 Left: VELOS wheel. Middle: Conditioning and power electronics. Right: VELOS mounted to the vehicle.

New brake disc and –caliper

During the installation of the VELOS wheel it turned out to be necessary to replace the brake disc (and thereby the brake caliper). The rim of the VELOS wheel is more narrow than the original wheel. Therefore the brake disc did not fit into the rim of the VELOS wheel. The BMW was equipped with upgraded sport package brakes. These have now been replaced by the standard brake disc and –caliper.



Figure 75 New brake disc and - calliper

Cabling

The cables in the system to supply the conditioner boxes with a supply voltage and to transport the signals from the sensors/conditioner boxes to the data acquisition unit are placed in the vehicle. Both the sensors and conditioner boxes are placed in the front of the vehicle. The power supply and data acquisition unit are placed in the trunk. Cables are therefore placed from the front of the vehicle to the trunk and are located in the vehicle below the ‘doorsteps’.

Power supply cabling

Table 29 shows what connection is connected with what colored cable. All the cables are accommodated with a banana plug which can be plugged into the DC/DC converter box in the trunk.

Table 29 Power supply cabling

	Power supply cabling		
	Voltage [V]	Left wheel	Right wheel
Conditioner box strain	0	Yellow	Brown
	15	Black	Blue
Conditioner box Eddy-current sensors	-15	Green -> Green	Green
	0	Black -> Brown	Black
	15	Red -> Yellow	Red

Cabling of the sensor signals

The sensor signals are transported via D-sub connectors from the conditioner boxes to the data acquisition unit. The details are given in Appendix G

Data acquisition unit: dSpace Autobox

The BMW is supplied with a data acquisition unit, the dSpace Autobox, to capture all the measurement signals. To the Autobox a laptop is connected on which the Autobox software is installed. This software in combination with Matlab/Simulink is used to measure and store the measurement data.



Figure 76 Data acquisition system: dSpace Autobox

The data is stored in .mat files. 24 channels are measured of which the overview is given in Table 49 in Appendix G.

5.2 Strain measurements: BETSY

The LSBs and knuckles have been tested on BETSY prior to the tests in the vehicle. Figure 77 shows a test run consisting of 24 load steps. It shows the applied forces in the upper graph and the measured strain in the lower graph.

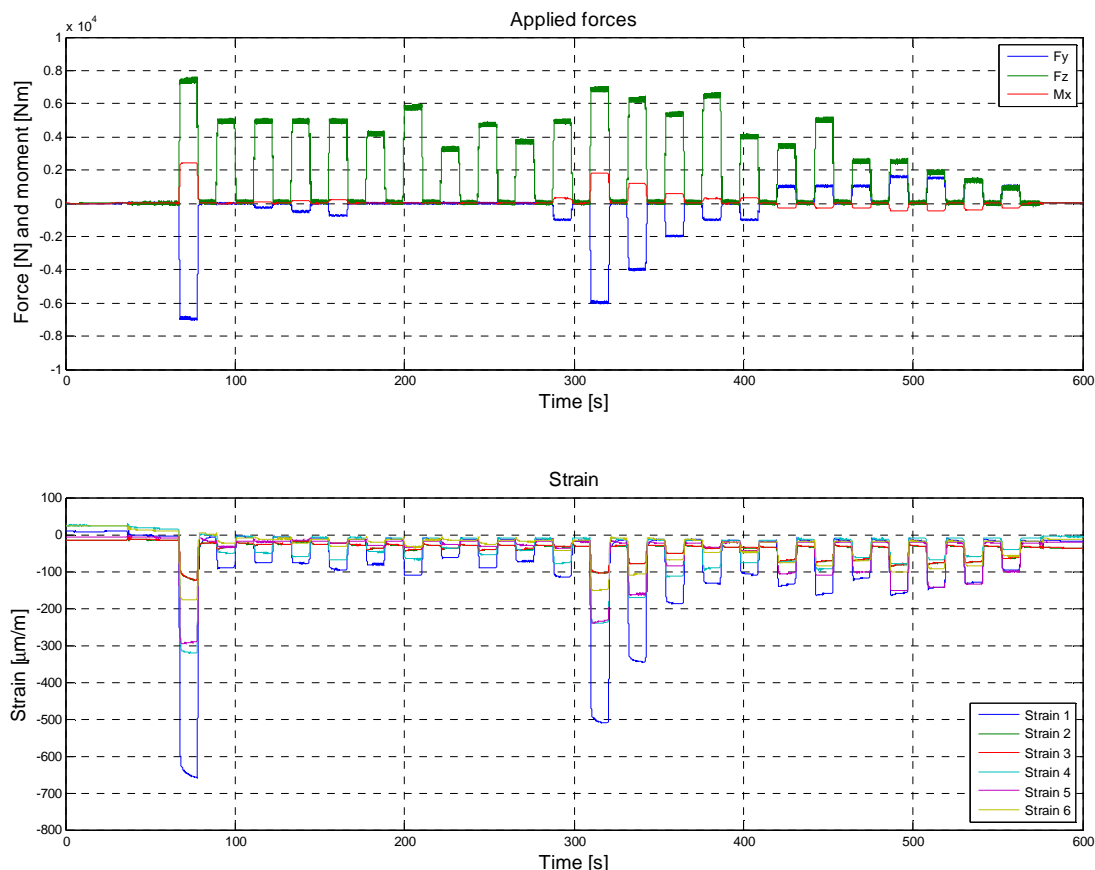


Figure 77 BETSY test run

Two things have been improved compared to the BETSY tests from 2011. The first thing is that the BETSY measurements from 2011 were performed, as explained in section 4.2.1, at 500 rpm = 8.33 Hz. Therefore a disturbing component was present in the dynamic frequency band from 1 Hz to 10 Hz. Current tests have been performed at 1000 rpm = 16.66 Hz. The disturbance falls therefore outside the dynamic bandwidth of interest.

The second thing is that the tests from 2011 were performed at half load, see section 2.4. Therefore the applied forces were only half of the forces which were measured during the field measurements. Now, the full load is applied and the forces follow the same F_y vs. F_z as is measured in the field.

Besides the improvements, something else went wrong. The lower graph shows that only five strain signals are visible. Strain gauge 2 and 3 show exactly equal strain, Probably because of an error in the BETSY software, the strain from strain gauge 2 has been lost. When, in section 5.9.2, force estimations with BETSY calibration are performed, strain gauge 2 will be omitted.

Table 30 shows the correlation coefficients for the semi-static and the dynamic parts for both positive- and negative F_y . An increase in correlation is obtained in contrast to the coefficients found using the BETSY experiments from 2011 in Chapter 3. This can be explained by bigger range of applied forces and the increase in frequency of rotation of the LSB. The dynamic parts of F_y and the strain are again completely uncorrelated.

Table 30 Correlation coefficients between F_y and strain for the field measurements

Strain gauge	Correlation coefficient between F_y and strain measured on BETSY			
	R_{xy} low ($F_y > 0$)	R_{xy} low ($F_y < 0$)	R_{xy} high ($F_y > 0$)	R_{xy} high ($F_y < 0$)
1	0,41	-0,99	-0,01	-0,04
2	0,89	-0,95	0,00	-0,03
3	0,89	-0,95	0,00	-0,03
4	0,10	-0,98	0,01	-0,04
5	0,98	-0,98	0,00	-0,04
6	0,85	-0,99	0,01	-0,04

5.3 Strain measurements: Field

Several test have been performed at the test track of SKF, Nieuwegein. Several test of 30 seconds have been performed at 10 km/h, 20 km/h and 30 km/h while driving a left or a right cornering maneuver. Also tests have been performed for which left and right cornering and the speeds are varied randomly. An overview of the performed tests can be found in Appendix D.

For a first analysis to check if the data acquisition is working properly, in Figure 78 the measured signals during several tests are shown. The tests which are used are the tests for which a left- or right corner is driven at nearly constant speed. Every sensor has its own graph. The six graphs contain the signals of the strain gauges. The signals of the strain gauges have been low pass filtered with a cutoff frequency of 10 Hz.

The VELOS wheel is used to measure the load at the wheel. These measurements are used as reference. Figure 79 shows for the same seven tests as in Figure 78 what is measured. The upper right graph shows that for the lateral F_y increases with increasing speed, with positive force for left corners and negative force for right corners. The used BMW is a rear wheel driven car, therefore the graphs for F_x and M_y only show negative force/moment during a braking maneuver as is the case for the reference test.

Measured strain signals for different tests

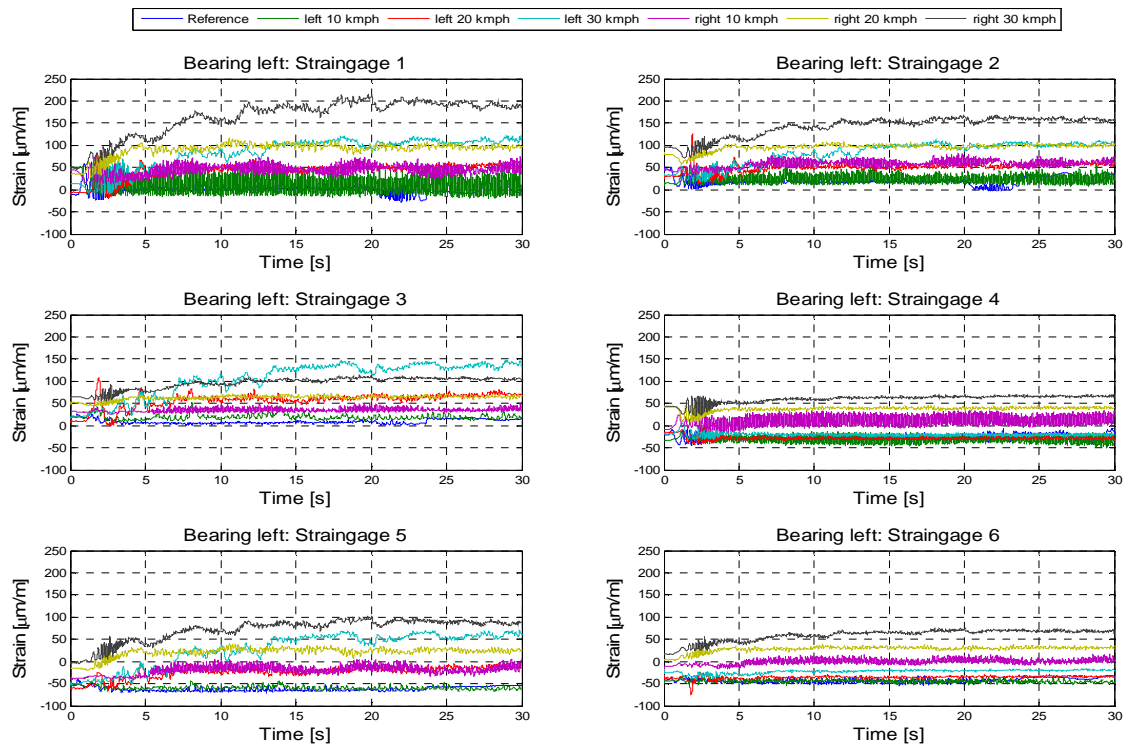


Figure 78 Measured signals: left bearing/knuckle

Velos: measured forces and moments

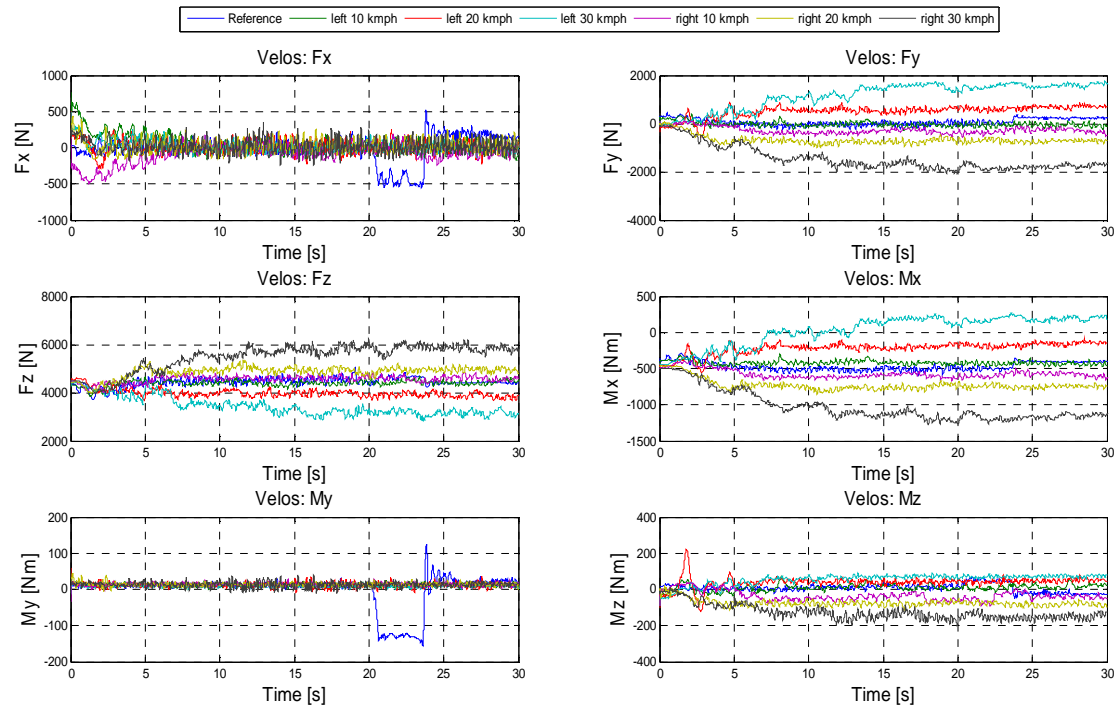


Figure 79 VELOS measured forces and moments

5.3.1 Correlation

Table 31 shows the correlation coefficients between F_y and the six strain gauges for both positive and negative F_y for the semi-static and dynamic content. As for the measurements on BETSY the low frequent content shows significant more correlation than the dynamic content. However, for the dynamic positive lateral forces non-negligible coefficients are observed. What has caused this increase in correlation compared to the measurements on BETSY is unknown.

Strain gauge 4 and 6 show the lowest correlation for $F_y > 0$ (Excluding the high frequent content for negative F_y). This can be explained by the unresponsiveness of these strain gauges on positive lateral force. The unresponsiveness is shown in Figure 80 in section 5.7.

Table 31 Correlation coefficients between F_y and strain for the field measurements

Correlation coefficient between F_y and strain measured the field measurements				
Strain gauge	R_{xy} low ($F_y > 0$)	R_{xy} low ($F_y < 0$)	R_{xy} high ($F_y > 0$)	R_{xy} high ($F_y < 0$)
1	0,97	-0,99	0,50	-0,02
2	0,95	-0,97	0,52	-0,01
3	0,98	-0,97	0,70	-0,02
4	-0,33	-0,88	-0,08	-0,01
5	0,99	-0,99	0,64	-0,02
6	0,50	-0,95	0,13	-0,01

5.4 Comparison strain measurements: BETSY and field

In this section the measurements of the strain gauges will be discussed. First, as in section 2.9, the lateral force will be plotted versus the strain for all the strain gauges. The observed V-shapes will again be approximated by linear fitlines, $\epsilon_{left} = c_{1,left} \cdot F_{y,left} + c_{2,left}$ and $\epsilon_{right} = c_{1,right} \cdot F_{y,right} + c_{2,right}$. The transformation coefficients c_A and c_B to transform the strain signals measured in the vehicle to the signals which would have been measured on BETSY when loaded with the same lateral force will again be determined. These coefficients will create the opportunity to use BETSY as the calibration system. As was explained in section 2.9 it is necessary that the measurements on BETSY and in the field are reproducible for BETSY being a valid calibration system. In section 5.8 the reproducibility of the BETSY- and field measurements is discussed.

Figure 80 shows the lateral force versus the strain for the measurements performed at BETSY and on the test track of SKF. Whereas for the Papenburg measurements an offset in the lateral force of 400 N was present, an offset of 200 N is observed for the measurements at SKF. This offset is again compensated for.

The responses are comparable but some differences in sensitivity can still be observed as was the case for the Papenburg tests.

Fy vs strain for the BETSY- and the field measurements

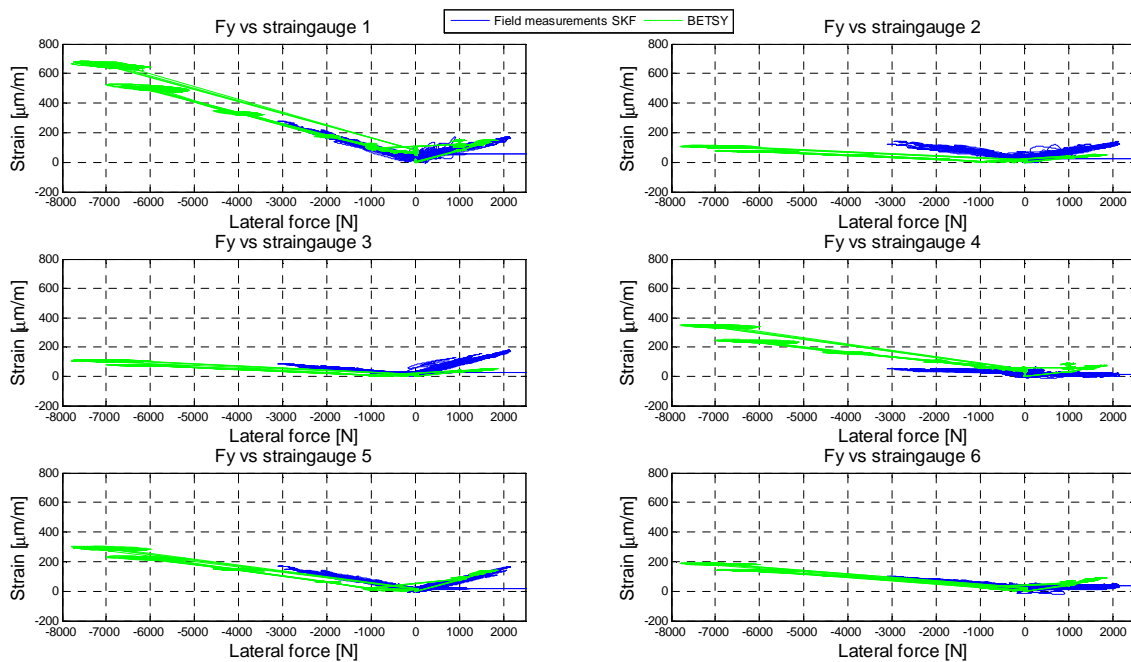


Figure 80 Lateral force vs. strain for tests performed at BETSY and at SKF

Table 32 shows the coefficients of the linear approximations for $F_y > 0$, $\varepsilon_{left} = c_{1,left} \cdot F_{y,left} + c_{2,left}$ and $F_y < 0$, $\varepsilon_{right} = c_{1,right} \cdot F_{y,right} + c_{2,right}$. Where left and right denote the turning maneuver as seen from the driver's seat of the vehicle.

Table 32 F_y - strain linear fit coefficients

Strain gauge	BETSY				SKF field measurements			
	Right		Left		Right		Left	
	Slope [µm/m/N] = $c_{1,right}$	Offset [µm/m] = $c_{2,right}$	Slope [µm/m/N] = $c_{1,left}$	Offset [µm/m] = $c_{2,left}$	Slope [µm/m/N] = $c_{3,right}$	Offset [µm/m] = $c_{4,right}$	Slope [µm/m/N] = $c_{3,left}$	Offset [µm/m] = $c_{4,left}$
1	-0,078	50,812	0,078	22,202	-0,072	35,183	0,061	33,523
2	-0,012	2,880	0,028	4,729	-0,037	31,009	0,048	25,065
3	-0,012	2,881	0,028	4,727	-0,020	17,793	0,072	18,474
4	-0,038	35,405	0,035	13,571	-0,011	23,355	-0,006	21,523
5	-0,038	-2,328	0,080	3,071	-0,049	12,308	0,070	4,101
6	-0,023	7,767	0,047	5,790	-0,023	27,734	0,005	22,754

Table 33 shows the transformation coefficients c_A and c_B where $c_A = c_A = \frac{c_1}{c_3}$ and

$c_B = c_2 - \frac{c_1 \cdot c_4}{c_3}$. These coefficients will be used in section 5.9.2 where the lateral force on the vehicle will be estimated using a BETSY calibration.

Table 33 Transformation coefficients

Strain gauge	Right		Left	
	C_A	C_B	C_A	C_B
1	1,08	12,89	1,29	-20,95
2	0,33	-7,42	0,58	-9,91
3	0,62	-8,08	0,39	-2,45
4	3,48	-45,84	-6,05	143,75
5	0,77	-11,82	1,14	-1,61
6	1,04	-21,09	9,80	-217,15

Strain gauge 2 and 4 show the biggest difference in response. It has to be noted that there might exist a chance that the signals have been switched. When switched the responses for BETSY and in the field would be equal. This can be checked using Table 32. Because the differences in the slope are compensated for it will not cause any problems in the force estimation and it will be left like this.

5.5 Eddy-current sensor measurements: BETSY

Figure 81, shows the lateral force F_y as a function of the measured deflections at the top and bottom of the of the ABS-ring. As was the case for earlier performed BETSY measurements, also this time a nice trend can be observed for both the upper and lower sensor.

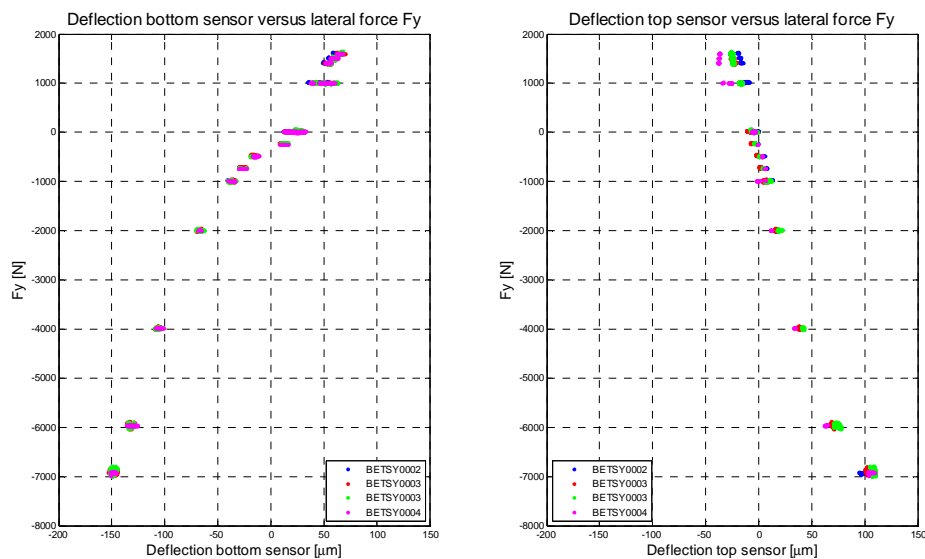


Figure 81 BETSY measurements: lateral force versus the measured deflection. Left plot: top sensor. Right plot: bottom sensor

Figure 82 shows the trend between the tilt and lateral force. We will see that this trend coincides with the trend observed for the BETSY 2011 data of Chapter 4 and also for the trend measured in the actual vehicle.

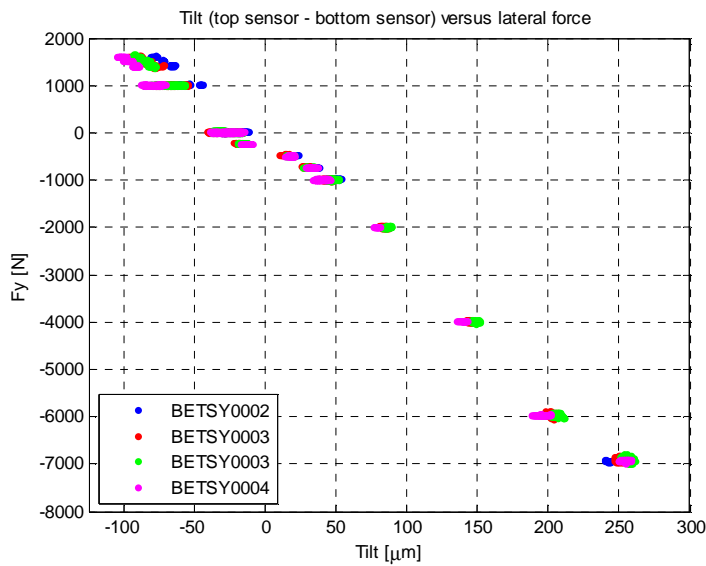


Figure 82 BETSY measurements: tilt vs. the lateral force F_y

The trend is again approximated by first to sixth order polynomials as shown in Figure 83. As in Chapter 4 this is also done for the trends observed using only the bottom- and only the top sensor. These figures can be seen in Appendix E

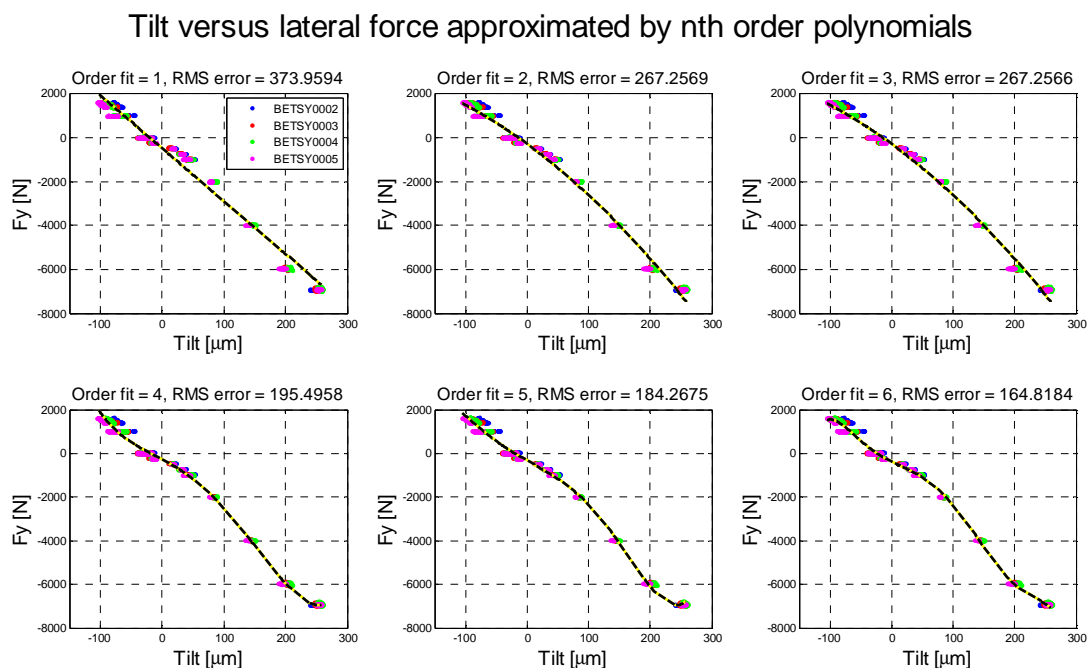


Figure 83 BETSY measurements: tilt versus lateral force approximated by n-th order polynomials

The RMS-fit errors are shown in Table 34. The fits for the tilt show the lowest error. Increasing the order to a sixth one, decreases the RMS-error significantly. Within the measured domain it is desirable to take a sixth order fit. One has to notice however that the extrapolation characteristics will be very inaccurate outside the measured domain so the sixth order trend can only be used within the measured range. Furthermore it is of

importance that we have the ability to do a calibration on BETSY. An higher order fit will make it more difficult to transform the observed trend measured in the vehicle to the trend measured on BETSY. This will be further explained in section 5.7

Table 34 BETSY measurements polynomial fit errors

Order	Fit errors		
	Tilt [N]	Bottom [N]	Top [N]
1	373,96	555,38	436,20
2	267,26	343,41	420,82
3	267,26	208,63	273,41
4	195,50	171,56	258,02
5	184,27	158,16	257,35
6	164,82	155,50	256,98

5.6 Eddy-current sensor measurements: Field

5.6.1 Eddy-current sensor signals

The Eddy-current sensor signals measured during the field measurements at the test track at SKF are conditioned in almost the same way the signals are conditioned during the tests on BETSY. Figure 84 shows that these signals are more subject to noise and the amplitude is decreased by a factor 7 for the left bearing and a factor 3 for the right bearing. Due to the high frequent noise the detection of the steepness down or up cannot be distinguished from the oscillations during the minima intervals by focusing on the derivative.

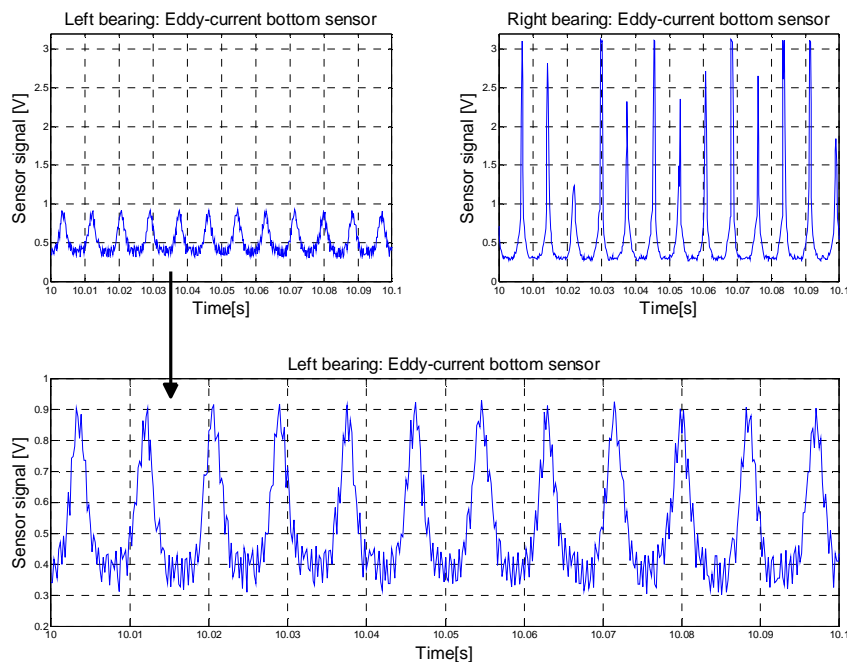


Figure 84 Measured Eddy-current signals during the field measurements.

5.6.1.1 Additional (velocity dependent) moving average filter

To overcome this problem a moving average filter is applied to the signals using $n=10$ data samples. The induced time shift is compensated for. This filter, which is shown at the end of this section, averages the signals over 10 data samples smoothing the noise during the minima and thereby making the slope during these minima smaller than the

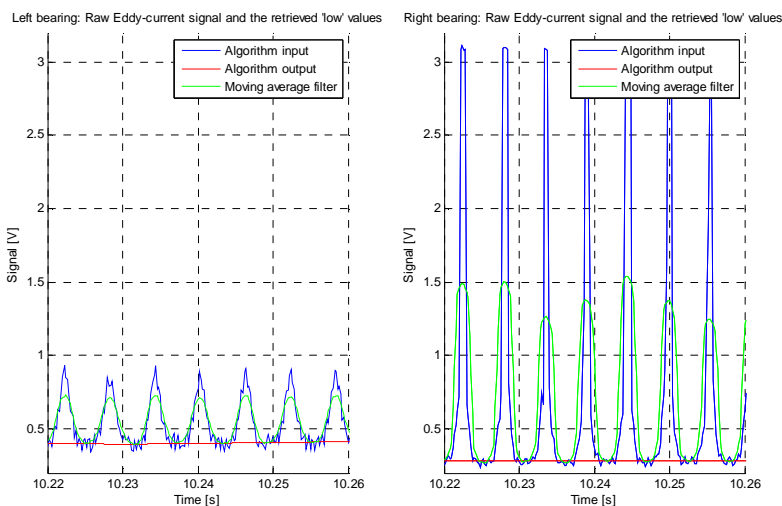


Figure 85 Eddy-current sensor signal measured during the field measurements at the SKF test-track including the moving average filtered signals

slope during the peaks. Now, the derivative condition in the algorithm is therefore met and the algorithm is able again to follow the minima. See Figure 85. In blue the original signal is shown. The green line represents the signal subject to the moving average filter and the red line the output of the algorithm.

Time shift

A moving average filter introduces a time shift of $n/2$ samples. This time shift is compensated for in the algorithm. It has to be noticed that this is only possible during post processing.

Moving average filter: algorithm addition

The following algorithm is added to the existing algorithm:

```

n = 10
for k = 1 : length(x) - 1
    if k > n;
        x_movavg(k) = mean(x(k-n:k));
    else
        x_movavg(k) = 0;
    end
end
x_movavg(length(x):length(x) + n/2) = 0

```

Time shift compensation

```

For k = 1 : length(x_movavg) - n/2
    x_movavg(k) = x_movavg(k + n/2);
end

```

Velocity dependence

While the tests runs at BETSY were performed at a constant speed, the speed during the field measurements was varying. When the wheel speed increases, the slope of the peaks increases, thereby decreasing the robustness of the derivative condition. It had been necessary for some tests to define different derivative bounds for different time intervals by adding the following piece of algorithm:

Else if ($k > k_{t1} \parallel k < k_{t2}$)

$y_{low} = y_1$

$y_{high} = y_2$

Where k_{t1} and k_{t2} define the interval of samples between time t_1 and t_2 and y_1 and y_2 define the bounds for the derivative condition.

5.6.2 Sampling rate

The sampling rate should be high enough to distinguish the peaks and values in the Eddy-current sensor signals. To be more specific it is necessary to have more than one sample during every valley and peak. Only then the algorithm to extract the lower values will work correctly. This is because the algorithm works with the slope (derivative) of the signal. When the slope of the signal is close to zero the algorithm detects a valley. If the sample rate is too low (as it has been the case) and only one sample or less is sampled during a valley of peak, the derivative will never become zero and the algorithm does not work properly.

What sampling rate is needed then to accurately measure the signals?

The rim of the wheel has a diameter of 17 inch. The tire's code is 225/50 R17. This means the radius of the wheel is $r_{wheel} = 0.33$ m. The circumference of the wheel s_{wheel} is determined to be approximately 2.06 m. On the test track at SKF the maximum velocity which can be driven is around $v_{max} = 50$ km/h = 13.98 m/s. The maximum frequency of wheel rotation will then be $f_{wheel,max} = v_{max}/s_{wheel} = 6.74$ Hz.

The ABS-ring contains 48 holes. This means 96 flanges need to be recognized during one rotation of the wheel and ABS-ring. When driving at the maximum allowed speed the minimum sample frequency becomes

$$f_{sample,min} = f_{wheel,max} \cdot 2 \cdot N_{flanges} = 6.74 \text{ Hz} \cdot 2 \cdot 96 = 1294 \text{ Hz} \quad (5.1)$$

Where $N_{flanges}$ is the total amount of flanges encountered during one revolution of the wheel and the factor 2 is included because of the Nyquist criterion.

To have at least more than one sample during every hole and non-hole the sample frequency is set to 5000 Hz = 5 kHz. Choosing 5 kHz is a factor 3.86 higher than $f_{sample,min}$. A valley will thus be measured with almost 8 samples.

5.6.3 F_y - tilt curves field SKF

This section will show the observed relations between tilt and lateral force measured in the actual vehicle. In Figure 86 the trends are shown between the lateral force and the bottom- and top sensor. In Figure 87 the lateral force is plotted versus the tilt. It is shown that the trends are very similar to the trends measured on BETSY.

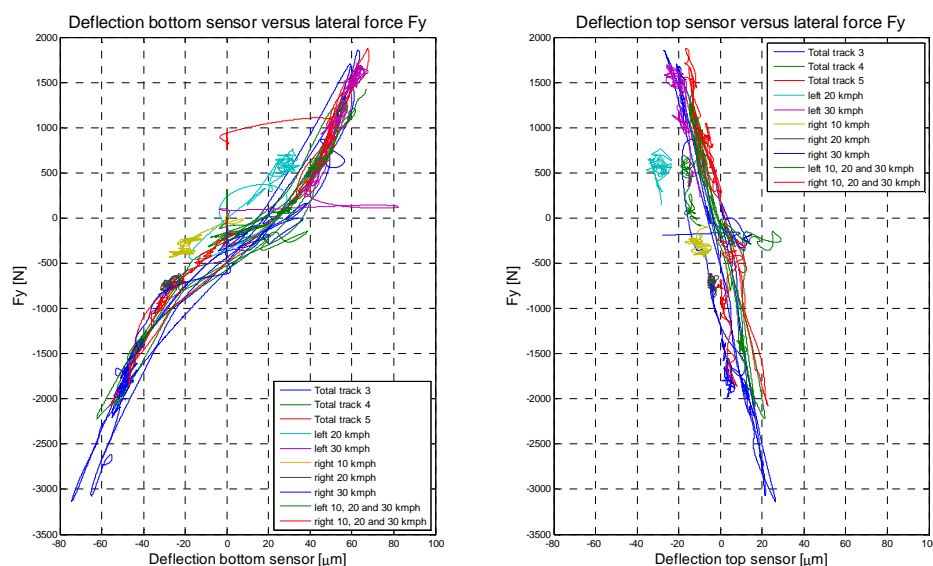


Figure 86 Lateral force versus the measured deflection. Left plot: top sensor. Right plot: bottom sensor

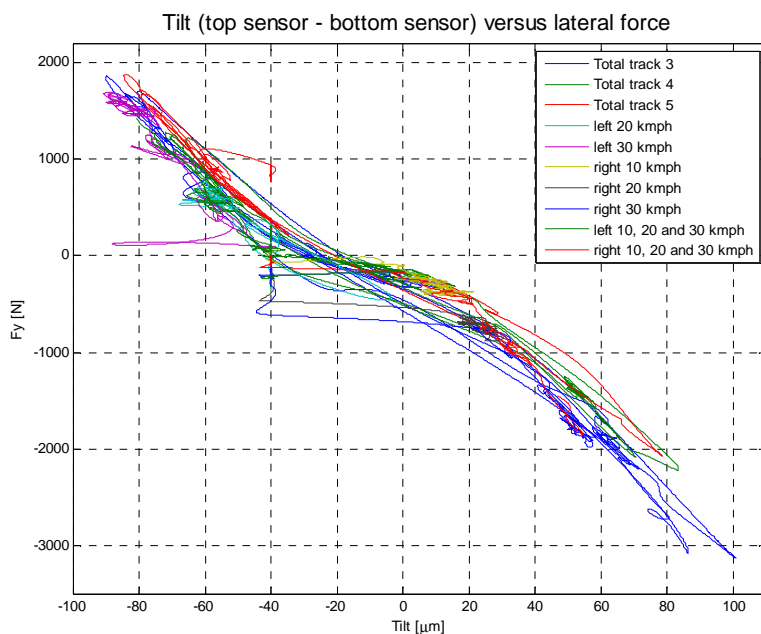


Figure 87 Field measurements: tilt vs. the lateral force F_y

Once again as in the previous section the relations between lateral force and top deflection, bottom deflection and tilt are approximated by first to sixth order polynomials.

Of which the F_y versus tilt is shown in Figure 88. The figures for the F_y - top deflection and the F_y - bottom deflection are shown in Appendix E

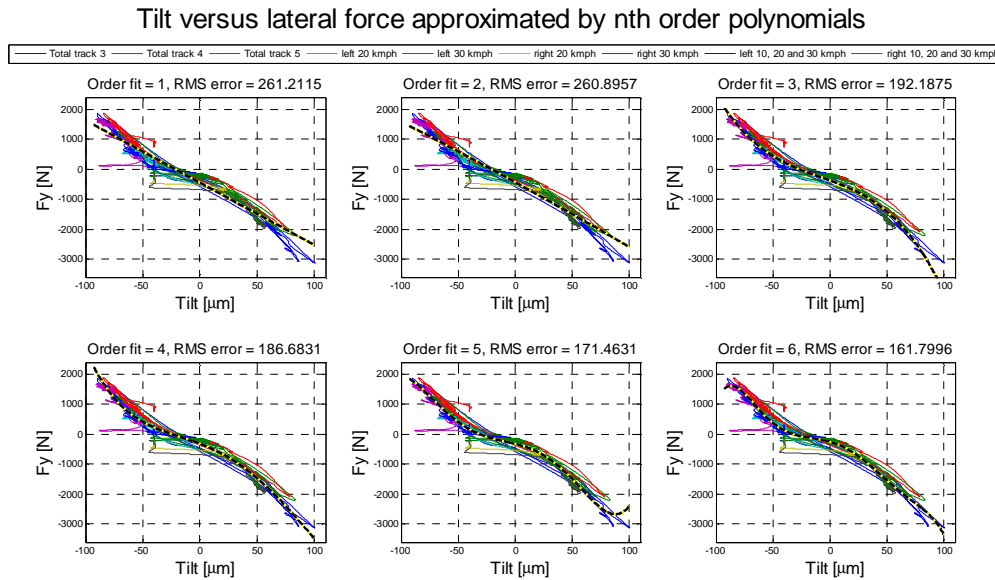


Figure 88 Field measurements: tilt versus lateral force approximated by n-th order polynomials

Table 35 shows the fit errors. As for the measurements on BETSY the smallest error is again obtained for the F_y versus tilt relation.

Table 35 BETSY measurements polynomial fit errors

Order	Fit errors		
	Tilt [N]	Bottom [N]	Top [N]
1	261,21	289,21	702,46
2	260,90	277,01	698,67
3	192,19	199,45	614,57
4	186,68	196,93	612,25
5	171,46	194,38	613,51
6	161,80	194,29	606,35

In Chapter 4, where the BETSY of 2011 is analyzed it was seen that using only the top sensor would give the best estimation result. So contrary to what is seen in Chapter 4, this time the tilt would give the best results for lateral force estimation.

5.7 Comparison Eddy-current sensor measurements: BETSY and field

In this section the Eddy-current sensor measurements, the F_y - tilt relations, for the BETSY- and the field measurements will be compared. It will be discussed how BETSY can be used as calibration system for these Eddy-current sensors.

For an n_{th} order fit the relation measured on BETSY can be described by

$$F_{y,B} = c_{0,B} + c_{1,B} \cdot x_{\text{tilt},B} + \dots + c_{n-1,B} \cdot x_{\text{tilt},B}^{n-1} + c_{n,B} \cdot x_{\text{tilt},B}^n = \sum_{k=0}^n c_{k,B} \cdot x_{\text{tilt},B}^k \quad (5.2)$$

And for the field measurements can be written

$$F_{y,F} = c_{0,F} + c_{1,F} \cdot x_{\text{tilt},F} + \dots + c_{n-1,F} \cdot x_{\text{tilt},F}^{n-1} + c_{n,F} \cdot x_{\text{tilt},F}^n = \sum_{k=0}^n c_{k,F} \cdot x_{\text{tilt},F}^k \quad (5.3)$$

Where the B stands for BETSY and the F for field.

Figure 89 shows the lateral force as a function of the tilt for the field- as well as the BETSY measurements. The left graph shows second order fits and the right one shows sixth order fits.

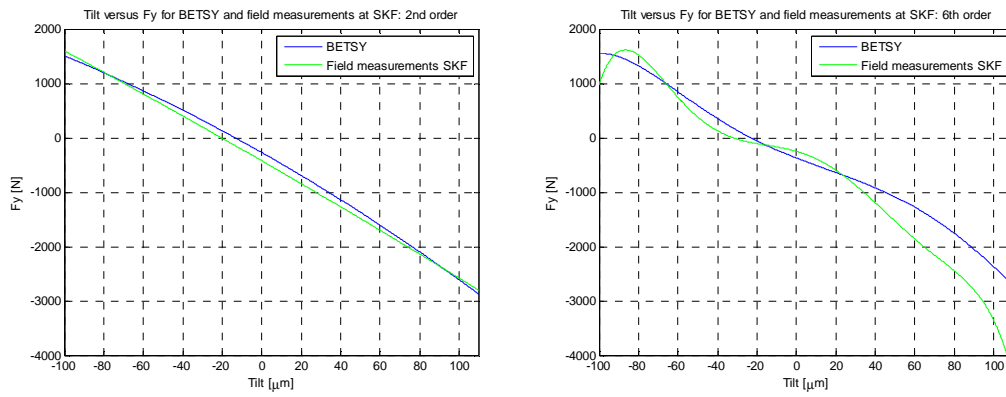


Figure 89 Tilt vs. F_y measured on BETSY and during the field measurements. Left: 2nd order. Right: 6th order

For the second order case the following equations can be written

$$F_{y,BETSY} = -0.0282 \cdot x_{\text{tilt}}^2 - 20.5586 \cdot x_{\text{tilt}} - 266.5474 \quad (5.4)$$

$$F_{y,Field} = -0.0069 \cdot x_{\text{tilt}}^2 - 20.8642 \cdot x_{\text{tilt}} - 418.6864 \quad (5.5)$$

And for the sixth order case:

$$F_{y,BETSY} = -1.3997 \cdot 10^{-10} \cdot x_{\text{tilt}}^6 + 6.9823 \cdot 10^{-8} \cdot x_{\text{tilt}}^5 - 5.5699 \cdot 10^{-6} \cdot x_{\text{tilt}}^4 - 1.2399 \cdot 10^{-3} \cdot x_{\text{tilt}}^3 + 0.0662 \cdot x_{\text{tilt}}^2 - 14.1231 \cdot x_{\text{tilt}} - 369.933 \quad (5.6)$$

$$F_{y,Field} = -5.5470 \cdot 10^{-9} \cdot x_{\text{tilt}}^6 + 3.0900 \cdot 10^{-7} \cdot x_{\text{tilt}}^5 + 7.3989 \cdot 10^{-5} \cdot x_{\text{tilt}}^4 - 4.197 \cdot 10^{-3} \cdot x_{\text{tilt}}^3 - 0.2791 \cdot x_{\text{tilt}}^2 - 10.55 \cdot x_{\text{tilt}} - 246.722 \quad (5.7)$$

Two methods are possible for using BETSY as calibration system.

The first is to directly use the relation measured on BETSY in the vehicle. This will introduce an error because the behaviour is not equal for both cases. For the second order case this error will have an RMS value of 114.55 N. For the sixth order case this will be 175.59 N. These errors will add up to the error introduced by the fit of the data, which are approximately 260 N for the second order and 160 N for the sixth order.

Secondly it is possible to make a transformation to the relation found in the vehicle by using $n+1$ multiply factors for the polynomial coefficients:

$$c_{k,transformation} = \frac{c_{k,F}}{c_{k,B}} \text{ for } k = \{0..n\} \quad (5.8)$$

To get the polynomial coefficients in the field:

$$c_{k,F} = c_{k,transformation} \cdot c_{k,B} \text{ for } k = \{0..n\} \quad (5.9)$$

When transforming the coefficients the error introduced by the differences in behaviour is compensated for.

But for higher order polynomials more coefficients need to be transformed. For now, the coefficients of BETSY as well as the coefficients for the field are available and the transformation can be performed without any error. One has to take notice of the fact that when BETSY is used for calibration of a LSB which has not been tested in the field the particular behaviour in the field is unknown. Then, for a slightly different behaviour in the vehicle, errors will be introduced with every transformation coefficient and will be increasing with increasing order.

For an higher order fit the error is less, but the extrapolation characteristics are worse.

The measured range of lateral force in the vehicle lies between the -3000 N to 1500 N. For sixth order fits, this would automatically be the valid usable range for force estimation because extrapolation is not possible, In the lower right of Figure 88 the curves deflects outside this range. For second order fits this range can be extrapolated to a range between -8000 N and 2000 N (not shown in Figure 89).

When keeping in mind that the extrapolation characteristics are bad for a sixth order fit and force estimations can only be performed for a certain range of forces the best option to use BETSY as calibration machine is by using the coefficient transformation method with sixth order fits. In this way the data fit errors are the smallest and the difference in behaviour is compensated for. Besides the extrapolation drawback one also has to keep in mind that this is not necessarily the best option when using another vehicle. Conclusions about that can only be drawn after it has been shown that the responses in different vehicles are equal. This is unfortunately outside the range of this research.

5.8 Reproducibility

In this section the reproducibility of the measurements on BETSY and in the field will be investigated. In 5.8.1 the strain measurements on BETSY will be discussed. In 5.8.2 the tilt measurements on BETSY and in 5.8.3 the strain measurements in the field. As explained in Chapter 2, all these measurements need to be reproducible when it is wanted to use BETSY as calibration system for a whole production line of LSBs. The reproducibility of the tilt measurements in the field cannot be checked, because only one vehicle is thus far supplied with Eddy-current sensors.

5.8.1 BETSY measurements: Strain

As explained, the measurements performed on BETSY and the tests performed in the field need to be reproducible. In this section the reproducibility of the BETSY measurements are investigated.

The following test runs are used in the analysis:

- BMW0005 – BMW0008
- BMW0010 – BMW0013
- BMW0015 – BMW0018

In Figure 90 the $F_y - \varepsilon$ curves are shown for the three above mentioned different BETSY test runs. The linear approximations of the three runs are also shown by three black lines. The differences in the slopes of the three black lines indicate the tests are not fully reproducible.

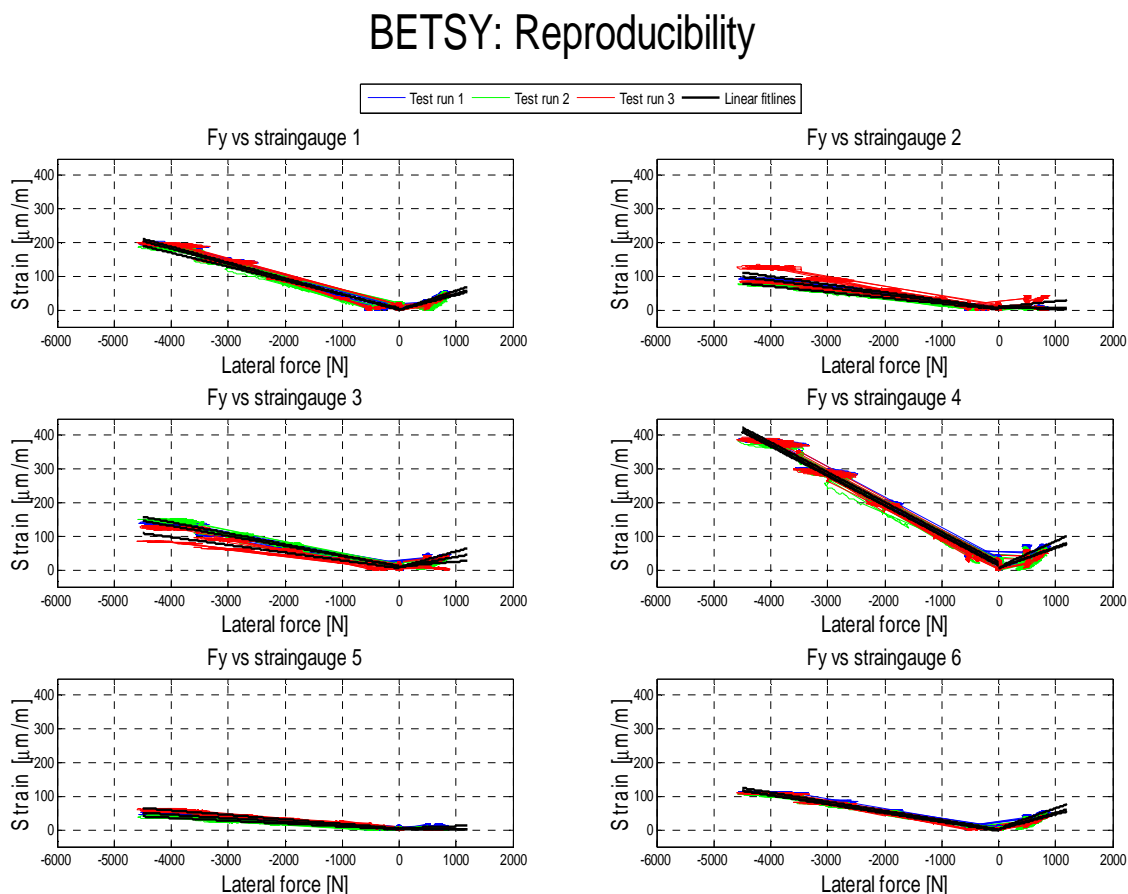


Figure 90 F_y - strain curves for three BETSY test runs

In Table 36 the coefficients are given of both the left- and right cornering behaviour for the three BETSY test runs.

To quantize the reproducibility of the BETSY tests the RMS-value of the difference between the measured strain and the strain estimated by an average of the three fit lines will be used.

Table 36 Slopes and offsets of the linear fits of the three BETSY test runs

Strain gauge	Testrun BMW0005 - BMW 0008				Testrun BMW0010 - BMW 0013				Testrun BMW0015 - BMW 0018			
	Right		Left		Right		Left		Right		Left	
	Slope [$\mu\text{m}/\text{m}/\text{N}$]	Offset [$\mu\text{m}/\text{m}$]										
1	-0,047	0,107	0,057	-0,048	-0,041	5,130	0,044	-0,160	-0,045	2,129	0,048	-0,459
2	-0,021	3,714	-0,005	10,207	-0,017	1,714	-0,005	7,442	-0,024	5,468	0,018	7,552
3	-0,030	11,846	0,047	7,736	-0,033	10,210	0,031	7,173	-0,023	5,596	0,014	10,132
4	-0,089	23,996	0,076	8,532	-0,088	17,175	0,063	4,958	-0,090	13,153	0,059	5,841
5	-0,010	3,259	0,006	4,966	-0,009	1,652	0,000	4,099	-0,013	4,426	0,000	2,535
6	-0,027	2,311	0,060	4,266	-0,026	0,102	0,049	2,171	-0,027	-2,761	0,044	1,540

To give an indication of the reproducibility per strain gauge the RMS-error of every strain gauge is given in Table 37.

Table 37 Reproducibility errors of the strain gauge response

Strain gauge	Root mean square error	
	Right [$\mu\text{m}/\text{m}$]	Left [$\mu\text{m}/\text{m}$]
1	6,38	5,61
2	4,19	9,45
3	5,13	8,30
4	7,56	7,69
5	2,22	3,33
6	2,80	4,17

After the determination of the calibration matrix coefficients using a multivariate linear regression analysis, it can be determined what error could be introduced by the spread in the strain signals and what error has to be accepted when using BETSY as a calibration system.

5.8.2 BETSY measurements: tilt

When one would compare Figure 81 in section 5.5 (BETSY data 2012) with Figure 56 in section 4.3 (BETSY data 2011) the relations seems to be inconsistent. Assuming that both the channels of the top- and bottom sensor have been switched and the signs have been changed, then the mirrored version of Figure 56a results in Figure 81b and Figure 56b results in Figure 81a.

As a result, the tilt, which is again the top deflection minus the deflection at the bottom, is equal. This is shown in Figure 91. It shows a 2nd order fit of the F_y – tilt trend for the older BETSY data from 2011 and the newer BETSY data from 2012.

The 2nd order fits perfectly match, indicating a good reproducibility of the BETSY measurements. The figure also shows that the extrapolation characteristics are good for a second order fit. Whereas for the 2012 BETSY data lateral forces are applied in the range from -2000 N to 8000 N, the applied lateral force for the 2011 BETSY data were in the range from -1000 N to 4000 N. Still, the 2nd fit of the older BETSY data coincides with the 2nd order fit of the newer BETSY data outside the range of the applied lateral force.

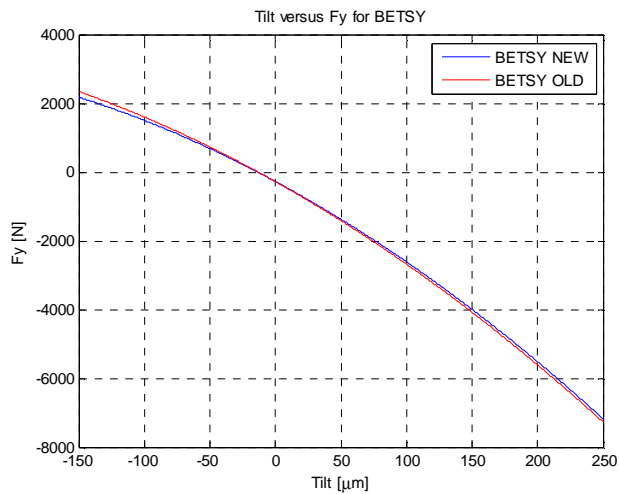


Figure 91 Second order polynomial relation of the lateral force vs. the tilt for the old and new BETSY data

Figure 92 shows that for a sixth order fit the match is only good on a certain range of tilt. The two curves now only match on the range of lateral force which had been applied retaining the 2011 BETSY data. Although there is still a good reproducibility of the tilt measurements on BETSY, it does show that for sixth order approximations the extrapolation characteristics are bad and can only be used within the range of applied force.

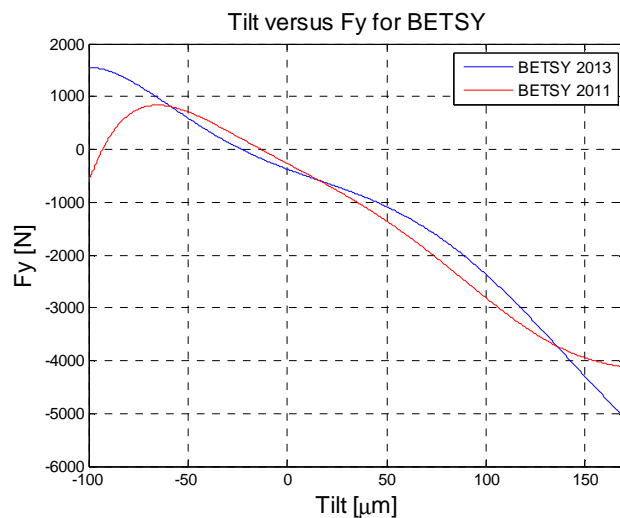


Figure 92 Sixth order polynomial relation of the lateral force vs. the tilt for the 2011 and 2012 BETSY data

5.8.3 Field measurements: strain

So far it is seen that for a particular LSB the strain gauge responses on BETSY are comparable with those in the actual vehicle. The differences are compensated for by describing the responses by first order polynomials. We have also seen that the measurements on BETSY are reproducible to a certain extent. Now it will be shown to what extent the field measurements are reproducible. As explained, this is a requirement

for using BETSY as calibration system for LSBs in a production line. Figure 93 shows the $F_y - \varepsilon$ curves for the field measurements performed in Papenburg (red) and at SKF (blue).

Fy vs strain for the field measurements performed at SKF and Papenburg

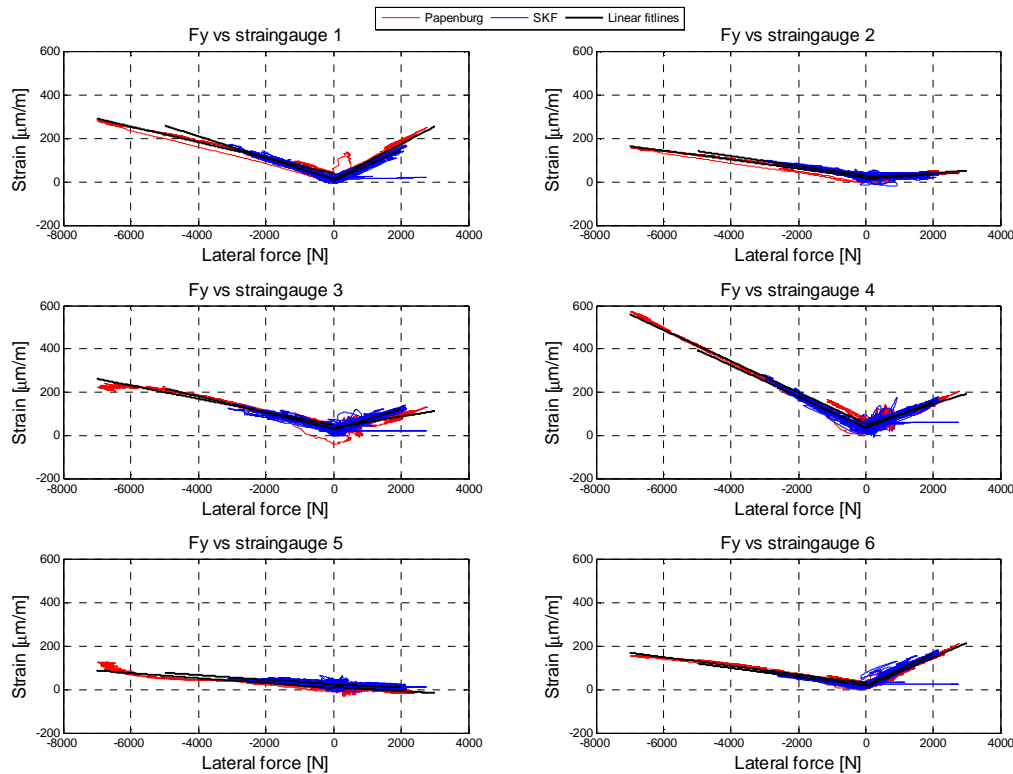


Figure 93 Lateral force vs. strain for the field measurements performed in Papenburg and at SKF

It turned out that the physical numbering of the LSBs in the BMW is not the same as the physical numbering used for the earlier BETSY measurements and the tests in Papenburg. It is assumed that the numbering used during the Papenburg measurements is as is shown in Figure 4. Table 38 shows what strain gauges correspond with each other for the different LSBs.

Table 38 Numbering LSB

Strain gauge	
Papenburg	SKF
1	5
2	6
3	2
4	1
5	4
6	3

As was seen in Chapter 2, strain gauges 2 and 5 did not show a response for positive lateral force and it was mentioned that these strain gauges should be omitted from the MLRA when performing a force estimation (for $F_y > 0$). For the current LSB these strain

gauges are designated by the numbers 4 and 6. These two will therefore be disregarded from the estimations using the MLRA in section 5.9.

To quantize the reproducibility of the BETSY tests the RMS-value of the difference between the two first order polynomials is taken for every strain gauge.

Table 39 Reproducibility errors of the strain gauge response

Strain gauge	Root mean square error	
	Right [$\mu\text{m/m}$]	Left [$\mu\text{m/m}$]
1	20,56	17,5
2	13,39	5,48
3	9,87	18,25
4	20,15	7,55
5	15,65	13,67
6	10,56	12,73

5.9 Algorithm force estimation

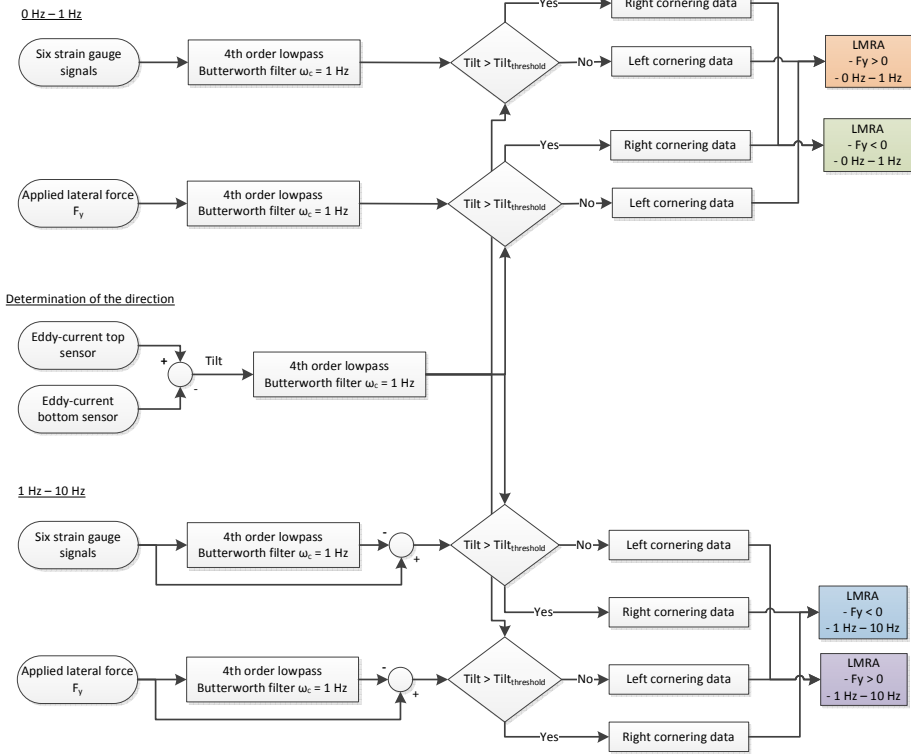
This section will show the results of the force estimations. First using an in situ calibration (section 5.9.1) and secondly using a BETSY calibration (section 5.9.2). The calibrations and validations are performed with a set of tests performed at the test track of SKF, Nieuwegein. The validation test is logically not included within the tests used for the calibration.

For both the in-situ and BETSY calibration, the lateral force is estimated using two different algorithms.

The first is the algorithm of Chapter 3 where the force is estimated by four MLRAs. One for the semi-static positive lateral force, one for semi-static negative lateral force, one for the dynamic part of positive lateral force and one for the dynamic part of the negative lateral force. Whereas Chapter 3 was based on BETSY measurements, there was a clear distinction between positive and negative F_y , as imposed by the load profile. For the field measurement the separation between positive and negative F_y is less straightforward, because the strain gauges suffer with the ‘absolute value problem’ and are not able to determine whether the lateral force is positive or negative. Fortunately the tilt measurements using the Eddy-current sensors have been introduced in Chapter 4. The measured tilt does not suffer with the ‘absolute value problem’ and does have the possibility to determine the direction. Therefore the tilt measurement is included in the algorithm of Chapter 3 to determine the direction and the corresponding MLRA, see Figure 94.

The second is the method from Chapter 4 where the low frequent part of the lateral force is estimated by the tilt of the inner ring/ABS-ring of the LSB, and where the dynamic part is estimated by measured deformations using a MLRA on the strain gauges. The tilt measurement is included to determine the direction and the corresponding MLRA of the dynamic lateral force, see Figure 95.

Calibration



Estimation

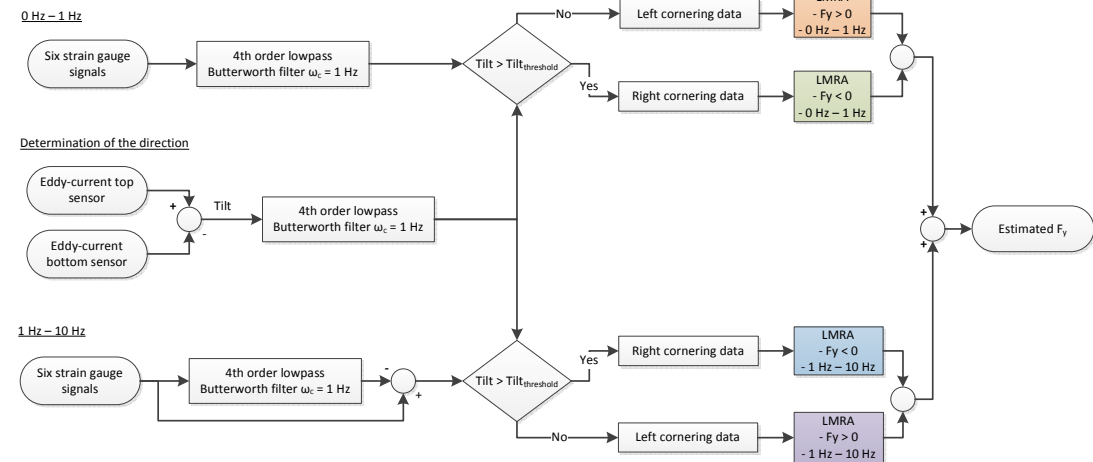
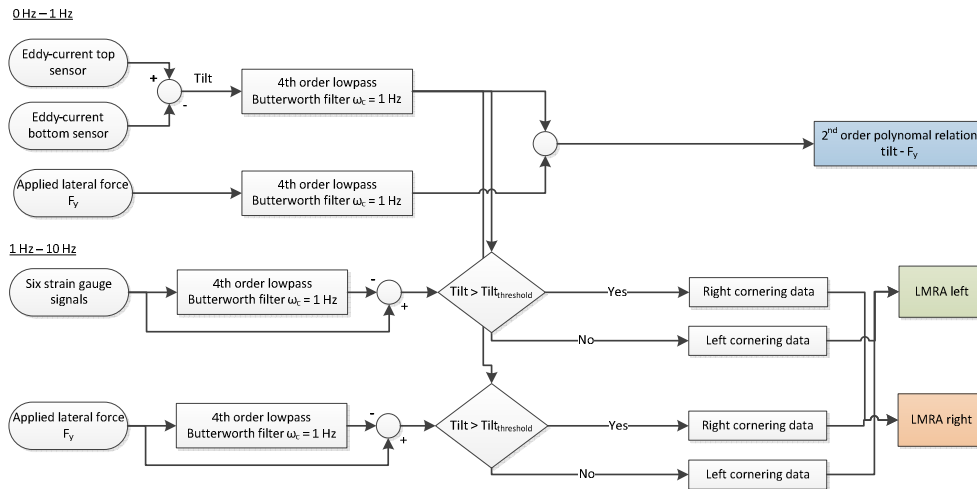


Figure 94 Block diagram method 1

Calibration



Estimation

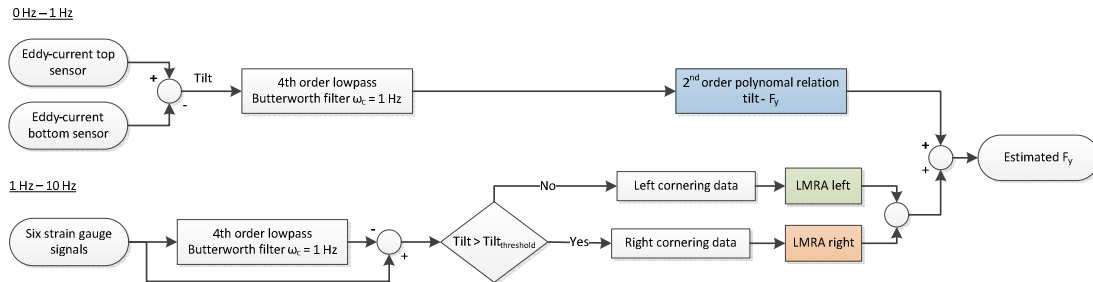


Figure 95 Block diagram method 2

The signals are thus again divided into two frequency bands. One lower frequency band in the range from 0 Hz to 1 Hz and the higher frequency band in the range from 1 Hz to 10 Hz as shown in Figure 96.

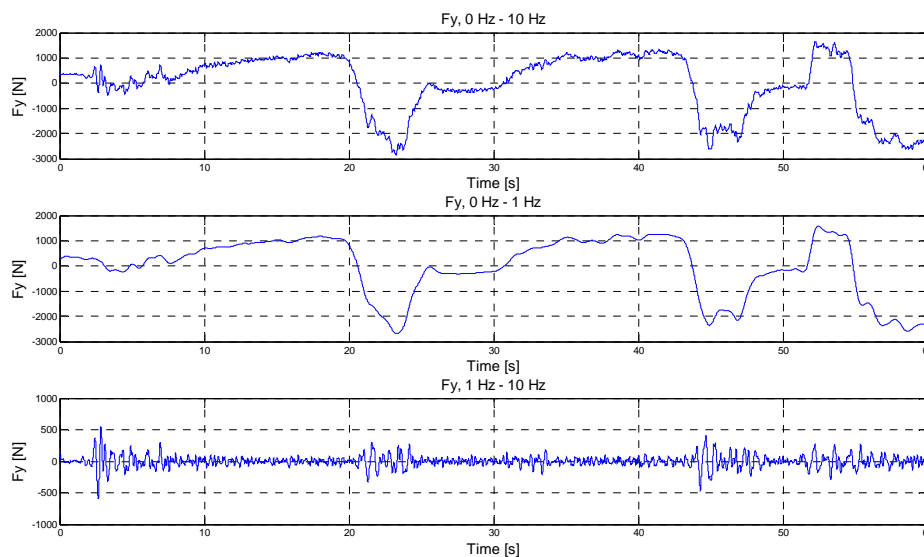


Figure 96 Frequency separation. Upper plot: Total signal. Middle plot: Signal content in the range from 0 Hz to 1 Hz. Lower plot: Signal content in the range from 1 Hz to 10 Hz.

For the estimations using the in-situ calibration all six strain gauges have been used, because it is shown in section 3.5 that there is no necessity of disregarding strain gauges from the MLRAs. However, for the estimations using the BETSY calibration three from the six available strain gauges are disregarded from the MLRA. First, strain gauge 2 is disregarded because this signal had been lost during the BETSY measurements. Strain gauge 4 and 6 have also been disregarded, because, for positive F_y , strain gauge 4 and 6 do not show response for the field measurements. It turned out that including one of these strain gauges in the MLRAs would completely ruin the lateral force estimation.

For the estimation using the tilt of the LSB both second and sixth order polynomials are used for the in-situ- and the BETSY calibration.

5.9.1 In situ calibration

Figure 97 shows the measured and estimated forces versus time. The measured force is shown in blue. The green line represents the estimation where the low frequent part is estimated by the tilt and the high frequent with two MLRAs. The red line represents the estimation where for both the low- and high frequent content two MLRAs are used.

Figure 98 shows the measured force versus the estimated force. The blue line represents the ideal line for which the estimated force is exactly equal to the measured force. The green and red lines are as in Figure 97. The error distributions are shown in Table 40 and Figure 99.

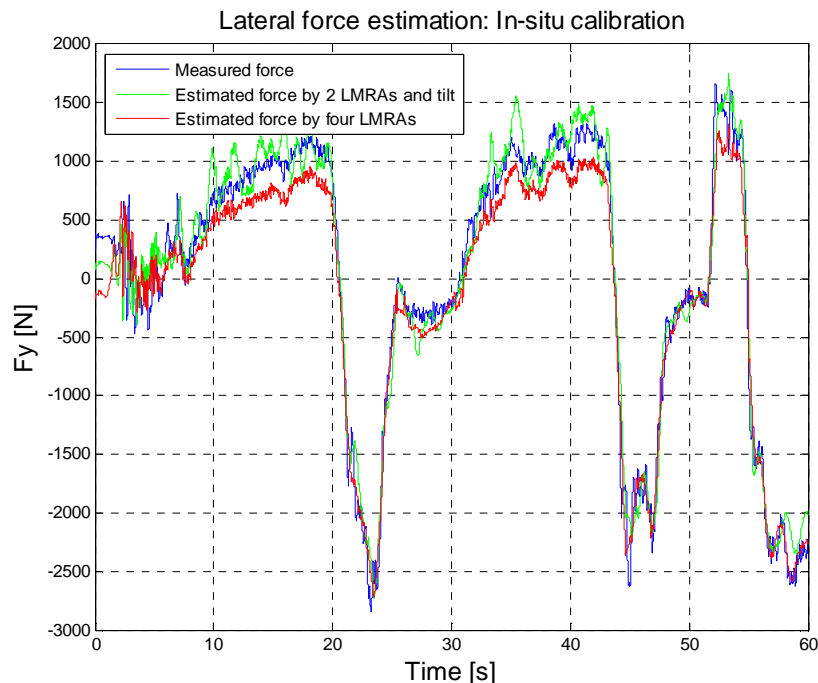


Figure 97 Measured and estimated lateral force

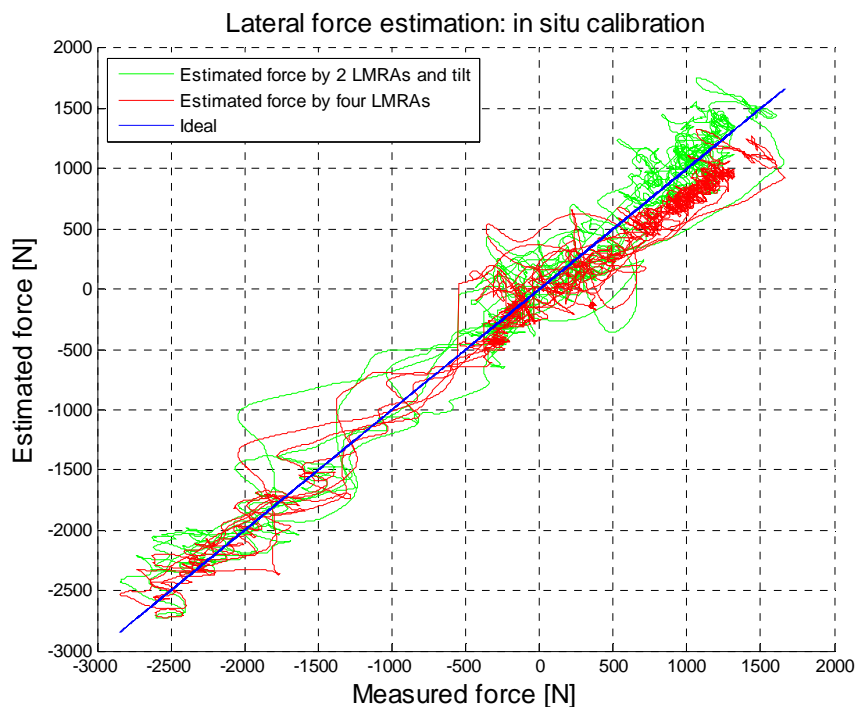


Figure 98 Measured force versus the estimated force

For the estimation using four LMRAs, the estimated positive lateral force is underestimated. This can be explained by the temperature induced strain in the LSB. The used validation test was the second test in a row of five 60-second-tests. The temperature and the temperature induced strain are therefore lower than the temperature and the temperature induced strain in the largest amount of data. This assumption is tested by ‘manually’ increasing the strain for positive lateral force with 1 microstrain. This manual increase resulted in a closer approximation and therefore it can be said that this underestimation is a consequence of the temperature. Another interesting thing to note here is that by manually changing the strain the temperature dependence can be tested. It turned out that the sensitivity of right cornering maneuvers for which F_y is smaller than zero the sensitivity was many times smaller in contrast to the sensitivity for left corners. With that it can be explained why only a deflection from the ideal line is observed for positive lateral force in Figure 98.

Figure 99 and Table 40 show the probability density distribution of the estimation errors and the RMS-errors, means and standard deviations in number respectively.

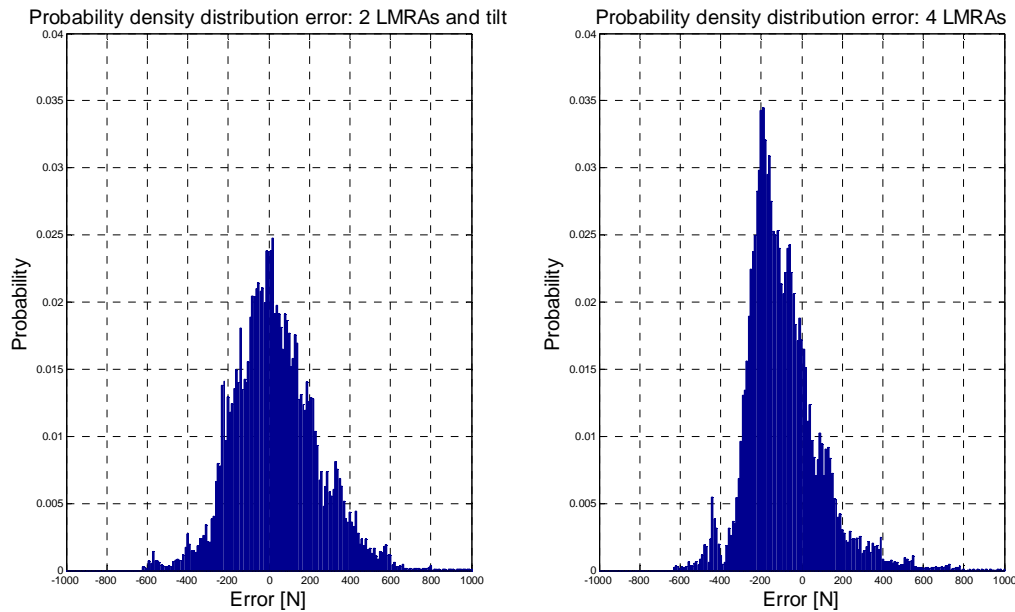


Figure 99 Probability density distribution of the estimation error. Left: estimation by 2 MLRAs and the tilt. Right: estimation by 4 MLRAs.

Table 40 RMS, mean and standard deviation of the estimation errors using an in-situ calibration

Frequency content	Method	RMS Error [N]	Mean μ [N]	Standard deviation σ [N]	Error [%]
0 Hz - 1 Hz	LMRA	188,82	-127,76	139,04	16,46
	Tilt 2nd order	229,84	31,78	227,63	20,04
	Tilt 6th order	174,47	31,22	171,65	15,21
1 Hz - 10 Hz	LMRA	130,89	-0,92	130,89	141,82
0 Hz - 10 Hz	Tilt + LMRA	216,82	30,29	214,70	18,78
0 Hz - 10 Hz	LMRA	232,00	-128,68	193,04	20,09

For the estimation incorporating the tilt a RMS error of 216.82 N is observed whereas for the estimation only using the strain gauges an error of 232.00 N is observed. Also included in the table is the low frequent force estimation using a second order relation between F_y and tilt.

5.9.2 BETSY calibration

This section shows the results of the force estimation using a BETSY calibration. The first step in the process is transforming the measured strain in the vehicle to the strain which would be measured on BETSY when it is loaded with the same F_y . To recapitulate, this step is necessary in order to use the calibration matrices which are obtained using the BETSY experiments, for the force estimations in the vehicle. Figure 100 shows the first order approximations for the F_y – strain curves obtained using BETSY in green, measured in the vehicle in blue and the transposed strain in red. The proposed method is successful. The green lines coincide with the red lines which indicate that the measured strain in the vehicle has successfully been transformed to the strain which would have been measured on BETSY while loaded with the same F_y . Some minor differences in

offset en slope are present. These small differences are assigned to be a result of the reproducibility. Whereas the transformation coefficients are based on several tests which contain a certain spread, the shown graphs are based on one single test.

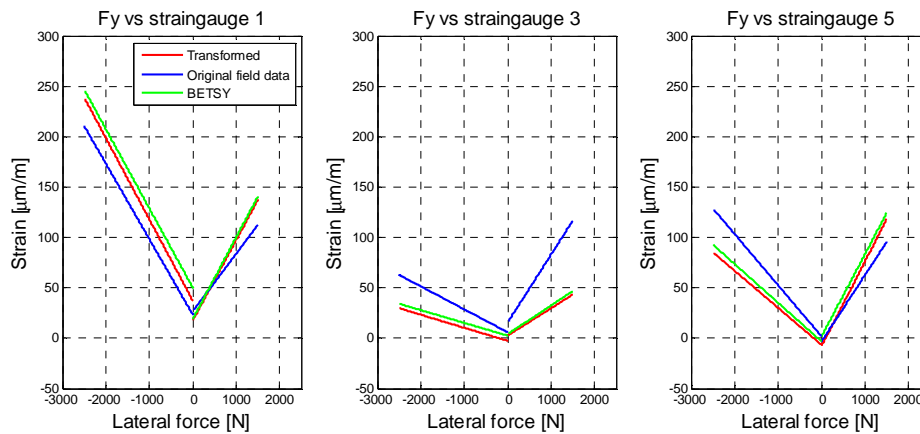


Figure 100 Transformation of the strain measured in the vehicle

In Figure 101 the estimation results using BETSY as calibration system are shown. The F_y – tilt relation found on BETSY is directly used for the estimation as explained in section 5.7.

Figure 101 shows the measured and estimated forces versus time. The measured force is again shown in blue. The green line represents the estimation where the low frequent part is estimated by the tilt and the high frequent with two MLRAs. The red line represents the estimation where for both the low- and high frequent content two MLRAs are used.

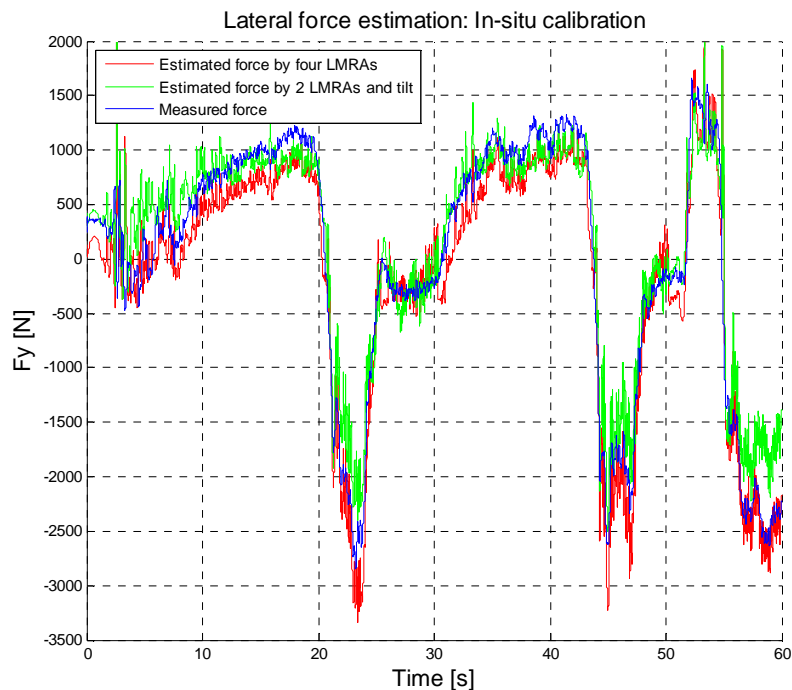


Figure 101 Lateral force estimation using BETSY calibration

Figure 102 shows the measured force versus the estimated force. The blue line represents again the ideal line for which the estimated force is exactly equal to the measured force. The error distributions are shown in Figure 103.

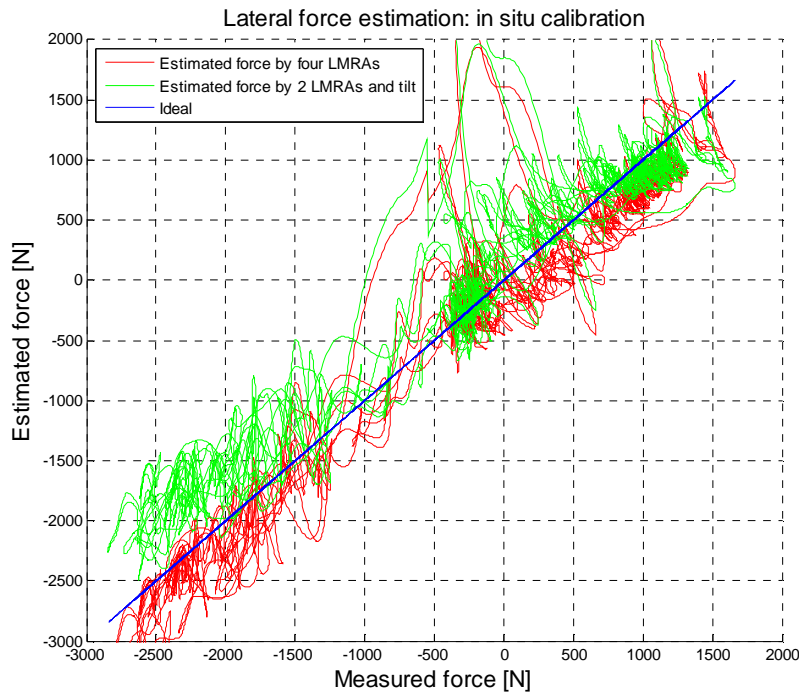


Figure 102 Measured force versus the estimated force

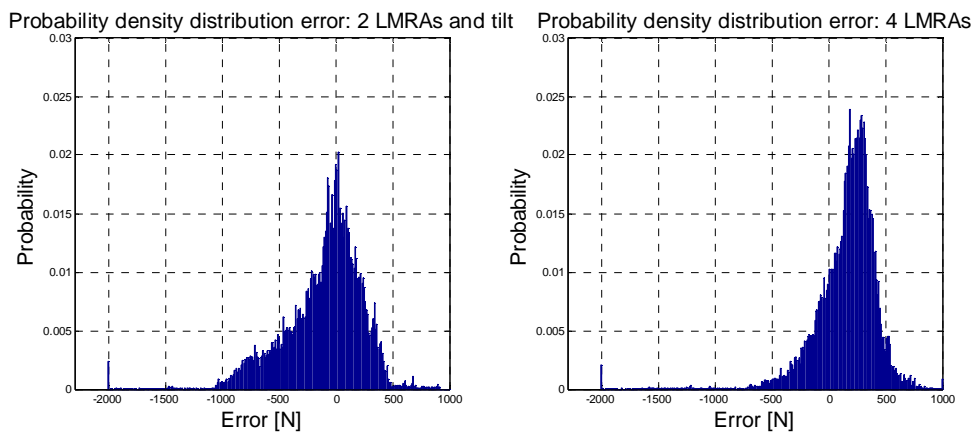


Figure 103 Probability density distribution of the estimation error. Left: estimation by 2 MLRAs and the tilt. Right: estimation by 4 MLRAs.

The RMS-error obtained by the low frequent estimation using the second order tilt is 261.2 N. The mean of the error is equal to -121.2 N and the standard deviation is 231.4 N. A sixth order relation would result in a RMS-error of 342.6 N, a mean of -162.9 N and a standard deviation of 301.4 N. Table 41 gives an overview of the RMS-error, mean μ , standard deviation σ and the error in percent. The errors are larger when compared to the in-situ calibration.

The larger errors for the estimations including the tilt are expected because the used F_y - tilt relation found on BETSY deviates from the F_y - tilt relation found in the vehicle as is

shown in Figure 89 in section 5.7. In this figure, especially the larger negative F_y shows deviation. This is perfectly reflected by Figure 102 where the green line deviates the most from the blue line for the larger negative F_y .

The larger errors for the low frequent force estimation using the LMRAs can be explained by the extra strain transformation step in the process; an additional step will introduce an additional error source.

Table 41 RMS, mean and standard deviation of the estimation errors using a BETSY calibration

Frequency content	Method	RMS Error [N]	Mean μ [N]	Standard deviation σ [N]	Error [%]
0 Hz - 1 Hz	LMRA	191,44	142,32	128,04	16,69
	Tilt 2nd order	261,23	-121,24	231,40	22,78
	Tilt 6th order	342,64	-162,93	301,43	29,88
1 Hz - 10 Hz	LMRA	265,34	12,40	265,05	287,49
0 Hz - 10 Hz	Tilt + LMRA	374,55	-108,84	358,40	32,44
0 Hz - 10 Hz	LMRA	335,29	154,73	297,46	29,04

6 Conclusions

The thesis aimed at the estimation of the lateral force acting the tire contact patch of the wheels of a vehicle using strain gauges and Eddy-current sensors.

In Chapter 3, based on BETSY measurements from 2011, a LMRA is performed on the strain gauges to estimate the lateral force. An estimation error of 8.85% had been obtained.

To improve the accuracy of the estimation, the lateral force is, in section 3.2, divided into two segments. One for the positive lateral force and one for the negative lateral force. For both the positive- and negative F_y a LMRA is performed. This reduced the error to 5,58%. To further improve the accuracy, the two segments of the lateral force have been, in section 3.3, divided into a low frequent semi-static bandwidth from 0 Hz to 1 Hz and into a higher frequent dynamic bandwidth from 1 Hz to 10 Hz, to obtain a force estimation in four quadrants:

- Bandwidth 0 Hz – 1 Hz, positive lateral force
- Bandwidth 0 Hz – 1 Hz, negative lateral force
- Bandwidth 1 Hz – 10 Hz, positive lateral force
- Bandwidth 1 Hz – 10 Hz, negative lateral force

The obtained estimation error was 6.67%. Although this is a decrease in accuracy with respect to the estimation by two segments (5.58%), the lower frequent content was estimated with an error of 4.31%, which is an increase with respect to the 5.58%.

It is shown that in the higher frequent bandwidth the strain gauges are uncorrelated with the lateral force, and therefore contaminate the LMRAs which include the dynamic content.

Section 3.4 has shown that a second order is the best option for the LMRA.

It is shown in section 3.5 that no significant improvement has been obtained and there is thus no necessity of disregarding strain gauges which show a lower correlation coefficient from the LMRA.

In Chapter 4 the Eddy-current sensors have been introduced. It is shown that F_y and the tilting movement of the ABS-ring are finely related and that this tilting movement can be used to estimate the low frequent content of F_y . Using the BETSY experiments from 2011 an estimation error, in the bandwidth 0 Hz to 1 Hz, of 10.8% is obtained. Like the strain gauges, the Eddy-current sensors show little correlation with F_y ($R_{xy} \approx 0.1$) in the dynamic frequency range and can therefore not be used for force estimation in that range. The obtained error has two main causes. The first originates from the ‘low value algorithm’ from section 4.2 which introduces a certain spread on the tilt, which in turn introduced a certain spread on the estimated force. The second is the rubber seal in which the ABS-ring is contained. The stiffness of the rubber seal changes with changing temperature. A change in stiffness implies a change in tilt and therefore a certain spread is present on the measured tilt and estimated force.

In Chapter 5 a LSB including a knuckle with Eddy-current sensors is mounted into the test vehicle, the BMW E60. Before it is mounted in the vehicle, the LSB is installed on

BETSY and tests are performed. Followed by the tests on BETSY, tests have been performed with the actual vehicle on the test track at SKF Engineering & Research Centre, Nieuwegein. Lateral force estimations, using the strain gauges and the Eddy-current sensors, are performed using an in-situ- and a BETSY calibration. The estimations are performed for both the semi-static- and the dynamic content of the lateral force F_y . Below, the obtained estimation errors are summarized

0 Hz – 1 Hz, estimation by the tilting movement, in-situ calibration

Eddy-current sensors can estimate the lateral force within the bandwidth 0 Hz to 1 Hz with an error of 174.5 N (15.2%) for a sixth order polynomial and an error of 229.8 N (20.04%) with a second order polynomial using an in-situ calibration.

0 Hz – 1 Hz, estimation by the tilting movement, BETSY calibration

Eddy-currents can estimate the lateral force within the bandwidth 0 Hz to 1 Hz with an error of 342.6 N (29.9%) for a sixth order polynomial and an error of 261.2 N (22.8%) with a second order polynomial using a BETSY calibration.

1 Hz – 10 Hz, estimation by the tilting movement

Because of the bad correlation between the lateral force F_y and the Eddy-current sensors, the Eddy-current sensors cannot be used for the estimation of the lateral force within the dynamic bandwidth of 1 Hz to 10 Hz.

0 Hz – 1 Hz, estimation using the strain gauges, in-situ calibration

Strain gauges can be used to determine the lateral force within the bandwidth 0 Hz to 1 Hz, taking temperature influences for granted, with a RMS-error of 188.8 N (16.5%) using an in-situ calibration. When the Eddy-current sensors are used for the low frequent force estimation, the strain gauges are redundant.

0 Hz – 1 Hz, estimation using the strain gauges, BETSY calibration

When a BETSY calibration is used for the estimation of F_y , Eddy-current sensors have to be used to determine the direction of the cornering maneuvers. A RMS-error of 191.4 N (16.7%) is obtained.

1 Hz – 10 Hz, estimation using the strain gauges

Strain gauges are not suitable for the determination of the lateral force within the bandwidth 1 Hz – 10 Hz. Within in this bandwidth the strain gauges and the lateral force are uncorrelated.

BETSY as calibration system

It was shown in previous research that the strain gauge responses are greatly influenced by the compliant bearing environment. Several set-ups with an environment with varying compliance had been tested and resulted in sensor responses which were not even close to what was measured in an actual vehicle. In the current set-up the LSB is mounted to BETSY by a knuckle/ball joint combination. It is shown that for this set-up the strain gauge responses on BETSY and in the vehicle are in the same order of magnitude. This opened the door for using BETSY as calibration system

Still some differences are present. Therefore, in Chapter 2, a method is derived to overcome these differences in sensitivity and offset. By describing the found $F_y - \epsilon$ relations by first order polynomials, the strain measured in the vehicle can be transformed to the strain which would be measured on BETSY under the influence of the same lateral force. Then calibration matrices found using BETSY can be used within the vehicle.

When for a certain LSB experiments are performed both on BETSY as well as an actual vehicle, this transformation can be performed accurately. This is confirmed in Chapter 5 by the almost identical results in force estimation in the bandwidth from 0 Hz to 1 Hz for the BETSY- and the in-situ calibration.

However, the goal is to use BETSY for the calibration of a whole production line. Then only one test on BETSY should be sufficient to calibrate the whole production line and no expensive field measurements are necessary. For that the experiments on BETSY and in the vehicle should be reproducible. The reproducibility had been looked at in section 5.8. Although the reproducibility results were promising, in Chapter 2 and Chapter 5 the strain transformation coefficients had been calculated for two different set of measurements and turned out to be different, which indicates that the reproducibility of the measurements is not good enough and thus is BETSY not usable as calibration system regarding the strain gauges.

The Eddy-current sensors have also been tested on BETSY and in the vehicle. The relations between the tilt and F_y were very similar. Using a second order polynomial relation, the estimation results using a BETSY and in-situ calibration differed only 2.8%, from 20.0% to 22.8%.

For a sixth order the difference was larger. From an in-situ calibration to a BETSY calibration the error increased from 15.2% to 29.9%.

Based on the performed experiments it can be concluded, regarding the Eddy-current sensors, that it is possible to use BETSY for calibration. However, the Eddy-current sensors have only been tested once within an actual vehicle and one should be careful about this drawn conclusion. Further experiments are necessary.

7 Recommendations

- In Chapter 6, the conclusion is drawn that BETSY is an appropriate calibration system regarding the Eddy-current sensors. Thus far, the Eddy-current sensors have only been tested once in a vehicle and one should be aware of the fact that the drawn conclusion is only valid for the particular used test vehicle. Tests in more vehicles are necessary to make the statement more valid.
- In the vehicle, an estimation error in the order of 20% is obtained using the Eddy-current sensors. This rather large error finds its origin in the 'low value algorithm' and in the rubber sealing which contains the ABS-ring. If an opportunity is created to remove both of these causes, it is expected that the accuracy of the estimation can significantly be improved. This opportunity can be created by inserting an extra unpatterned ring next to the ABS-ring. If this ring does not contain holes like the ABS-ring there is no need of a 'low value algorithm' and if the ring is not confined within the rubber sealing, both sources of error are removed.
- Experiments on BETSY have shown that the signals from the strain gauges do not correlate with the lateral force F_y in the dynamic bandwidth. Because in the experiments in the field the LSB is excited with only a small amount of dynamic F_y , it is advised to perform tests which excite the vehicle with a higher amount of high frequent F_y . Then more reasonable judgments can be made regarding the dynamic content of the strain gauges and lateral force in the vehicle.
- For future work it is advised to set the strain signals in the vehicle to zero by adjusting the conditioner boxes. This will take away the necessity of the offset compensation.
- The thesis aimed at the estimation of the lateral force, but the LSB creates also great opportunities for the estimation of the longitudinal- and vertical force. More research is necessary to investigate the possibilities of the LSB regarding the longitudinal- and vertical force.
- The thesis conclusions are based on the post processing of the measurements. A logical next would be to implement the estimation algorithm in the vehicle and perform tests, estimating the lateral force real time while driving.

8 Appendices

8.1 Appendix A

8.1.1 Overview measured variables Papenburg

Channel	Source	Variable	Channel	Source	Variable	Channel	Variable
1	LSfrontleft	Strain 1	41		My	81	Pfl
2		Strain 2	42		Mz	82	Pfr
3		Strain 3	43	MTSrearleft	Fx	83	Pitchangle
4		Strain 4	44		Fy	84	Pitchrate
5		Strain 5	45		Fz	85	Prl
6		Strain 6	46		MTSangle	86	Prr
7		temp	47		Mx	87	Rollangle
8	LSfrontright	Strain 1	48		My	88	Rollrate
9		Strain 2	49		Mz	89	Trigger
10		Strain 3	50	MTSrearright	Fx	90	Vx_corrsys
11		Strain 4	51		Fy	91	Vx_corrsys_middle
12		Strain 5	52		Fz	92	Vxdsc
13		Strain 6	53		MTSangle	93	Vx_newcorrsys
14		temp	54		Mx	94	Vx_newcorrsys_middle
15	LSrearleft	Strain 1	55		My	95	Vy_corrsys
16		Strain 2	56		Mz	96	Vy_corrsys_rearaxle
17		Strain 3	57		Angle_newcorrsys	97	Vy_newcorrsys
18		Strain 4	58		Ax_body_fl	98	Vy_newcorrsys_rearaxle
19		Strain 5	59		Ax_body_fr	99	Yaw_dsc
20		Strain 6	60		Ax_body_rl	100	Yawrate_boschL
21		temp	61		Ax_body_rr	101	Yawrate_boschR
22	LSrearright	Strain 1	62		Ax_dsc	102	clutch
23		Strain 2	63		Ay_body_fl	103	delta_afs
24		Strain 3	64		Ay_body_fr	104	delta_steer
25		Strain 4	65		Ay_body_rl	105	delta_summen
26		Strain 5	66		Ay_body_rr	106	delta_wheel
27		Strain 6	67		Ay_boschL	107	enginertorque
28		temp	68		Ay_boschR	108	gear
29	MTSfrontleft	Fx	69		Ay_dsc	109	throttle
30		Fy	70		Az_body_fl	110	w_fl
31		Fz	71		Az_body_fr	111	w_fr
32		MTSangle	72		Az_body_rl	112	w_rl
33		Mx	73		Az_body_rr	113	w_rr
34		My	74		Az_wheel_fl	114	zfl
35		Mz	75		Az_wheel_fr	115	zfr
36	MTSfrontright	Fx	76		Az_wheel_rl	116	zrl
37		Fy	77		Az_wheel_rr	117	zrr
38		Fz	78		Ddelta_afs		
39		MTSangle	79		Delta_steer		
40		Mx	80		Distance_newcorrsys		

8.2 Appendix B

8.2.1 Papenburg vehicle specifications

Vehicle specifications:

- Engine: 4.4 L, 333 bhp
- Tyres: 225/50 ZR17 with 17 inch rims
- Wheel base: 2.888 m
- Track base front & rear: 1.558 m & 1.582 m
- Vehicle weight: 1721 kg empty, estimated during tests 2000 kg (3 people + equipment)

8.3 Appendix C

8.3.1 Frequency analysis: Papenburg

To get a good understanding of the signals, the frequency spectra are calculated. In this section, first the frequency spectra will be shown. Afterwards the observed frequency peaks will be discussed.

Below, in Figure 104, the frequency spectra of the six strain signals are shown. The frequency spectrum is shown on the frequency range 0 Hz – 20 Hz.

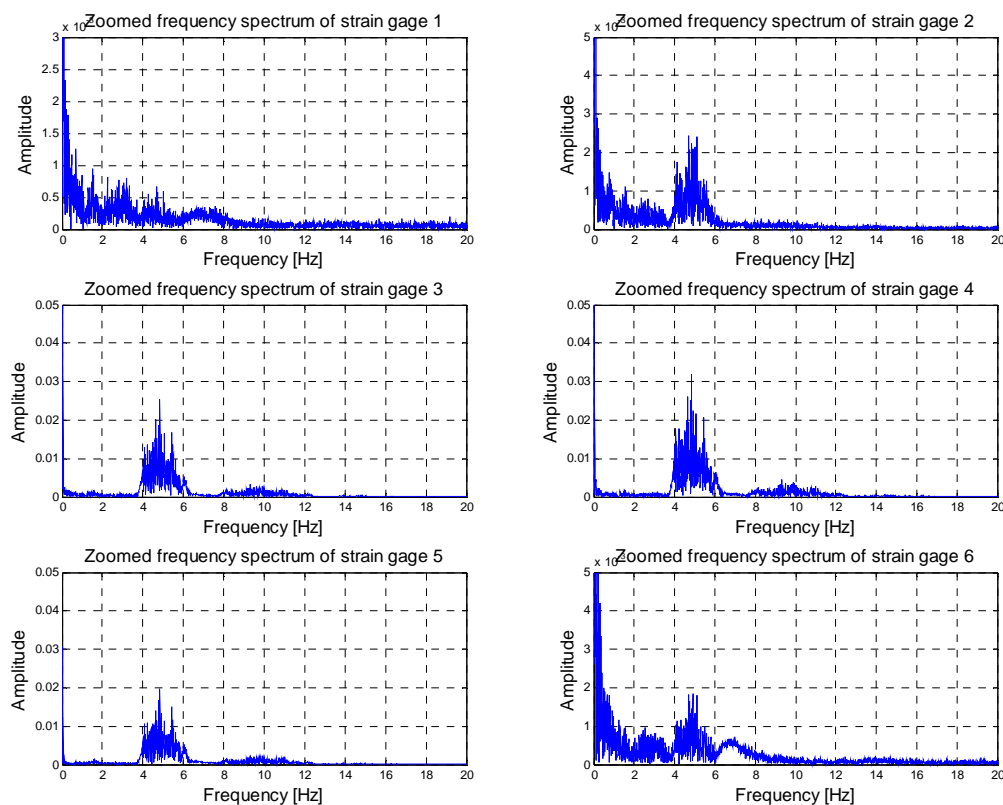


Figure 104 Frequency spectrum of the strain signals

Most of the energy in the input signals is concentrated within the lower frequency band, 0 Hz – 5 Hz. Peaks are seen at 0 Hz, 0.044 Hz, 1.5 Hz, 4.85 Hz and a small peak at 1.5 Hz.

Next, in Figure 105, the frequency spectra of the loads are shown. Again, the frequency spectrum is shown for the frequency band 0 Hz – 20 Hz.

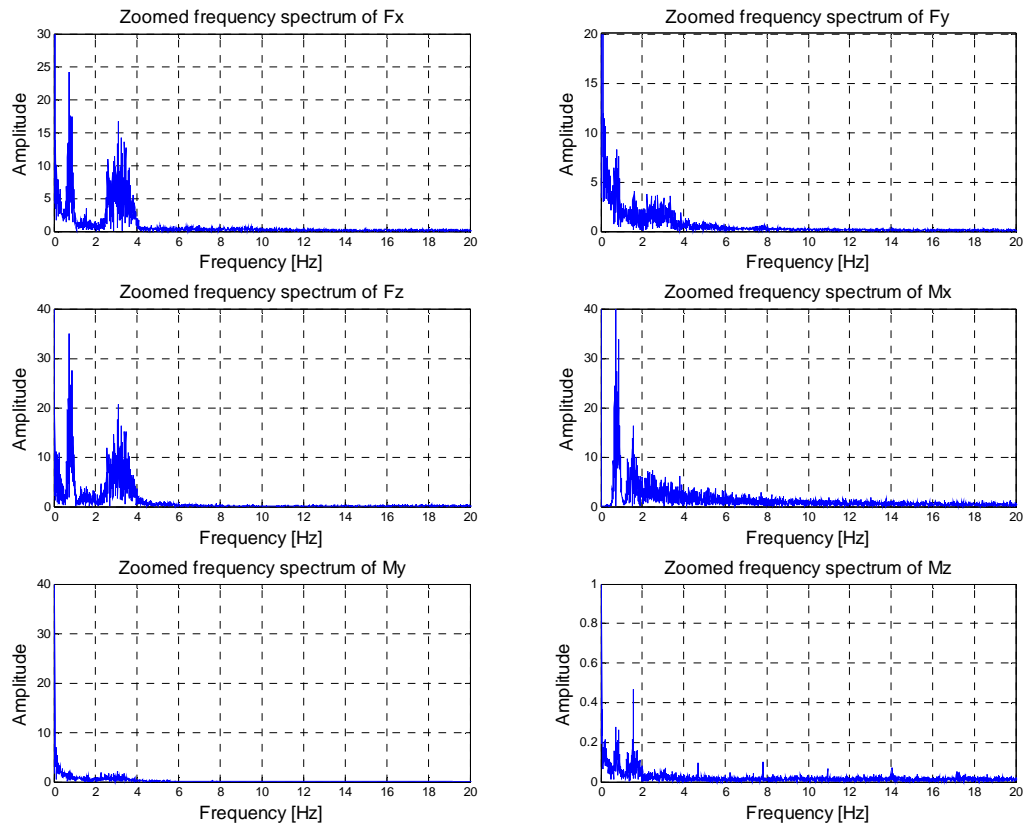


Figure 105 Frequency spectrum of the output signals

Most of the energy is again concentrated within the lower frequency band, 0 Hz – 5 Hz. Peaks are seen at 0 Hz, 0.044 Hz, 0.74 Hz, a small peak at 1.5 Hz and a peak around 3 Hz.

Not all loads show the same frequency content, see Table 42. In the next section it will become clear where these differences come from.

Table 42 Frequency content per load

Load	Frequency peaks Hz				
	0	0.044	0.74	1.5	3
Fx	x	x	x	x	x
Fy	x	x	x		
Fz	x	x	x	x	x
Mx	x		x	x	
My	x	x			
Mz	x	x	x	x	

8.3.2 Comparison

Expected frequencies peaks

The first frequency peak we expect to see is a peak at 0 Hz. This peak is caused by the DC-offsets present in the signals. Another frequency peak should arise at the frequency of the turning movements of the slalom.

Frequencies peaks which are also expected to see are the angular frequency of the wheel or frequencies which are multiples of the angular frequency of the wheel. These can be caused by, for example, an unbalance in the wheel. A peak is also expected at the so called ‘ball pass frequency’. Every time one of the balls in the bearing passes a strain gauges it locally deforms the strain gauge. This local deformation should be seen in the measured signals. These local deformations can only be sensed by the strain gauges on the bearing and not by the MTS wheel.

In Table 43 the observed frequency peaks are summarized.

Table 43 Frequency content of the strain and measuring wheel signals

	Frequency peaks strain Hz	Frequency peaks measuring wheel Hz
First frequency peak	0	0
Second frequency peak	0.044	0.044
Third frequency peak	1.5	0.74
Fourth frequency peak	2.8	1.6
Fifth frequency peak	4.85	3

DC-offset

All the strain and load signals contain energy at 0 Hz. This is, as told above, due to the DC offset in the signals.

Slalom frequency

The second frequency peak is located at 0.044 Hz. This is expected because we are analyzing data from a ‘slalom’-test. In this test the complete cycle of a left turn and a right turn has period T of around $20\text{sec} < T < 25\text{sec}$ resulting in frequency of

$$0.04\text{Hz} < f = \frac{1}{T} < 0.05\text{Hz}.$$

Angular frequency of the wheel

The angular frequency of the wheel can be calculated by $\omega_{wheel} = \frac{V_{wheel}}{r_{wheel}}$. Where V_{wheel} is the velocity of the wheel and r_{wheel} is the radius of the wheel; 0.3285 m.

The angular frequency of the wheel can be calculated. The average velocity during the test v_{avg} is measured to be 1.55 m/s.

$$\omega_{wheel} = \frac{v_{avg}}{r_{wheel}} = \frac{1.55 \text{ m/s}}{0.328 \text{ m}} = 4.739 \text{ rad/s} = 0.7542 \text{ Hz}$$

Table 43 shows that there is a peak in the output at 0.74 Hz. This frequency is present in the signals measured with the MTS force measuring wheel but not in the signals measured by the strain gauges and is therefore caused by an offset in one of the measured channels of the measuring wheel which superimposes a signal component with the angular frequency of the wheel.

A frequency peak of 3 Hz is present in the signals of the MTS wheel is for F_x and F_z . 3 Hz is exactly four times the angular velocity of the wheel. F_x and F_z are in the radial direction of the wheel and are measured with the four radial flexmembers of the measuring wheel, which are only flexible in the radial direction, see Figure 10. These flexmembers introduce a variation in the radial stiffness along the circumference and are passed to the calculated forces.

The 1.5 Hz is two times the calculated angular frequency of the wheel. Probably also introduced by variations in radial stiffness.

Ball pass frequency

The ball pass frequency can be calculated with the help of the theory of planetary gearboxes. The relation between the angular velocities and diameters of the inner ring, outer ring and ball carrier, respectively the sun, wheel carrier and ring for a planetary gearbox is

$$D_{innerring} \omega_{innerring} + D_{outerring} \omega_{outerring} = (D_{outerring} + D_{innerring}) \omega_{ballcarrier}$$

$$\omega_{ballcarrier} = \omega_{innerring} \frac{D_{innerring}}{(D_{outerring} + D_{innerring})}, \quad (\omega_{outerring} = 0)$$

The inner ring rotates together with the wheel $\omega_{innerring} = \omega_{wheel} = \frac{V_{vehicle}}{r_{wheel}}$

The ball pass frequency is the ball carrier frequency times the number of balls in one ball row.

$$\omega_{ballpass} = N \cdot \omega_{ballcarrier}$$

Combining above equations the ball pass frequency can now be calculated by:

$$\omega_{ballpass} = \frac{N \cdot \frac{V_{vehicle}}{r_{wheel}} \cdot D_{innerring}}{(D_{outerring} + D_{innerring})}$$

With $N = 15$, $r_{wheel} = 0.3285 \text{ m}$, $\frac{D_{innerring}}{(D_{outerring} + D_{innerring})} = \frac{60}{90 + 60} = 0.4$ and with an average wheel speed of 1.55 m/s the ball pass frequency becomes:

$$\Omega_{ballpass} = 29.928 \text{ rad/s} = 4.763 \text{ Hz}$$

In the frequency spectra of Figure 104 and Figure 105 it can be observed that the peak around $\omega_{ballpass}$ is spread out over a wider frequency bandwidth. This is expected because an average value of the velocity is used. Of course during the test the velocity was varying. This frequency is not observed in the signals of the MTS wheel, because the passing balls only affect the strain gauge.

The ball pass frequency depends on the wheel speed and is thus varying with the vehicle velocity. At low velocities the ball pass frequency will be visible in the bandwidth of 0 Hz to 10 Hz and starting at $v = 3.27 \text{ m/s}$ it will fall outside this bandwidth, see Figure 106.

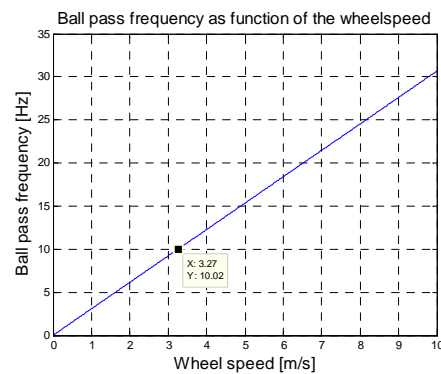


Figure 106 Ball pass frequency as a function of the wheel speed / vehicle speed

8.3.3 Frequency analysis BETSY

In this section the frequency spectra of the measured strain, lateral deflection and applied loads will be analyzed. First the spectra will be shown in three figures. One with six graphs for the strain, one with three graphs for the loads and one with two graphs for the Eddy-current sensors. Secondly an overview of all the observed frequency peaks will be given and finally an analysis of the frequency peaks is performed.

8.3.3.1 Strain

Below, in Figure 107, the frequency spectra of the strain gauges are shown. All strain gauges show the same behaviour with respect to the frequency content. In Table 5 the peaks are listed.

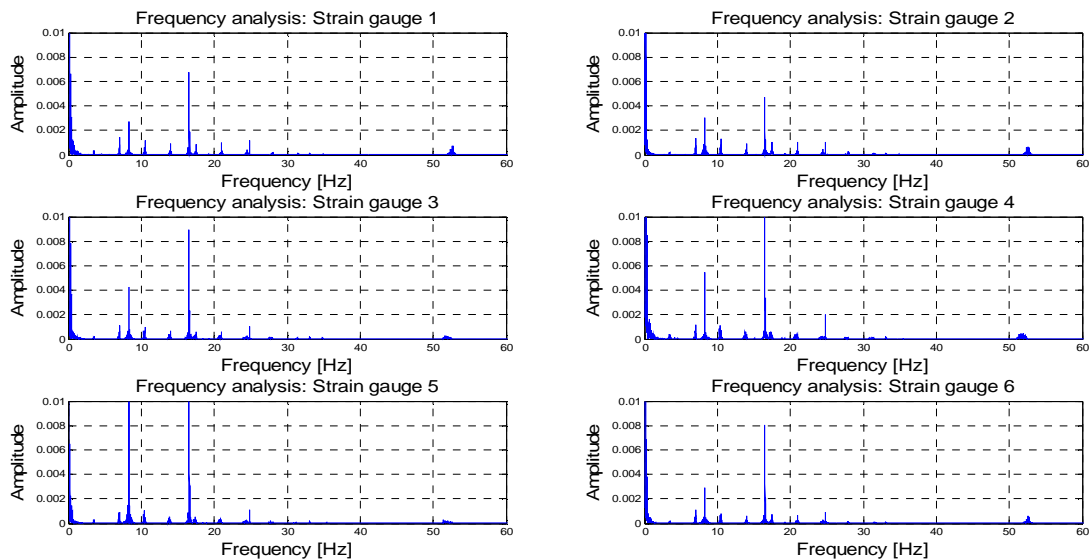


Figure 107 Frequency spectra of the strain gauges

8.3.3.2 Load

In Figure 108 the frequency spectra of the loads are shown. Expect for peaks at 3.5 Hz and 7 Hz, all the loads show the same spectra. Again, the peaks are listed in Table 44.

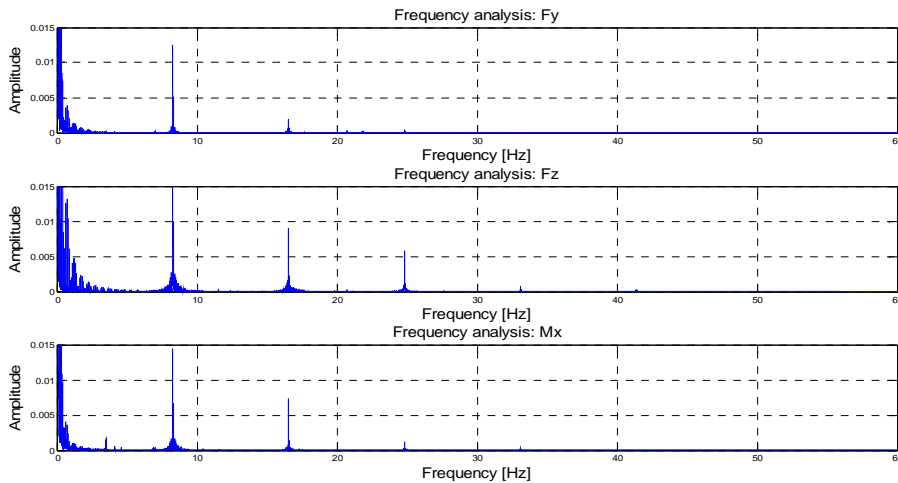


Figure 108 Frequency spectra of the applied loads

8.3.3.3 Eddy-current sensors

In Figure 109 the frequency spectra of the Eddy-current sensors are shown. Both sensors show the same spectra. Again, the peaks are listed in Table 44. Whereas the strain gauges show lots of frequency peaks which are not present within the applied loads, the Eddy-current sensors are in agreement with the applied loads.

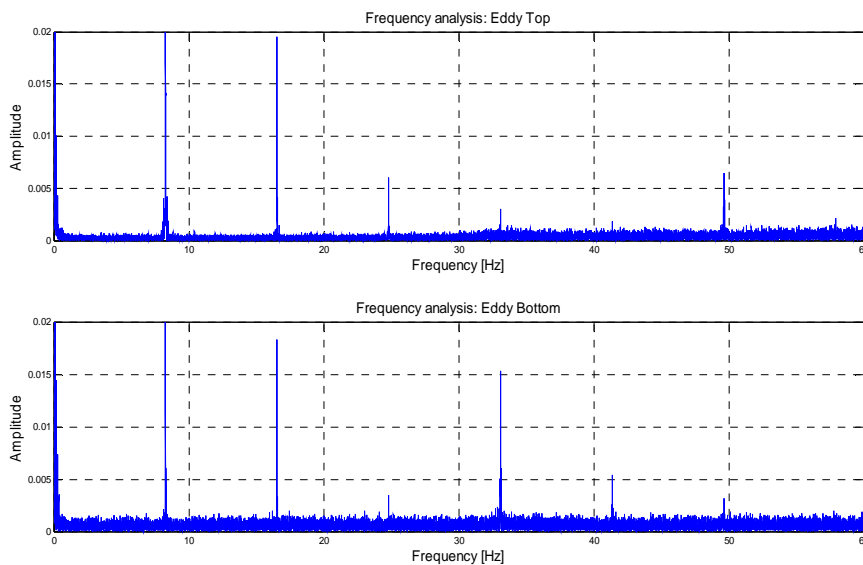


Figure 109 Frequency spectra of the Eddy-current sensors

8.3.3.4 Comparison

Below in Table 44 all the frequency peaks for all the signals are listed. As a first observation it can be noticed that the strain gauges are subject to more frequency peaks than the loads applied by BETSY. In contrast, the Eddy-current sensors show a response which is more in agreement with the applied loads.

Table 44 Frequency spectra overview

Frequency [Hz]	Strain gauge 1 -					
	6	Eddy top	Eddy bottom	F_y	F_z	M_x
0	x	x	x	x	x	x
0.12 - 0.78	x	x	x	x	x	x
3.5	x					x
7	x			x		x
8.28	x	x	x	x	x	x
10.48	x					
13.98	x					
16.55	x	x	x	x	x	x
17.46	x					
20.96	x					
24.45	x					
24.83	x	x	x	x	x	x
27.98	x					
31.47	x					
33.11	x				x	x
34.9	x					
41.38		x	x			
49.65		x	x			
52.6	x					

The zero Hz content can be assigned to the average value of the signals. Every signal has an average and therefore a peak at 0 Hz.

The peaks from 0.12 Hz. to 0.78 Hz. can be assigned to the spectral leakage introduced by the window function Hann which is applied before making the transformation from the time domain to the frequency domain.

The BETSY tests are performed at 500 rpm = 8.3 Hz. The observed frequencies 8.28 Hz., 16.55 Hz., 24.83 Hz. and 33.11 Hz. are all integer multiples of the frequency of rotation. They can be assigned to a misalignment in the inclination of the bearing on the BETSY machine. The inclination misalignment thus introduces an error source within the system bandwidth of 0 Hz – 10 Hz. To exclude this error source for the BETSY measurements performed in Chapter 5, the measurements are performed at 1000 Hz.

The fourth multiple of the rotation frequency of 8.28 Hz. is not seen in the lateral force and in the Eddy-current sensors signals. The Eddy-current sensors measure the lateral deflection and are therefore correlated with the lateral force. This explains why this

fourth multiple is not seen by the Eddy-current sensors. However, why this fourth multiple is not seen in F_y but is seen in F_z and F_x is unknown for now.

The 52.6 Hz. content in strain gauges represent the ball pass frequency.

One ball row contains 15 balls. The peaks observed for 3.5 Hz, 7 Hz, 10.48 Hz, 13.98 Hz, 17.46 Hz, 20.96 Hz, 24.45Hz, 27.28 Hz, 31.47 Hz 34.9 Hz for the strain gauges are all multiples of the 3.5 Hz; the ball pass frequency of one single ball. This indicates variations in pretension of the balls which could be caused by small differences in diameter.

The peak at 3.5 Hz. is also observed for F_y and M_x and the peak at 7 Hz is also observed for F_y . Why these two are also observed in these forces, and only these lower two multiples, is unknown for now.

Peaks at 41.38 Hz., 49.65 Hz. are observed for Eddy current sensors.

8.4 Appendix D

8.4.1 Overview of the performed field tests at SKF, Nieuwegein

Data file	Sample rate: ASVs	Duration [s]	Date of execution	Maneuver(s)
t_221012_l_10_001.mat	5	30	22-Oct-12	Test op 22 10 2012, Left turn, 10 km/h try 1
t_221012_l_10_002.mat	5	30	22-Oct-12	Test op 22 10 2012, Left turn, 10 km/h try 2
t_221012_l_20_001.mat	5	30	22-Oct-12	Test op 22 20 2012, Left turn, 10 km/h try 1
t_221012_l_20_002.mat	5	30	22-Oct-12	Test op 22 20 2012, Left turn, 10 km/h try 2
t_221012_l_30_001.mat	5	30	22-Oct-12	Test op 22 30 2012, Left turn, 10 km/h try 1
t_221012_l_30_002.mat	5	30	22-Oct-12	Test op 22 30 2012, Left turn, 10 km/h try 2
t_221012_l_102030_001.mat	5	30	22-Oct-12	Test op 22 30 2012, Left turn increasing velocity: 10, 20 and 30 km/h try 1
t_221012_l_102030_002.mat	5	30	22-Oct-12	Test op 22 30 2012, Left turn increasing velocity: 10, 20 and 30 km/h try 2
t_221012_r_10_001.mat	5	30	22-Oct-12	Test op 22 10 2012, Right turn, 10 km/h try 1
t_221012_r_10_002.mat	5	30	22-Oct-12	Test op 22 10 2012, Right turn, 10 km/h try 2
t_221012_r_20_001.mat	5	30	22-Oct-12	Test op 22 20 2012, Right turn, 10 km/h try 1
t_221012_r_20_002.mat	5	30	22-Oct-12	Test op 22 20 2012, Right turn, 10 km/h try 2
t_221012_r_30_001.mat	5	30	22-Oct-12	Test op 22 30 2012, Right turn, 10 km/h try 1
t_221012_r_30_002.mat	5	30	22-Oct-12	Test op 22 30 2012, Right turn, 10 km/h try 2
t_221012_r_102030_001.mat	5	30	22-Oct-12	Test op 22 30 2012, Right turn increasing velocity: 10, 20 and 30 km/h try 1
t_221012_r_102030_002.mat	5	30	22-Oct-12	Test op 22 30 2012, Right turn increasing velocity: 10, 20 and 30 km/h try 2
T_221012_Reference001.mat	5	30	22-Oct-12	Driving a straight reference run
t_221012_total_001.mat	5	60	22-Oct-12	Driving for 60 sec. over the test track making turns left and right at different speeds
t_221012_total_002.mat	5	60	22-Oct-12	Driving for 60 sec. over the test track making turns left and right at different speeds
t_221012_total_003.mat	5	60	22-Oct-12	Driving for 60 sec. over the test track making turns left and right at different speeds
t_221012_total_004.mat	5	60	22-Oct-12	Driving for 60 sec. over the test track making turns left and right at different speeds
t_221012_total_005.mat	5	60	22-Oct-12	Driving for 60 sec. over the test track making turns left and right at different speeds
Test_001.mat	5	10	22-Oct-12	Test to see if all the sensors are working
test_19_10_12_endtest.mat	5	10	19-Oct-12	Test to see whether all sensors are still working
test_19_10_12_jinksom_102030_001.mat	5	60	19-Oct-12	Driving a left turn to the left in increasing steps 10, 20 and 30 km/h
test_19_10_12_rechtsom_102030_001.mat	5	60	19-Oct-12	Driving a right turn to the right in increasing steps 10, 20 and 30 km/h
test_19_10_12_rechtsom_rechtuit_10_001.mat	5	40	19-Oct-12	Drive starts at corner right, driving straight at 10 km/h
test_19_10_12_rechtsom_rechtuit_10_002.mat	5	60	19-Oct-12	Drive starts at corner right, driving straight at 10 km/h
test_19_10_12_rechtsom_rechtuit_20_001.mat	5	60	19-Oct-12	Drive starts at corner right, driving straight at 20 km/h
test_19_10_12_rechtsom_rechtuit_30_001.mat	5	60	19-Oct-12	Drive starts at corner right, driving straight at 30 km/h
test_19_10_12_test_001.mat	5	10	19-Oct-12	Test to see if all the sensors are working
test_19_10_12_test_002.mat	5	10	19-Oct-12	Test to see if all the sensors are working
test_19_10_12_test_003.mat	5	10	19-Oct-12	Test to see if all the sensors are working
test_19_10_12_total_track_10.mat	5	60	19-Oct-12	Driving left and right random over the test track
test_03_10_12_driving_back_to_Catlab001.mat*	0.5	30	03-Oct-12	Driving from the test track back to the catlab
test_03_10_12_left_corner_20kmpmat	0.5	30	03-Oct-12	Taking a left corner at 20 km/h
test_03_10_12_left_corner_40kmpmat*	0.5	30	03-Oct-12	Taking a left corner at 30(0) km/h
test_03_10_12_Reference_straight.mat*	0.5	30	03-Oct-12	Driving a straight reference run
test_03_10_12_right_corner_20km.mat*	0.5	30	03-Oct-12	Taking a right corner at 20 km/h
test_03_10_12_right_corner_30km.mat*	0.5	30	03-Oct-12	Taking a right corner at 30 km/h
test_05_10_001.mat*	0.5	60	05-Oct-12	Test to see if a higher sample frequency works
test_05_10_002.mat*	0.5	60	05-Oct-12	Test to see if a higher sample frequency works
test_05_10_003.mat*	0.5	60	05-Oct-12	Test to see if a higher sample frequency works

Figure 110 Overview of the performed field tests at the test track of SKF Nieuwegein

8.5 Appendix E

8.5.1 F_y vs. bottom- and top deflection

Deflection bottom sensor versus lateral force

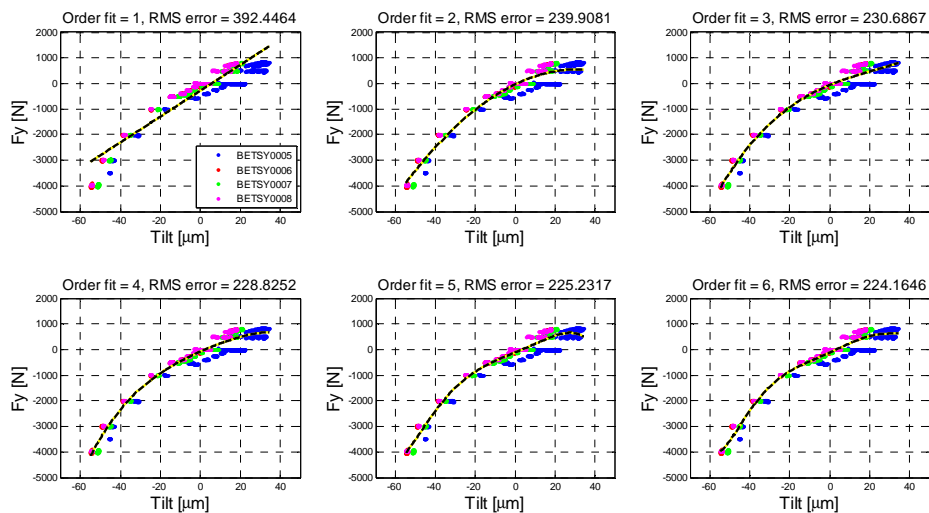


Figure 111 Deflection bottom sensor versus lateral force F_y including polynomial fits for BETSY BMW+0005 – BMW+0008

Deflection top sensor versus lateral force

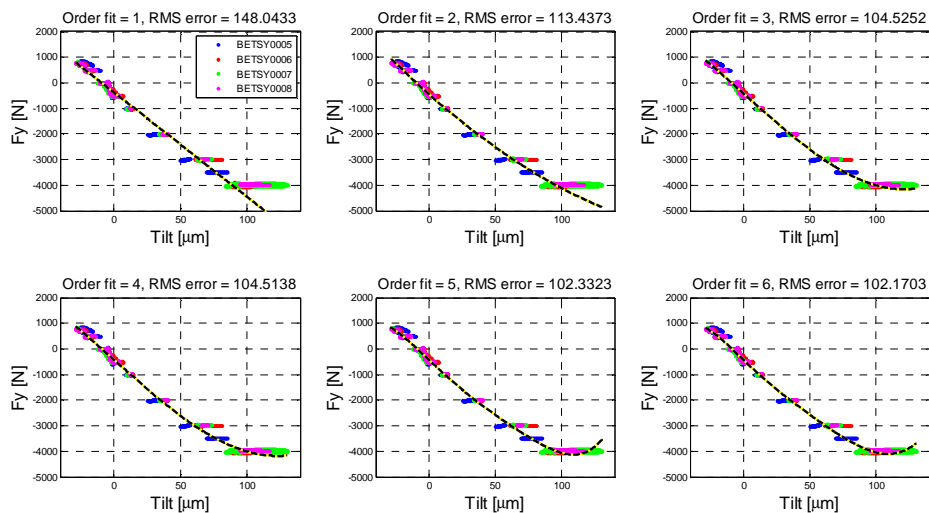


Figure 112 Deflection top sensor versus lateral force F_y including polynomial fits for BETSY BMW+0005 – BMW+0008

Deflection bottom sensor versus lateral force

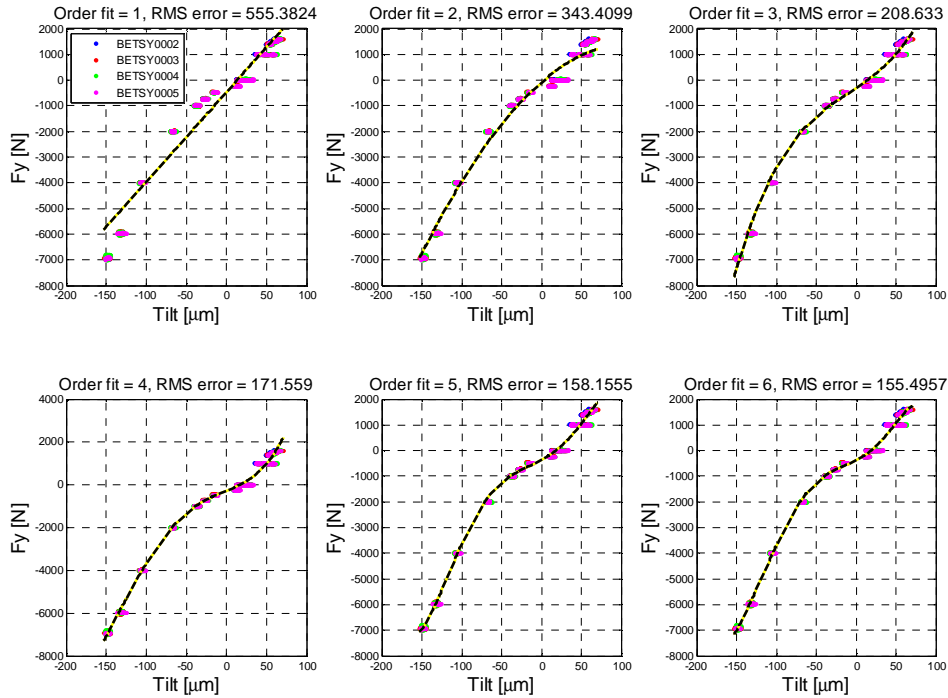


Figure 113 BETSY measurements: deflection bottom sensor versus lateral force approximated by n-th order polynomials for the BETSY test performed on the bearing which is mounted in the BMW E60

Deflection top sensor versus lateral force

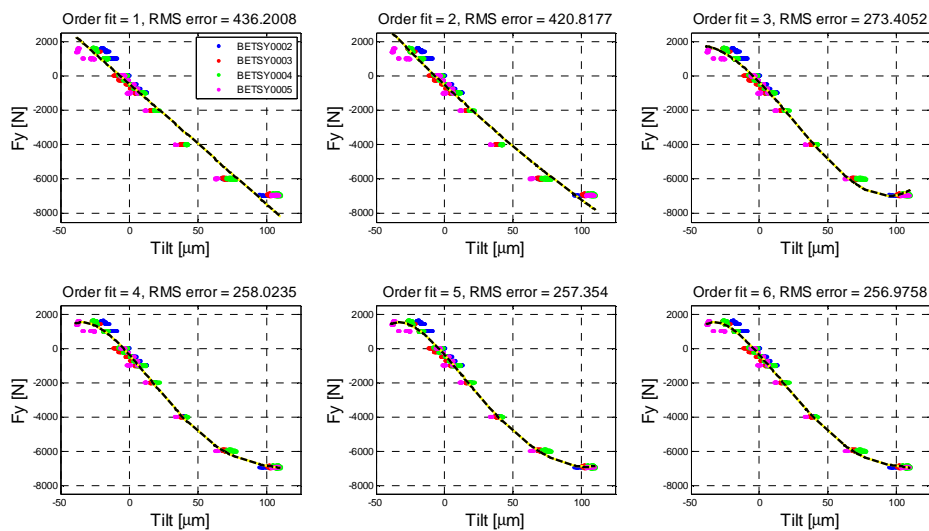


Figure 114 BETSY measurements: deflection top sensor versus lateral force approximated by n-th order polynomials for the BETSY test performed on the bearing which is mounted in the BMW E60

Bottom deflection versus lateral force approximated by nth order polynomials

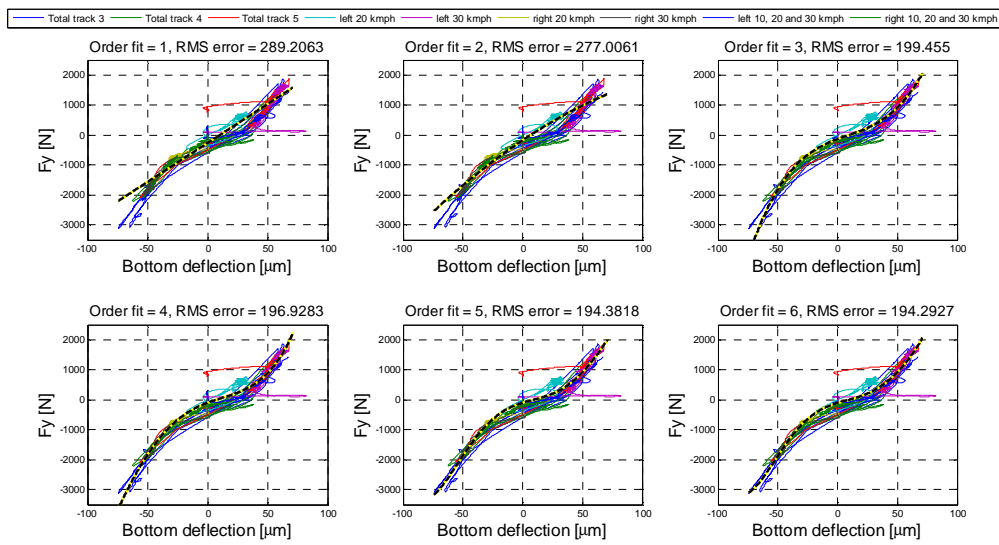


Figure 115 Field measurements: deflection bottom sensor versus lateral force approximated by n-th order polynomials

Top deflection versus lateral force approximated by nth order polynomials

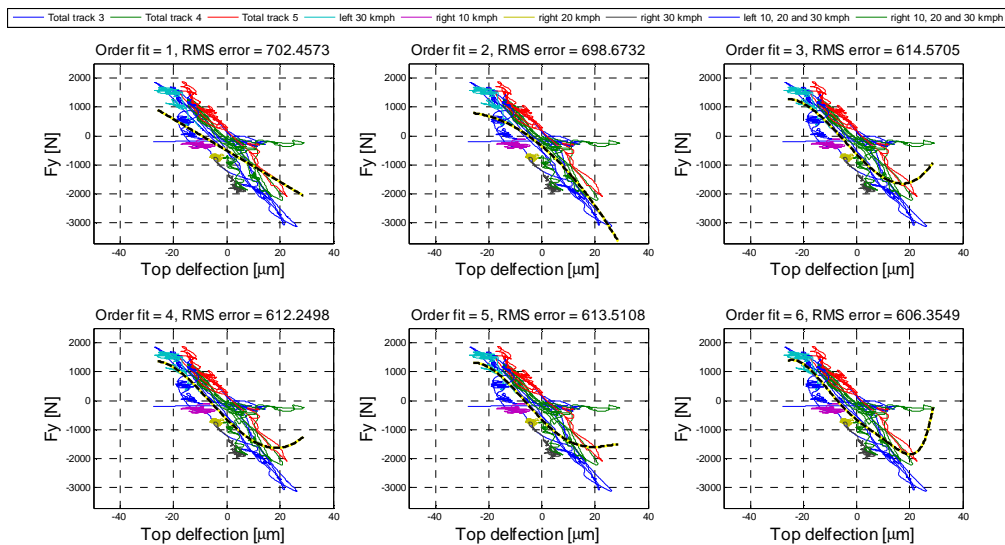


Figure 116 Field measurements: deflection top sensor versus lateral force approximated by n-th order polynomials

8.6 Appendix F

8.6.1 F_y estimations using Eddy-current sensor

Lateral force estimation based on the tilt measurement, 1 Hz - 10 Hz

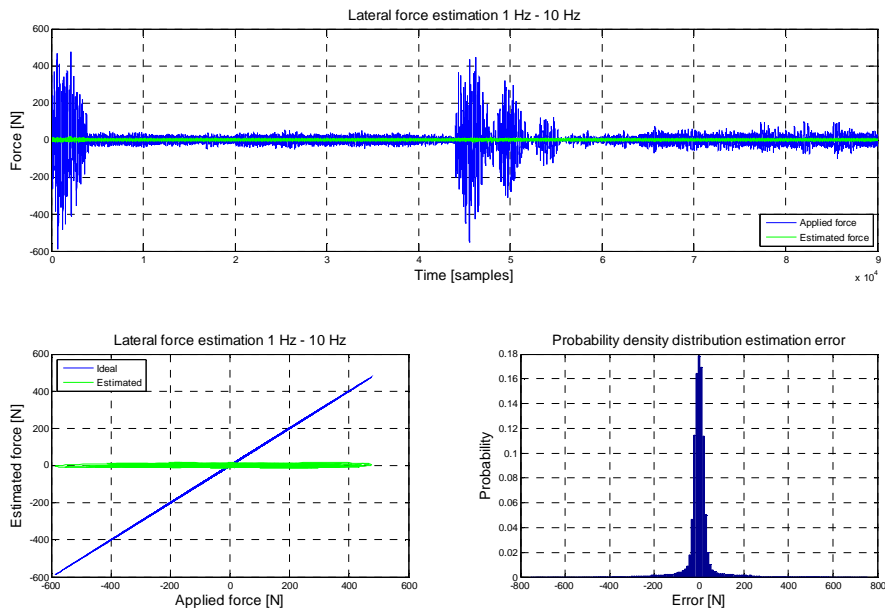


Figure 117 High frequent force estimation using the tilt

Lateral force estimation based on the tilt measurement, 0 Hz - 10 Hz

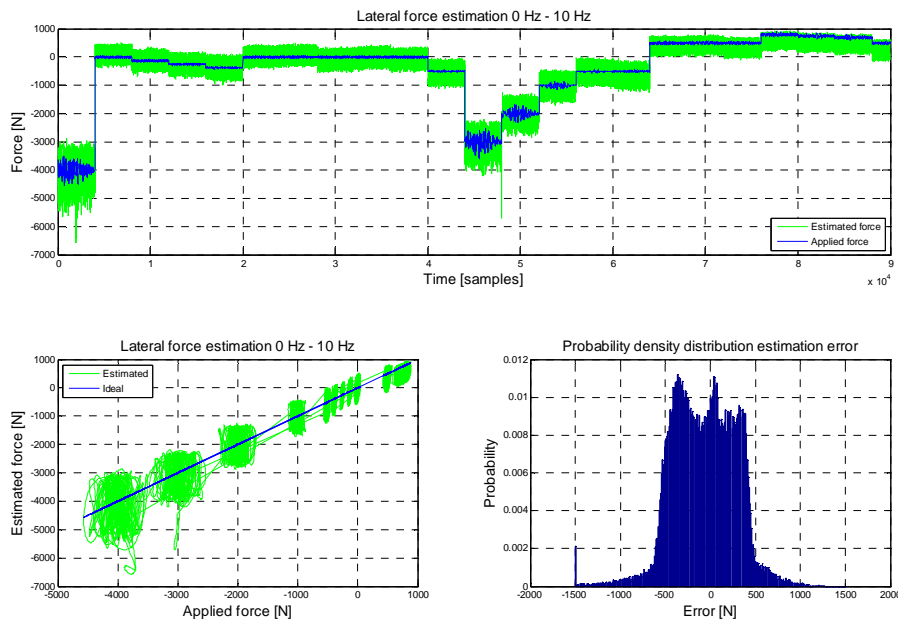


Figure 118 Full frequency range force estimation using the tilt

Lateral force estimation based on the top sensor measurement, 1 Hz - 10 Hz

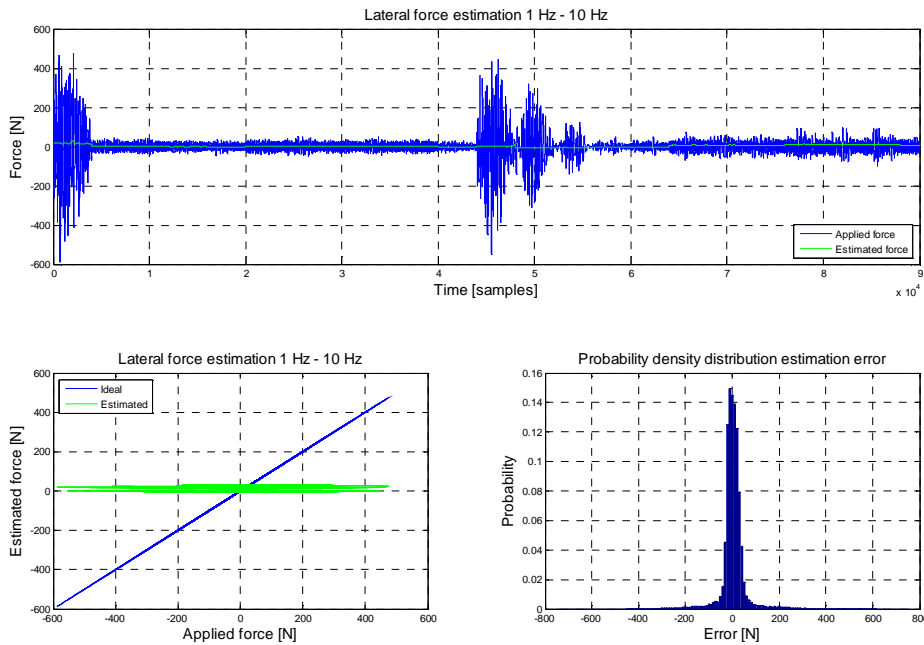


Figure 119 High frequent force estimation using the top sensor

Lateral force estimation based on the top sensor measurement, 0 Hz - 10 Hz

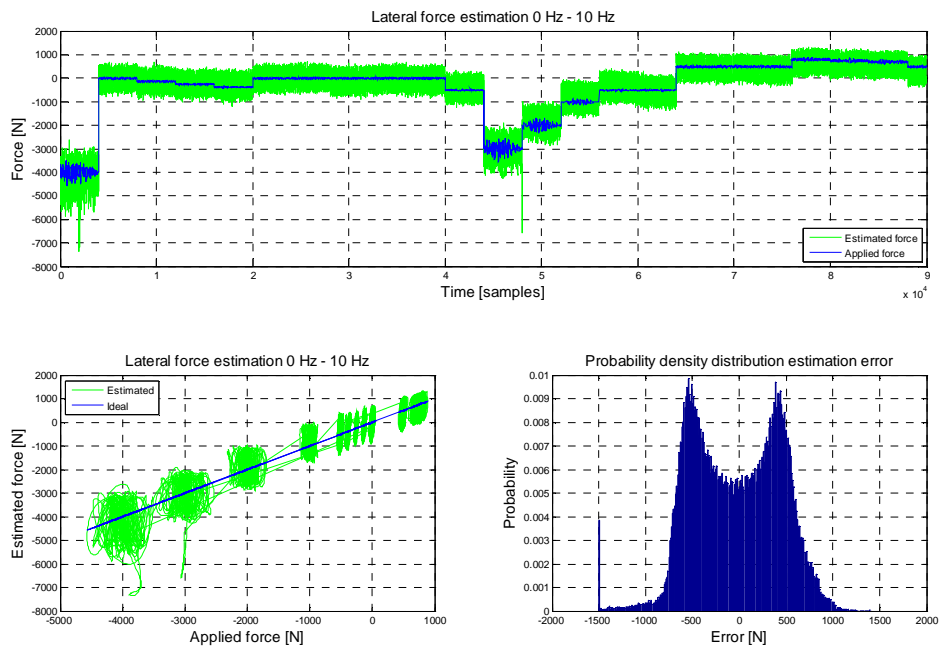


Figure 120 Full frequency range force estimation using the top sensor

Lateral force estimation based on the bottom sensor measurement, 1 Hz - 10 Hz

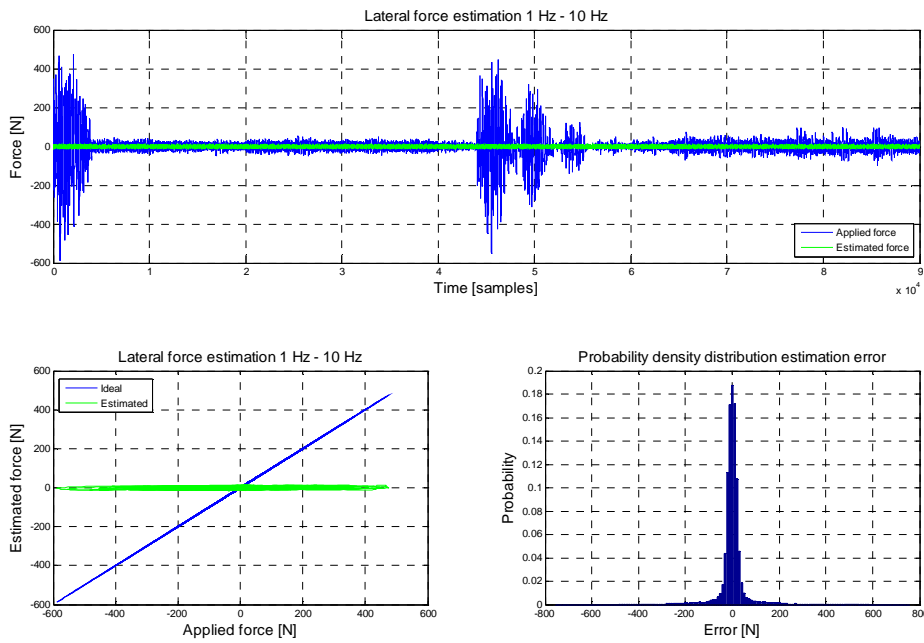


Figure 121 High frequent force estimation using the bottom sensor

Lateral force estimation based on the bottom sensor measurement, 0 Hz - 10 Hz

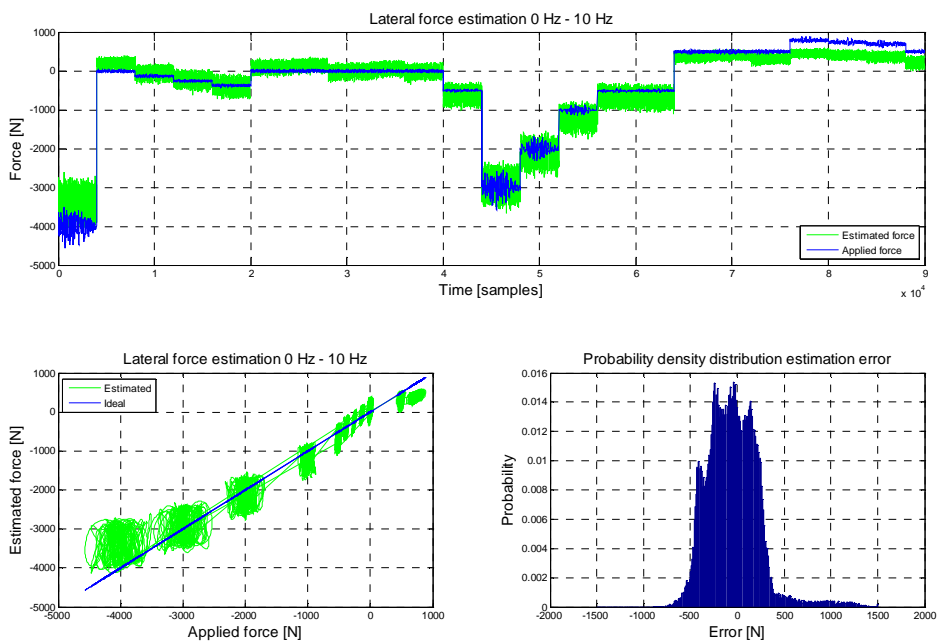


Figure 122 Full frequency range force estimation using the bottom sensor

8.7 Appendix G

8.7.1 Cabling of the sensor signals

The six strain gauge signals leave the conditioner box via a 25 pole D-sub plug. Table 45 shows what signal is represented by what pin of the plug. Because only 12 pins are used (six signal and six grounds), 13 pins are unused. A flat cable is connected to the plug and finds its way to the trunk.

Table 45 Strain gauge conditioner box left- and right side

Strain gauge conditioner box left- and right side	
D-Sub 25 pin	Signal
1	Channel 1 low
2	Channel 1 high
3	Channel 2 low
4	Channel 2 high
5	Channel 3 low
6	Channel 3 high
7	Channel 3 low
8	Channel 4 high
9	Channel 4 low
10	Channel 5 high
11	Channel 6 low
12	Channel 6 high
13-25	Empty

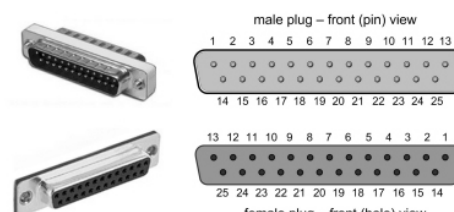


Figure 123 25 D-Sub plug

The Eddy-current sensor signals leave the conditioner box via a BNC cable. These cables are inserted to the flat cable. The end of the flat cable counts thus four extra terminals (two signals and two grounds). At the end of the flat cable a 25 Sub-D connector is connected. Table 46 shows what signal is represented by what pin of the plug.

Table 46 25 D-Sub connector at the trunk side

Trunk side		
D-Sub 25 pin	Signal	Note
1	Channel 1 low	
2	Channel 1 high	
3	Channel 2 low	
4	Channel 2 high	
5	Channel 3 low	
6	Channel 3 high	
7	Channel 3 low	
8	Channel 4 high	
9	Channel 4 low	
10	Channel 5 high	
11	Channel 6 low	
12	Channel 6 high	
13	Eddy-current top sensor low	Left side: 3208. Right side: 3210
14	Eddy-current top sensor high	Left side: 3208. Right side: 3210
15	Eddy-current bottom sensor low	Left side: 3209. Right side: 3211
16	Eddy-current bottom sensor high	Left side: 3209. Right side: 3211
17-25	Empty	

Also to the VELOS wheel a 25 D-Sub connector is connected, see Table 47.

Table 47 25 D-Sub connector VELOS

VELOS measuring wheel	
D-Sub 25 pin	Signal
1	VELOS MFy
2	VELOS MR13
3	VELOS MR24
4	VELOS MMy
5	VELOS MM13
6	VELOS MM24
7	VELOS MSIN
8	VELOS MCOS
9	MEPS/T1
10	MEPS/T2
25	Ground
11 - 24	Empty

Three D-Sub connectors with 25 pins end up in the trunk. One for the left- and right side load sensing equipment and one the VELOS wheel. The data acquisition unit, the dSpace Autobox, accepts a D-Sub 50 connector. The three D-Sub 25 connectors are connected via a flat cable to the D-Sub 50 connector for the Autobox. Table 48 shows what pin of this connector is represented by what signal. The second column of this table shows the name as it is known by the dSpace software.

Table 48 D-Sub 50 connector at the data acquisition unit

Autobox side		
D-Sub 50 connector pin	Signal ADC	Signal
1	Vin, 1	Bearing left: Channel 1 high
2	Vin, 3	Bearing left: Channel 2 high
3	Vin, 5	Bearing left: Channel 3 high
4	Vin, 7	Bearing left: Channel 4 high
5	Vin, 9	Bearing left: Channel 5 high
6	Vin, 11	Bearing left: Channel 6 high
7	Vin, 13	Bearing left: Eddy-current top sensor high (3208)
8	Vin, 15	Bearing left: Eddy-current bottom sensor high (3209)
9	Vin, 17	Bearing right: Channel 1 high
10	Vin, 19	Bearing right: Channel 2 high
11	Vin, 21	Bearing right: Channel 3 high
12	Vin, 23	Bearing right: Channel 4 high
13	Vin, 25	Bearing right: Channel 5 high
14	Vin, 27	Bearing right: Channel 6 high
15	Vin, 29	Bearing right: Eddy-current top sensor high (3210)
16	Vin, 31	Bearing right: Eddy-current bottom sensor high (3211)
17	GND	Ground VELOS measuring wheel
18	GND	Bearing left: Channel 1 low
19	GND	Bearing left: Channel 2 low
20	GND	Bearing left: Channel 3 low
21	GND	Bearing left: Channel 4 low
22	GND	Bearing left: Channel 5 low
23	GND	Bearing left: Channel 6 low
24	GND	Bearing left: Eddy-current top sensor low (3208)
25	GND	Bearing left: Eddy-current bottom sensor low (3209)
26	GND	Bearing right: Channel 1 low
27	GND	Bearing right: Channel 2 low
28	GND	Bearing right: Channel 3 low
29	GND	Bearing right: Channel 4 low
30	GND	Bearing right: Channel 5 low
31	GND	Bearing right: Channel 6 low
32	GND	Bearing right: Eddy-current top sensor low (3210)
33	GND	Bearing right: Eddy-current bottom sensor low (3211)
34	Vin, 2	VELOS MFy
35	Vin, 4	VELOS MR13
36	Vin, 6	VELOS MR24
37	Vin, 8	VELOS MMy
38	Vin, 10	VELOS MM13
39	Vin, 12	VELOS MM24
40	Vin, 14	VELOS MSIN
41	Vin, 16	VELOS MCOS
42	Vin, 18	VELOS MEPST1 - NOT USED
43	Vin, 20	VELOS MEPST2 - NOT USED
44-50		Empty

Table 49 Measured signals during the field tests at the test track of SKF Nieuwegein

Column	Signal
1	Left bearing strain gauge 1
2	Left bearing strain gauge 2
3	Left bearing strain gauge 3
4	Left bearing strain gauge 4
5	Left bearing strain gauge 5
6	Left bearing strain gauge 6
7	Left bearing Eddy-current top sensor
8	Left bearing Eddy-current bottom sensor
9	Right bearing strain gauge 1
10	Right bearing strain gauge 2
11	Right bearing strain gauge 3
12	Right bearing strain gauge 4
13	Right bearing strain gauge 5
14	Right bearing strain gauge 6
15	Right bearing Eddy-current top sensor
16	Right bearing Eddy-current bottom sensor
17	Velos: MFy
18	Velos: MR13
19	Velos: MR24
20	Velos: MMY
21	Velos: MM13
22	Velos: MM24
23	Velos: MSIN
24	Velos: MCOS

9 Bibliography

- Ballegooij, S. v. (2011). *Effect of housing compliance on load sensing bearing system and sensor responses*. Nieuwegein, NL: SKF.
- Bot, D. d. (2009). *A Temperature state estimator for a load sensing hub bearing unit*. Master of Science thesis: SKF, TU Delft.
- Douglas C. Montgomery, E. A. *Introduction to linear regression analysis*.
- Henk Mol, S. v. (2010). *Load Sensing G1 G2 Combination*. Nieuwegein: SKF.
- Jayashankar, A. (2011). *Experimental & modeling study of the influence of support stiffness on load sensing bearings*. Delft, Nieuwegein: TU Delft, SKF.
- Kistler, B. *VELOS instruction manual*.
- Mol, H. (2010). *Patent No. WO2011154016A1*. The Netherlands.
- Zaaijer, E. (2005). *NL05E905 Evaluation and validation of zero lshbu*. Nieuwegein: SKF.